The Dissertation Committee for Tushar Sharma Certifies that this is the approved version of the following dissertation:

Nanostructured PVDF-TrFE based Piezoelectric Pressure Sensors on Catheter for Cardiovascular Applications

Committee:

John X.J. Zhang, Supervisor

Brijesh S. Gill, Co-Supervisor

Christopher J. Ellison

Pengyu Ren

Thomas E. Milner

Nanostructured PVDF-TrFE based Piezoelectric Pressure Sensors on Catheter for Cardiovascular Applications

by

Tushar Sharma, B.Tech.; M.S.E.,

Dissertation

Presented to the Faculty of the Graduate School of

The University of Texas at Austin

in Partial Fulfillment

of the Requirements

for the Degree of

Doctor of Philosophy

The University of Texas at Austin

December 2012

Dedication

For Papa and Mumma

Acknowledgements

First and foremost I would like to thank my advisor, Prof. John X.J. Zhang for his guidance, advice and the wonderful training that helped me reach to this point in my career. Without his constant encouragement, expertise and great vision, none of this would have been possible. I cannot thank him enough for the influence he has had on me.

I would like to thank Dr. Billy Gill for initiating this project, financial support and the technical guidance. I would also like to thank my committee members, Dr. Christopher Ellison, Dr. Pengyu Ren and Dr. Thomas Milner for making this thesis a reality. Thank you!

Special thanks to my current and past collaborators, Dr. Mauro Ferrari, Dr. Rodney Ruoff, Dr. Marc Feldman, Dr. David Terreson and Dr. Tony Hu, who have helped broaden my horizons. Their contribution was highly important towards shaping my interest in inter-disciplinary research.

The students at the Zhang Research lab have an amazing sport and made my graduate school exciting beyond imagination. I would like to thank them for their valuable feedback, attending my practice talks and indulging in technical and non-technical discussions that kept me entertained and provoked my thinking. I would like to make a special mention of our research associate, Dr. Kaz Hoshino. He has been a great mentor and instrumental with his keen observation and insight on the various aspects of this research. I would also like to thank Dr. Dajing Chen, Yu-Yen Huang, Youngkyu Lee,

Youmin Wang, Lingyun Wang, Gauri Bhave, Peng Chen, Elaine Ng, Oanh Hoang, Nick Triesault, Karthik and Stephanie for an amazing time in the lab. Special thanks to Sahil Naik, Jewel Langevine, Ryan Truby, Yang Liu, Sarah Pederson, Christina Wood and Chet Murthy for their extremely valuable contributions towards this research project. I would also like to thank my co-workers in the past, Dr. Ashwini Gopal, Andrew Horton, Jean Fakhoury, Dr. Yuyan Wang, Dr. Karthik Kumar, Dr. Daghan, Zhiguo Wang, Ellen Blinka and Kathyrn Loeffler for their guidance and making my graduate school life, an enjoyable experience. I need to thank Bobby M. Knight for all the awesome work and outside-of-work related times we have had together. It was great working with you as a teaching assistant and hope to have more of our important meetings later on as well.

Outside the lab, I owe a big thank-you to an amazing bunch of people who have supported, mentored and encouraged me in numerous endeavors. I owe it to my best friends in Austin, especially Subhamoy Das, Varun Pattani, Abhimanyu Bhat and Andrea Lopez. You guys have helped me survive more than you know it. I also owe it big time to all the runners and members of Association for India's Development. I learnt to push myself to new limits because of all of you and y'all simply rock! It would be unfair to neglect the importance of some amazing friends, who sadly had to relocate from Austin due to various reasons, especially Animesh Agarawal, Mithun Prakash Vyas, Kanay Jerath and Tamanna Shaikh; also to Rohan Mahadik, Reshmy Mohanan and Anousha Lakhani. Lastly, I would like to thank all my undergrad and life-long childhood friends who kept in touch with me even after I came to the USofA, especially Amit Garg, Piyush Labhsetwar, Utsav Aggarwal, Vinay Jayakumar, K.B. Ganesh, Karan Govil, Rahul Sethi and Karan Dogra. We have always seen the good of times and hope to continue to do so.

Finally, there are two very important people in my life that made it all happen and come together. Thanks to my Papa, Mumma and Nani-mumma who have always been standing by my side through the various phases of my life. You have been my worst critics and best friends at the same time. I owe my every achievement to you and to your love for me.

Writing this acknowledgement has been a great revealing experience for me. I know for sure that, even though I tried very hard, I have missed a couple of names that deserve to be mentioned here. So if you were reading this section in anticipation of finding your name, I salute you with a big thank-you!

Nanostructured PVDF-TrFE based Piezoelectric Pressure Sensors on Catheter for Cardiovascular Applications

Tushar Sharma, Ph.D.

The University of Texas at Austin, 2012

Supervisor: John X.J. Zhang

Co-supervisor: Brijesh S. Gill

The objective of this research is to develop a new class of miniaturized sensors on-catheter technology through the integration of functional nanomaterials and flexible microsystems, with high sensitivity, fast recovery time, reduced form factor, for *in situ* blood pressure and flow monitoring with minimal invasiveness. Real-time endovascular pressure measurement techniques are crucial to evaluate the hemodynamics, which indicates the physiological state of the cardiovascular system. Current technology relies on fluid filled catheter coupled to remote transducers to measure endovascular pressures and gradients. The fluid filled catheters are bulky, inherently inaccurate due to the tubing mechanical resonance, and with low signal integrity due to the vibration noises from the environment. Silicon based conventional pressure sensors have complications due to issues of catheter stiffness, biocompatibility or small form factor integration. We propose a paradigm shift in designing the endovascular pressure sensing technology, through

developing compact flexible sensing structures using nanoengineered piezoelectric polymers which can be integrated on catheters without consuming the internal lumen space.

We focused on designing novel nanostructures using PVDF-TrFE (Polyvinyledene fluoride trifluoroethylene), with well controlled β-crystalline phase to significantly improve the resulting sensor performance. The research objectives include: (1) Thin-film structures for higher piezoelectric effect without any mechanical stretching or poling requirements, (2) High density highly-aligned electrospun nanofibers through electrospinning towards enhanced sensitivity; (3) Core-shell electrospun nanofiber for tapping the near β-crystalline phase formation and high cyrstallinity by virtue of inherent stress and stretching involved in the fabrication procedure. For pressure sensor design and characterization, we worked on two main form factors designs: thin-film, and aligned electrospun nanofiber based sensors patterned on catheter tips which are ready to be deployed in intra-vascular environment. Testing results showed promising results from PVDF based pressure sensors. The average sensitivity of the PVDF sensors was found to be four times higher than commercial pressure sensor while the PVDF sensor had five fold shorter response time than commercial pressure sensor, making the PVDF sensors highly suitable for real-time pressure measurements using catheters.

Table of Contents

List of Tables

List of Figures

Chapter 1: Background and Significance

1.1 MOTIVATION

Traditionally, surgery required an incision large enough for the surgeon to see directly and place his or her fingers and instruments directly into the target operating site. Most often, the damage done to skin, muscle, connective tissue, and bone to reach the region of interest causes much greater injury than the curative procedure itself. This results in more pain to the patient, longer recovery times, and complications due to surgical trauma. The accelerating trend is toward minimally invasive surgery (MIS) by using catheters. This technique has great potential to allow access to regions now inaccessible, or to enhance the surgeon's abilities in applications where current minimally invasive techniques do not permit the full range of human dexterity and perception. In addition, they can even extend the surgeon's capability over great distances, via telesurgery [1-3].

Catheter-based blood pressure sensors are desired for several reasons, first being safety of the catheter insertion. Current methods of tracking catheter insertion include angiography, requiring contrast agents, X-ray imaging and surgeon experience [4-6]. These methods can potentially cause the adverse effects of allergic reactions and radiation exposure, or vessel puncture, respectively. Both methods involve unnecessary risks and costs. These problems can be solved using a catheter-based blood pressure sensor. These sensors can be placed on catheter tips, and the transmitting lines routed through one of the lumens of the catheter.

Secondly, catheter-based blood pressure sensors can aid with the controlled catheter balloon inflation. The current technique relies on surgeon experience to determine the completeness of balloon inflation. With the catheter based blood pressure sensor, the placement of blood pressure sensors before and after the balloon can provide surgeons an indicator of balloon inflation.

Lastly, the catheter based blood pressure sensor can give important information about potential occlusions and perforations via the resulting changes in blood pressure.

Presently, over 1.5 million pulmonary artery catheters are placed per year for real-time hemodynamic monitoring in the U.S. [7] with sales drawing $17 billion in 2010 and $21.2 billion in 2011 [8]. Endovascular techniques for measurement of physiologic parameters that describe normal and abnormal hemodynamics have changed little since Richard Gorlin derived his equation for calculating cardiac valve areas in 1951 [9]. Current systems rely on fluid filled catheter coupled to remote transducers to measure endovascular pressure and gradients [10-12]. The process uses a flexible stainless steel guide wire about 1mm in diameter that is inserted into the artery. This guide wire is pushed to the desired location under fluoroscopic monitoring, used as a guide for insertion of a hollow catheter, and is then removed. Finally the catheter is filled with a suitable fluid whose pressure is a function of the propagation characteristics of the hollow catheter [13]. Figure 1.1 shows one such pulmonary artery catheter frequently used for blood pressure measurements. This technique has the advantage of minimal expense and decent accuracy since the external transducer can be calibrated against an external reference at any time.

Initial attempts at producing manometer- tipped catheters were successful in terms of their ability to generate a more artifact- free measurement, but have not been used in a widespread clinical fashion because of a lack of flexibility inherent to their construction that makes them less safe for intravascular use. Systems that incorporate fluid filled catheters coupled to remote transducers for pressure measurement have inherent inaccuracies related to resonance in the system, which is a function primarily of the length and diameter of the tubing and the frequency of the waveform being measured, which is typically the heart rate for intravascular systems. In addition to artifact created by resonance, which tends to overestimate pressure waveforms before the transducer by artifactual amplification, compressible volumes, like air in the tubing, can dampen waveforms leading to underestimation of pressures [14].

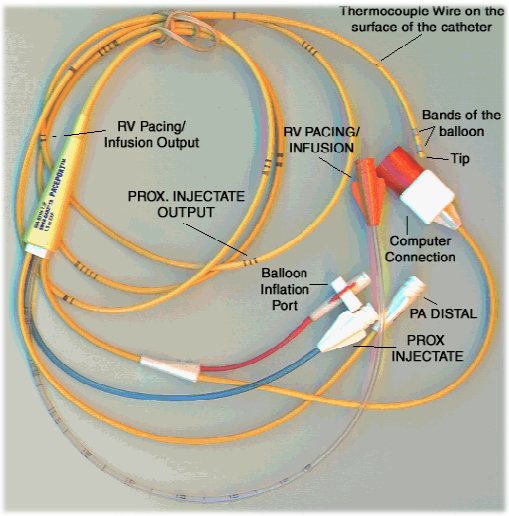

Figure 1.1 Photograph of swan-ganz catheter, a pulmonary artery catheter frequently used for intravascular pressure measurement. Source: [15]

Use of manometer-tipped catheters and external transducer is currently the 'gold standard', against which all other systems are judged [16]. However for delicate surgeries,

like ventriculostomy, has the disadvantage of tissue penetration (of the meninges and brain), with the possibility of transmission of bacteria through the fluid coupling [17].

Alternative techniques for measurement of the intravascular blood-pressures have also been reported with pressure sensitive diaphragms; MEMS based pressure sensors and fiberoptic tranducers [18, 19]. MEMS have received a great deal of attention in recent years. MEMS pressure sensors currently dominate the market for greater-than-atmospheric-pressure sensors. The 1995 for micromachined pressure sensors was approximately US $1 billion, and is expected to grow to US $2.5 billion by 2005 [20]. M. Esashi, *et al.* [21] reported miniaturized silicon diaphragm sensors using the piezoresistive operating principle for biomedical experiment purposes. During the fabricated chip transferring, they suffered from thermal stress, additional sensitivity calibration, and associated circuit complex. After a couple of decades later, there have been several alternative approaches, but transferring chips onto the catheter is not a scalable solution. Moreover, such sensors are bulky which makes them unsuitable for use in catheters, which must have internal space for interventional apparatus. Further, the stiffness imparted to the catheter by such sensors is highly undesirable.

In addition to the numerous applications mentioned earlier, the development of a flexible pressure sensor can enable the development of novel catheters that can ease some of the complicated surgeries. Here we consider one such surgery, of pelvic fractures, and the role of such a catheter:

Pelvic fractures (PF) are a very common clinical finding in fatally wounded US combat personnel. In trauma care surgeries, pelvic ring injuries are the third most

common cause of death (behind central nervous system injury and major pulmonary/cardiac injury). Associated organ system injury is also common in this setting (though less so than in combat injuries). Importantly, the median time to death is roughly 6 hours in fatally injured patients with pelvic fracture versus 40 hours in those without PF, strongly suggesting that exsanguination is a major contributor to mortality in patients with PF.

Surgical control of pelvic hemorrhage has proven difficult [22]. Direct access to the internal iliac artery and its branches is problematic from an anatomic standpoint and requires disruption of the peritoneum with resultant loss of tamponade of bleeding from deep structures.

The mainstay of hemorrhage control in PF is angiographic embolization of the internal iliac artery or its branches [22-26]. This is the only method available which can control selective branches of both the anterior and posterior arterial elements of the pelvis. This methodology requires fluoroscopy capability with a large set of proprietary gear to be fully effective, along with highly specialized training. The endovascular balloon occlusion technique yields several potential advantages for the control of pelvic hemorrhage.

There is one significant problem with occluding the distal aorta: there is occlusion of blood flow to the legs. This vastly increases the volume of ischemic tissue and resultant reperfusion injury to the other organs when the balloon is removed. Additionally, if one or both legs are relatively uninjured, the technique incurs risk of ischemic neuropathy and subsequent loss of function even after rehabilitation.

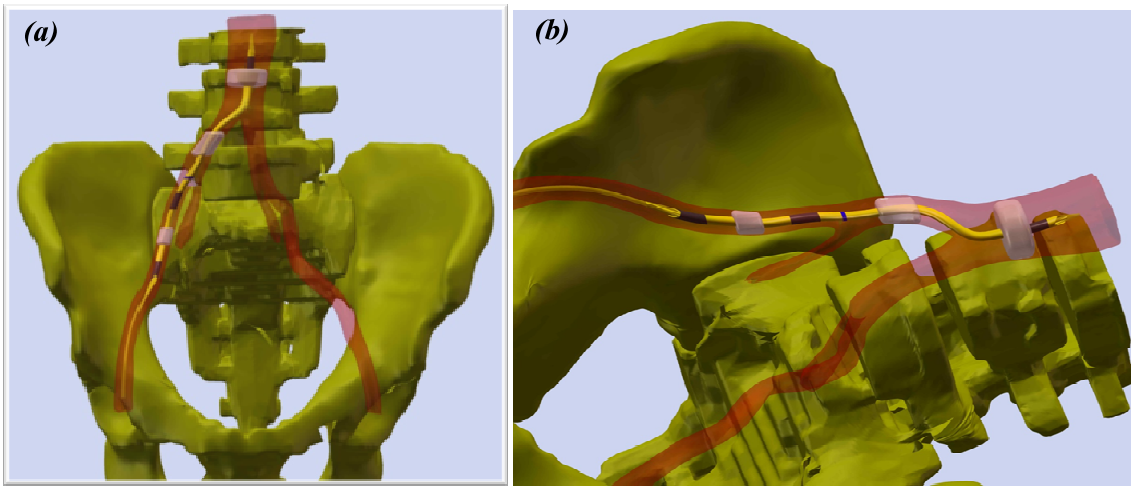

Figure 1.2 (a) Schematic showing placement of a three- balloon catheter in Illiac artery with multiple pressure sensors (in black) on either side of the balloons and (b) Catheter deployed to occlude IIA. In normal use the aortic balloon is inflated as an aid to confirm placement but then deflated once the IIA is isolated. If aortic occlusion is indicated (e.g., massive lower limb trauma with uncompressible pelvic injury) the aortic balloon can be left inflated to occlude flow to the contralateral pelvis and leg.

A more robust solution would isolate the internal iliac artery while maintaining flow of blood to the leg. A catheter designed along these lines would also be of major benefit. As far as we are aware, no hospital in the United States maintains 24-hour, in house angiography capability. The ability to temporize exsanguinating pelvic bleeding for several hours in a manner consistent with damage control principles would be of substantial benefit in these highly resource-intensive patients.

In ideal case, the desired catheter will have three balloons: an aortic balloon, a common iliac balloon, and an external iliac balloon. While at first glance placement of the IIA catheter would seem to be highly complex, the actual placement of this catheter will actually be simpler and more robust overall than placement of the existing aortic

occluder catheter. In addition to the balloons, the catheter needs to rely on sensors for the successful functioning of the catheter. A pressure sensor located before and between each balloon, can allow determination of pressures between inflated balloons. If the balloon in between is not inflated, any pair of pressure sensors can be used to determine flow direction of blood between the sensors. Therefore such sensors could allow for determination of the blood pressures along with the possible indication of any accidental dislogding of balloons.

Intravascular measurement of pressure using a catheter design which minimizes catheter diameters and provides reproducible measurements over a large range of physiologic heart rates, while avoiding the artifact inherent in fluid filled systems, would improve significantly the quality of data and therefore improve clinical decision making. In the present study, we use flexible, biocompatible piezoelectric polymer for fabrication of compact yet highly sensitive pressure sensors that could be easily mounted on the curved surfaces of a catheter. In particular, we focus on fabrication of novel nano structures out of PVDF-TrFE (polyvinylidene fluoride trifluoroethylene) that can be used to fabricate sensitive pressure sensors for biomedical applications. We describe three main shapes and designs: (1) thin-film planar, (2) aligned electrospun nanofiber, and (3) core-shell electrospun nanofiber based sensors. Of the above listed designs for transducers, the thin-film planar and aligned electrospun nanofiber based designs would act as enabling designs for the required characterization and development of core-shell electrospun nanofiber based sensors. Whereas, core-shell electrospun nanofiber based sensors will tap the near beta formation and high cyrstallinity by virtue of inherent stress and stretching involved in the fabrication procedure. Further, the transducer design is novel and one that has not been reported elsewhere. Enhancing the crystallinity in the

structures can result in highly sensitive pressure sensors for biomedical applications. Incorporation of nanofiber technology provides the opportunity to develop multifunctional "smart" catheters while maintaining lumen space which is important for aiding catheter placement and providing access for drug, contrast and indicator administration.

1.2 DISSERTATION ROADMAP

The motivations for the dissertation and the choice of approach are introduced in Chapter 1. An overview of various pressure sensing technologies, suitable for catheter application, are discussed in Chapter 2. Chapter 3 talks about the PVDF as a material along with its co-polymers. We focus on the properties of the used PVDF-TrFE co-polymer used in the present study. Various techniques used to characterize the polymer are also covered in the same chapter. Chapter 4 presents results on the fabrication of different form factors of PVDF along with the characterization of those structures. In Chapter 4 we also describe the fabrication of highly aligned nanofibers and core-shell structures. Chapter 5 describes the device fabrication process and simulations comparing the advantages of using core-shell fibers versus the aligned nanofibers. Chapter 6 describes the results obtained from testing of the fabricated devices. Finally, Chapter 7 summarizes the dissertation and presents future research directions.

Chapter 2: Review of Pressure Sensing Technologies

2.1 Review of Silicon based technologies

Implantable pressure sensors have been a topic of interest since the 1950s [16, 27]. The history of the catheter-based blood pressure sensors dates back to 1969, when Melvin M. Scheinman, M.D., Joseph A. Abbot, M.D., and Elliot Rapaport first measured blood pressure in the pulmonary artery using a sensor incorporated with a nylon catheter. The next year, H.J.C. Jeremy Swan, Ph.D., and William Ganz, M.D., introduced a flow directed, balloon-tipped catheter [28]. Quickly becoming the standard for coronary care, their catheter was popular for its ease of use and ability to be used without fluoroscopy. These catheters, now known as Swan-Ganz or pulmonary artery catheters, utilize an inflated balloon wedged in a small pulmonary vessel to provide an indirect measurement of left atrium pressure. Subsequent techniques and alterations to the device have been created over the years for a variety of functions: the thermodilution technique for cardiac output measurement, addition of multiple lumens to allow injection of drugs through the catheter, incorporation of fiber optic SvO2 probes to obtain instantaneous measurements of oxygen saturation in the vessel, etc [29].

Similarly, new procedures and devices are being constantly created for real-time *in vivo* blood pressure measurements. Primarily motivated by ICU surgery and trauma care, new applications for intravascular blood pressure measurements include delivering real-time, direct measurement of pressure; offering information about potential occlusions and perforations; providing controlled catheter balloon inflation; and guiding the catheter through the vascular network are being constantly researched up.

Pressure sensors can vary drastically in technology, design, performance, application suitability and cost. A conservative estimate would be that there may be over 50 technologies and at least 300 companies making pressure sensors worldwide [30]. With the proliferation of catheters with multiple lumens, there are three main technologies that have emerged on the market for use as blood-pressure sensors: piezoresistive, inductive-capacitive, and optical

Since the discovery of piezoresistivity in silicon in the mid 1950s, silicon-based pressure sensors have been widely produced. Microfabrication technology has greatly succeeded from the techniques and advancements in integrated circuit industry, borrowing materials, processes, and toolsets. Because of this, MEMS based devices have seen huge explosion and are now poised to to catalyze the development of new markets. The 1995 market for MEMS based pressure sensors was approximately US $1 billion, and was expected to grow to US $2.5 billion by 2005 [20].

The common feature of all of the pressures sensors is that they covert pressure to motion of a mechanical element (Figure 2.1). Many devices are based on diaphragm movement. Other devices sought to improve the amount of deflection of a simple diaphragm such as the capsule. Strain gauges were commonly used on diaphragm based devices. For most part of the measurable range, amount of deflection is directly proportional to the applied pressure. In the case of a diaphragm with large built-in stress or large deflections, however, this direct proportionality does not hold true. A linear response in the deflection measurement is often desirable, since such systems are simple to calibrate and measure.

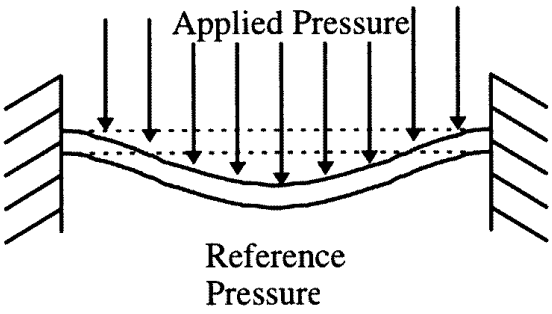

Figure 2.1 A schematic cross section of a typical pressure sensor diaphragm. Dotted lines represent the undeflected diaphragm. Source: [20]

2.1.2 Capacitive

Capacitive sensors employ parallel metalized plates as capacitors and measure the change in the capacitance. A typical bulk-micromachined capacitive pressure sensor is shown in Figure 2.2. The capacitance of a parallel plate can be found from

$$C = \frac{\varepsilon A}{d}$$

Where, ε, A, and d are the permittivity of the gap, the area of the plates, and the separation of the plates, respectively.

Since the deflection of a circular diaphragm is not linear, a capacitive sensor can be operated in contact mode to increase linearity. In contact mode, the capacitance is nearly proportional to the contact area, and therefore exhibits good linearity with respect to applied pressure [20].

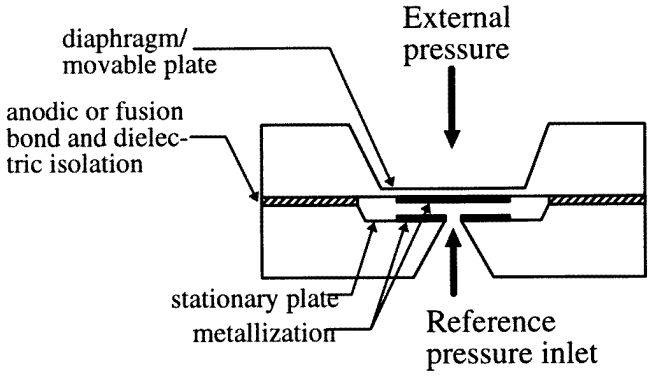

Figure 2.2 A cross-section schematic of a capacitive pressure sensor. Source: [20]

Alternative known method to achieve a linear response is to use bossed diaphragms. The thicker centre portion (or boss) is much stiffer than the thinner portion of the membrane on the outside. The centre boss contributes most of the capacitance of the structure and its shape does not distort appreciably under applied load. Hence the capacitance-pressure characteristics are more linear [20].

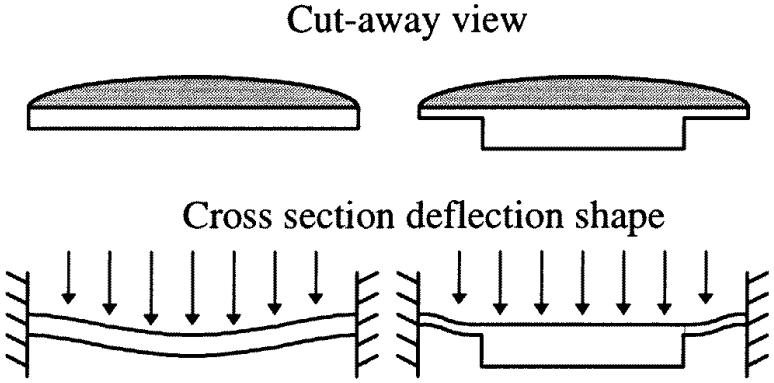

Figure 2.3 A comparison of deflection shapes for uniform-thickness (left) and bossed (right) diaphragms. Source: [20]

The main advantages of using capacitive based sensors over piezoresistive pressure sensors include higher pressure sensitivity and decreased temperature sensitivity [13, 14]. However, capacitive pressure sensors suffer from excessive signal loss due to parasitic capacitance, which hindered the development of miniaturized capacitive sensors until on-chip circuitry could be fabricated [16, 31].

Historically, capacitive sensors have benefited from the same advantages in diaphragm etching and wafer bonding that piezoresistive sensors have. However, the piezoresistive approach generally has a complex transducer with simple circuit requirements, while the opposite is true of the capacitive approach [20].

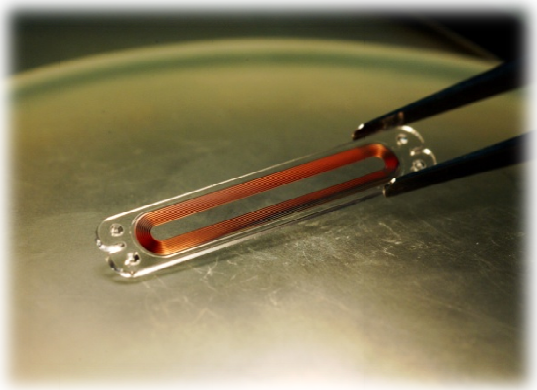

Figure 2.4 Photograph showing an inductive-capacitive based pressure sensor manufactured by CardioMEMS. Ref: [32]

A commercial sensor based on inductive-capacitive technology is produced by CardioMEMS, Inc. In contrast to other sensors, this sensor was not incorporated into the catheter. Rather, it uses a catheter to guide the permanent placement of the devices inside the vasculature to enable continuous real-time monitoring. While the sensor does not require an outside power source, it is relatively big (3.5 x 2 x 15 mm^3) and is inserted

using an equally big 11 French catheter. This sensor is used for low-pressure applications and requires a complex readout circuitry [33] [ref]. Manufactured using micoelectromechanical systems (MEMS) techniques, this sensor react to outer pressure forces by changing its capacitance. The resulting current is shared with the inductor, and the energy oscillates at a specific frequency. These specific frequencies can be measured and correlated to blood pressures [34].

2.1.3 Piezoresistive

In 1954, Smith reported the piezoresistive effect of silicon and germanium, stating that the material undergoes a change of resistance with applied stress. This discovery enabled production of semiconductor-based sensors [20]. Piezoresistive based pressure sensors have piezoresistors mounted on or in a diaphragm (Figure 2.5). For thin diaphragms and small deflections, the resistance change is linear with the pressure.

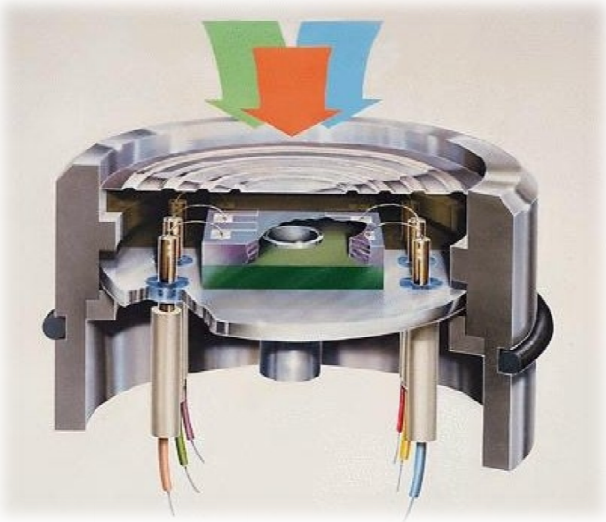

Figure 2.5 Cross-section schematic of a miniaturized MEMS piezoresistive pressure sensor. Source: [35]

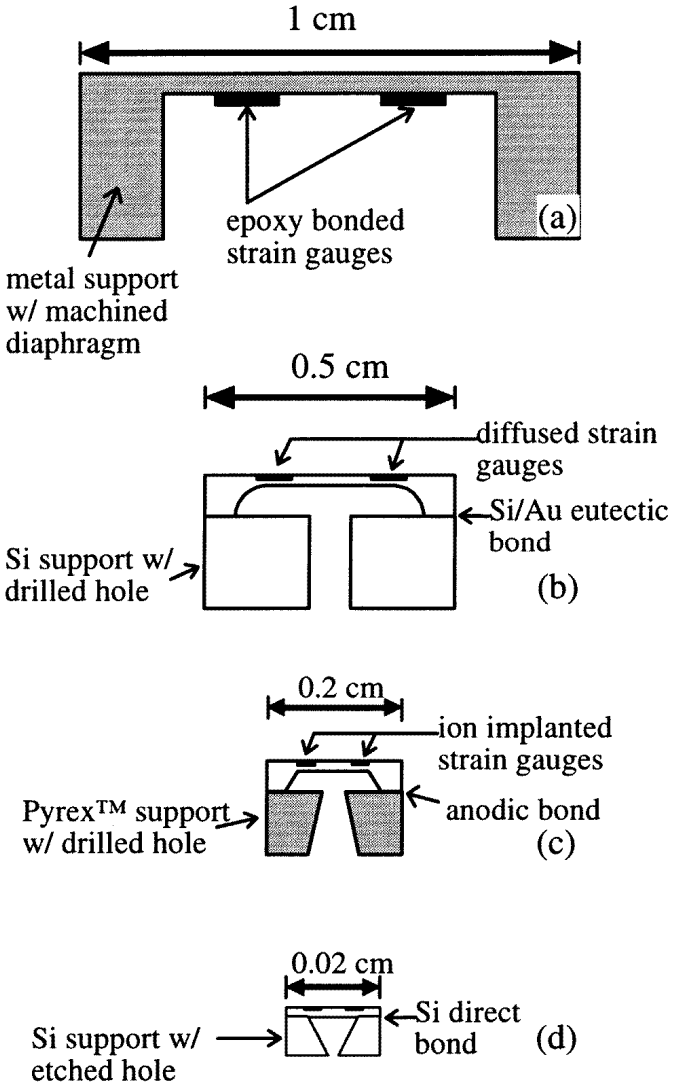

Figure 2.6 The evolution of diaphragm pressure sensors, adapted from [20].

The evolution of the piezoresistive pressure sensor technology is illustrated in Figure 2.6. Metal diaphragms were used initially to fabricate strain gauges. Metal diaphragms were quickly replaced with single-crystal diaphragms with diffused piezoresistors (Figure 2.6b), thereby eliminating the problems of hysteresis and creep

associated with metal diaphragms. At room temperatures, silicon is perfectly elastic and will not plastically deform [20]. Silicon obeys Hooke's law up to 1% strain, a tenfold increase over common metal alloys [36]. This made silicon based diaphragms an immediate popular choice over metal diaphragms.

Some of the first silicon diaphragms were created by mechanical milling spark machining followed by wet chemical isotropic etching, to create a cup shape [37]. These diaphragms were bonded to silicon supports by a gold-silicon eutectic (T = 370C) [37].

Development of anodic bonding and the ability of device to withstand 500-1500V and 400-600C enabled fabrication of silicon diaphragms bonded to pyrex glass supports (Figure 2.6c) [38, 39]. Use of anodic bonding amounted to significant cost reduction in the sensor fabrication process. However, this did not bring about the required miniaturization of the piezoresistive based sensors for biomedical applications.

Figure 2.7 Implantable bladder pressure sensor embedded in PDMS. Source: [40]

Introduction of silicon on insulator (SOI) technology in the 1980s offered a number of benefits to MEMS based pressure sensors, primarily because of the buried insulator that can act as an etch stop allowing precise control of the diaphragm thickness [41]. Since then, several miniaturized pressure sensors have been reported, which have silicon nitride [42-44] or polysilicon [45-47] diaphragms.

The leading piezoresistive sensor is produced by Millar Instruments. This sensor operates by utilizing a piezoresistive material placed on a silicon substrate. When the material is bent as a result of a mechanical force, the crystal lattice changes and causes a change in resistivity of the element. The change in resistance causes a change in voltage which can then be detected by the sensor. The sensor is a reusable device that can be incorporated onto a medium-sized 3.5 French catheter and can sense pressures from -50mmHg to +300mmHg. While the Millar instruments sensor is mechanically stable, it is disadvantaged by its large power consumption, temperature dependence, instability in dynamic field conditions, and high stiffness. This sensor has not yet been approved for human-use but is currently being used in animal and clinical studies [48].

Figure 2.8 Photograph showing various piezoresistive based pressure sensors manufactured by Millar Instruments. Source: [49]

2.1.4 Optics based

Sseveral diaphragms-based optical sensors have been reported based on the Mach-Zehnder interferometry [50-52] and Fabry-Perot interferometry [53] principle, which measures pressure induced deflections. The deflection derived from these devices varies linearly with pressure.

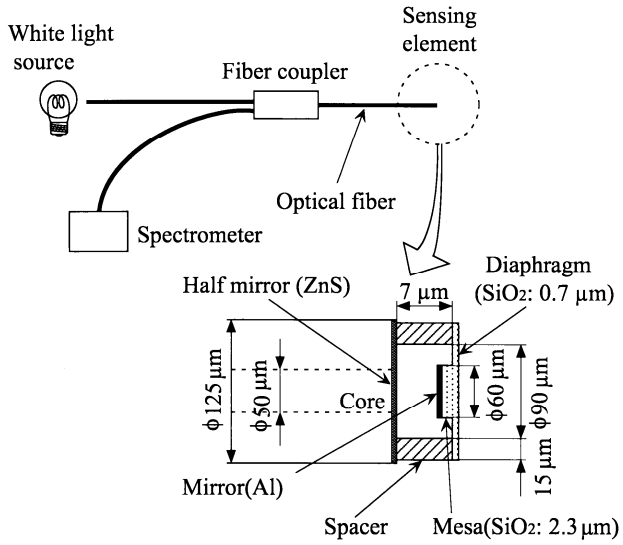

Figure 2.9 Schematic of a diaphragm-type 125µm diameter fiber-optic pressure sensor. Source: [54]

Optical sensors can be quite accurate, but often suffer from temperature sensitivity problems [20]. Moreover, aligning the optics and calibrating the sensors can be challenging and expensive. Furthermore, bending of the fiber can result in undesirable light intensity change, which results in output noise. A readout method using white-light interferometry was developed that succeeded in improving sensor performance [54, 55] to a certain extent.

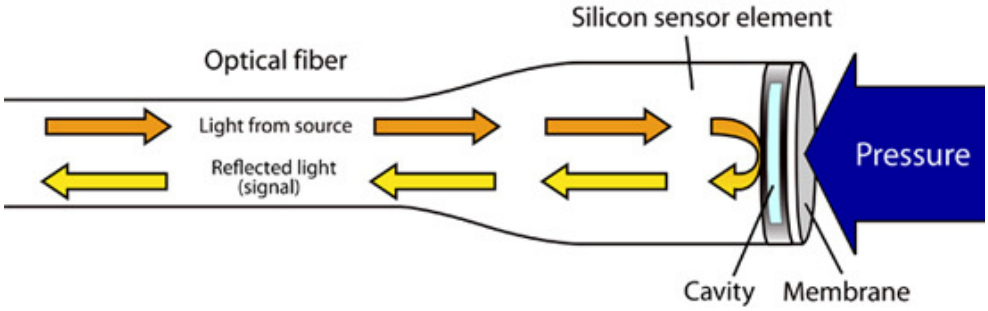

Figure 2.10 Schematic of a fiber-optic pressure sensor. Source: [56]

The company Samba Sensors produces a pressure sensor using fiber otpics. This sensor utilizes a reflective element at the end of the sensor tip which is compressed when a pressure wave passes over. The amount of compression translates to a change in the time required to reflect light back to the light source, which is correlated to a change in pressure. This technology makes for very accurate sensors that are also very small. The sensor, however, is disadvantaged by its fragility and change in path lengths due to bending of the fiber, when used for *in-vivo* applications.

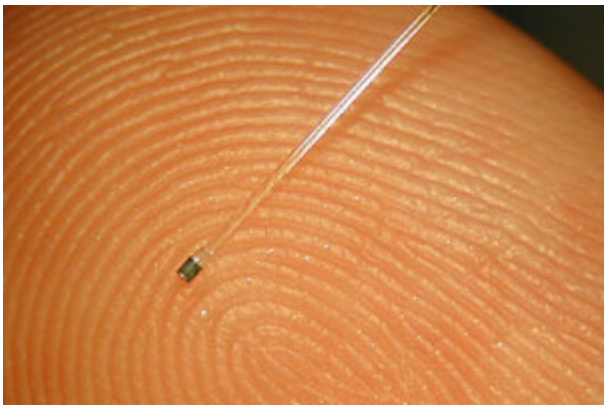

Figure 2.11 Photograph showing fiber-optic pressure sensor. Source: [56]

2.1.5 Disadvantages

With the advent of micro-electro-mechanical systems (MEMS) technology, both types of sensors (piezoresistive and capacitive) can be fabricated in a miniaturized fashion. Further, advancements in SOI based piezoresistive pressure sensors did decrease the required die size and simplified integration with electronics, but at the cost of reduced sensitivity and reproducibility of mechanical properties. Presently, piezo-resistive sensors are more commonly used in catheter based pressure sensing systems since they are better suited for periodic pressure sensing systems. They may be better suited for periodic

pressure measurement rather than for dynamic telemetric applications as the power consumption is high. Piezoresistive sensor often produces a large temperature error [20]. Capacitive sensors are more suited to implantable devices because of their sensitivity. Most importantly the reduced power consumption is essential for wire-less applications as power is not randomly available. For this reason research in the area of implantable pressure sensors tends to focus on the use of capacitive MEMS devices [57]. Drawbacks of a capacitive sensor for implantable applications include the need for active implanted electronics and its instability over various environmental conditions.

2.2 PIEZOELECTRIC SENSORS

Piezoelectricity is the phenomenon of generation of charge from a material under stress. This effect is also reversible. In other words, when a charge is introduced to a piezoelectric material, it undergoes deformation. Use of piezoelectric transducers has the ability to make improvements in a number of areas. First, existing sensors are bulky and most of their components must be mounted to the distal end of a catheter as they are too large to fit within a catheter lumen. These sensors also contain transducing fluids or multiple wires that fill the majority of the lumen volume. The thin film design of a piezo electric based sensor allows the entire sensor to be directly mounted onto the catheter; only a wire connected to the sensor's electrodes will need to be stored in the catheter, opening up the intraluminal space otherwise occupied by competitors' products.

There are numerous piezoelectric materials, including Barium titanate, lead zirconate titanate, lead titanate, zinc oxide among synthetic ceramics and sucrose, quartz, topaz, Rochelle salt, tendon amongst naturally occurring piezoelectric crystals. Application of these materials for the fabrication of thickness monitors, UV and IR

sensors, ultrasound transducers and energy harvesters is highly common [58]. However, ceramics and natural crystal based piezoelectric materials are not frequently used for fabrication of pressure sensors.

Further, the piezoceramics are not biocompatible. ZnO wires are inflexible and brittle with a large modulus of 21 GPa and fracture strain of only several percent [59]. The low fracture strain of ZnO wires means that breakage can occur when small deformations are applied. Even if many wires are incorporated into the device to increase charge, fracture of a few would lead to catastrophic failure of many other wires since the same mechanical load would be distributed amongst fewer wires. Further, ZnO is difficult to pattern, assemble into devices, stack in multiple layers and soluble in even dilute (< 1%) saline solutions [60, 61] making encapsulation challenging, especially given that the lead sheath is not a perfect barrier to penetration of body fluids over the life of the implant [62, 63].

2.2.1 Piezoelectric polymers

Polymers can be of two types: a) polar polymers such as PVDF (polyvinylendene fluoride), and b) nonpolar polymers such as polyethylene and polytetrafluoroethylene (Teflon). When a polymer material is introduced to a high electric field, the dipoles of the polymer will be re-oriented. There will be no dipole alignment in a non-polar polymer, however. Therefore, in a non-polar polymer, the net dipole on the bulk polymer is due to induced dipoles. Whereas in a polar polymer, the net dipole is from individual contributions of atomic, dipolar, and space charge polarizations [64].

Piezoelectric polymers such as PVDF (polyvinylendene fluoride) have several significant advantages over ZnO or any other ceramic. Firstly, piezoelectric polymers couple the high charge output of a piezoelectric material and flexibility of a polymeric material, besides being very good insulating materials.

Second, they can be processed into thick and thin films or any other desired size and shape. Third, they posses superior thermomechanical and chemical resistance properties [64].

Further, it is well known that the existing capacitive and piezoresistive pressure sensors are relatively unstable in dynamic flow conditions and can only be used in low pressure applications due to low flexibility and high rigidity. Because flexible piezoelectric polymers can withstand the mechanical forces created in high pressure applications, piezoelectric polymer are the ideal choice for sensor fabrication.

2.3 PVDF BASED SENSORS

PVDF exhibits the highest piezoelectricity among all piezoelectric polymers. Along with the high electromechanical coupling coefficient and its semi-crystalline nature, makes PVDF a popular choice for fabrication of robust and sensitive sensors. PVDF is an ideal biomaterial because it is nontoxic, inert, resistant to water absorption (absorbs < 0.04% by weight), biocompatible [65] and clean-room friendly.

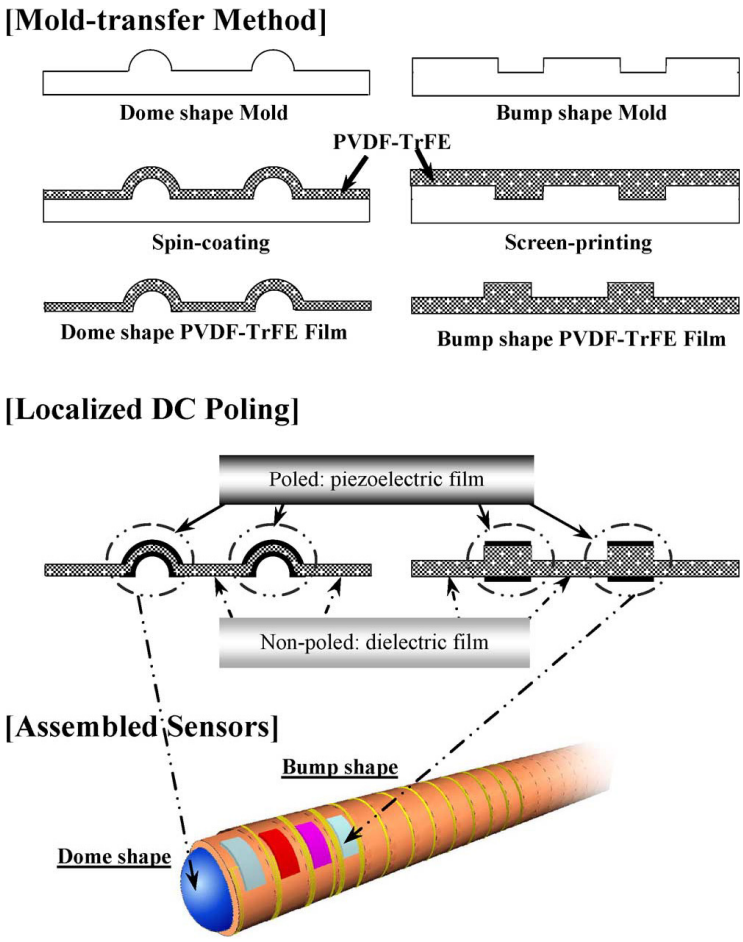

Figure 2.12 Dome and bump shaped PVDF-TrFE based piezoelectric tactile sensor modules for smart catheters. Source: [66]

The principle of fabricating PVDF based sensors remains the same. A diaphragm made using PVDF is usually used as the sensing element. Compression or stress in the membrane produces charge, which is recorded using the metalized electrodes coated on either side of the diaphragm. M. Robert *et al.* [67] reported a process that spin coat the copolymer film directly onto a curved substrate in order to make uniform surface using press focusing and lapping over a curved surface. However, this approach also required multi-processing steps and its result was not satisfactory. In contrast, C. Li *et al.* [68] and

Chunyan *et al.* [66] reported the film to be spin coated on a flat substrate and transferred onto the rounded catheter backing (Figure 2.12). However, this extra step required the use of an adhesive layer and a proper fit to the final substrate. Such transferring the film from its original substrate to the curved backing of the sensors can result in damage to the fragile piezoelectric film. Another problem is that the adhesion layer can become a source of another interface, which may be a major concern at high frequencies where the thickness of the glue layer may approach the dimension of a wavelength of the acoustic signal.

While use of PVDF as membrane for ultrasound transducers has been well known, application of PVDF for pressure sensing application is a recent trend. In another study, C. Li *et. al.* [69] reported the dual-mode operation of polyvinylidene fluoride trifluoroethylene (PVDF-TrFE) piezoelectric polymer diaphragm, capacitive, or resonant mode, as flexible intracranial pressure sensors (Figure 2.13). The dual-mode capability of the sensor had advantages of (a) high linearity in small pressure ranges of 0–50 mmHg and insensitivity to environmental temperature variations in the capacitive mode; and (b) high sensitivity and resonant frequency as the output in the resonant mode which allows easy adaption for wireless application. In addition, this approach provided two detection methodologies on a single device, thus allowing the independent measurement of pressure signals, thus generating two sets of data for comparison and error checking. However the sensor was bulk (in thickness) and use of air-cavity can prove to be lethal when employed for *in-vivo* applications.

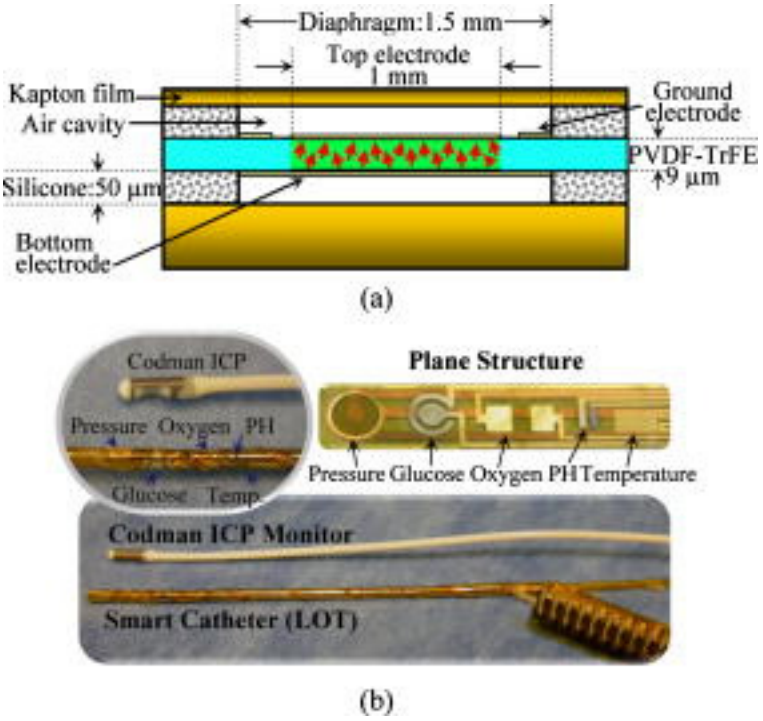

Figure 2.13 (a) Schematics of the intracranial pressure sensor and (b) photograph of the developed intracranial pressure sensor on smart multimodal catheter. Source: [69]

2.4 PRESENT APPROACH

We have developed versatile microsensors with built-in nanostructures as the core sensing elements that can profoundly revolutionize the catheter development, especially for combining multiple monitoring and diagnostic modalities on a smaller catheter. Untreated PVDF itself cannot have β phase without delicate mechanical stretching or electrical poling processes (Chapter 3). Additionally, due to its incompatibility with the standard lithography process, many alternative fabrication methods such as screen printing and shadow mask process [70] have been developed.

Our approach offers a practical option to overcome these limitations, and offers cost-effective batch process with high film uniformity and high resolution of polymer patterning towards enhanced sensor performance using standard clean room and electrospinning techniques.

In the present study, we focus on fabrication of novel nano structures out of PVDF-TrFE that can be used to fabricate sensitive pressure sensors for biomedical applications. In particular, we will work on three main shapes and designs: *(1) thin-film format, (2) highly aligned electrospun nanofiber, and (3) aligned core-shell electrospun nanofiber based sensors.*

PVDF has been conventionally drawn in to films either by melt casting or solvent casting. These techniques usually produce thicker films of PVDF (>15μm). Thin films of PVDF can be easily spin-coated from the solution obtained by dissolving the raw polymer in an organic polar solvent. In the present report, we study the effect of confining PVDF polymer to thickness of around 1μm and compare the sensor performance with thicker PVDF film based sensors. The gained insights from developing thin-film PVDF-TrFE based pressure sensors can act as enabling design for the required characterization and development of nanofiber based sensors.

To fabricate nanofibers on a substrate, we will employ and optimize the technique of electrospinning. Electrospinning is a process through which nanofibers are produced under the influence of an electric field. The high electric fields involved in electrospinning result in simultaneous pulling and poling of the fibers [71], resulting in fibers with dipole moments oriented along the length of the fibers. Further, it has been

previously shown that the higher strain gradients and higher electromechanical coupling coefficients associated with nanofibers can result in significantly higher signal output compared to PVDF thin films [72]. In order to create highly sensitive and robust pressure sensors, high density of highly aligned nanofibers were fabricated.

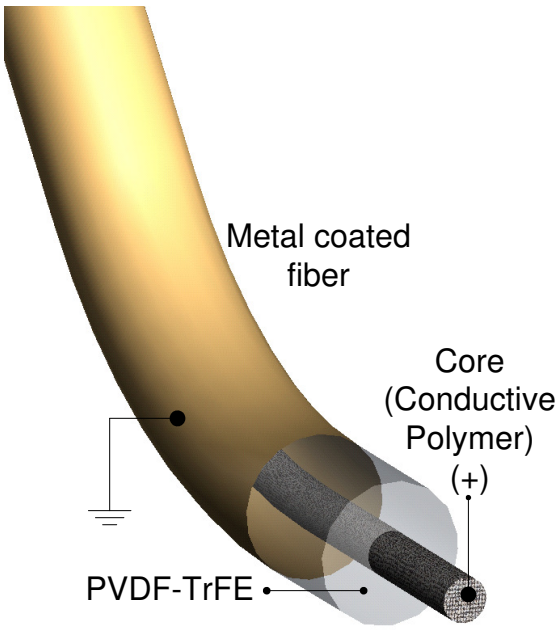

Figure 2.14 Schematic of Novel Core-Shell Electrospun PVDF Fiber showing the sandwiched nature of piezoelectric polymer

Nanofiber based devices tap in to the high electromechanical coupling coefficients to generate higher signal output. However aligned nanofiber based sensors call for extra steps to prevent the effect of stray electrostatic charges interfering with device signals. Further, as the dipole moments are aligned in the direction of the nanofiber, the devices operate in d_{31} mode which is not the most effective excitation

mode. Therefore, using aligned nanofibers is not the most ideal scenario, compounded by the fact that most of the charge is lost due to the high internal resistance of the polymeric fibers.

In order to circumvent the above problem and fabricate highly sensitive sensors, we fabricated core-shell electrospun fibers (Figure 2.14). The core of this fiber was made from conductive polymer (PEDOT:PSS) and the shell was comprised of PVDF-TrFE. After successfully fabricating core-shell structures, thin film of metal was sputtered to form the external electrode. High sensitivity can be expected from these devices due to their higher surface area to volume ratio and d_{33} mode of operation (similar to sandwiched thin film devices, Chapter 3). Further, people have fabricated highly aligned nanofibers in the past [73-75], however, application of core-shell fibers for sensing application has not been explored. Development of versatile sensors that use these core-shell structures can profoundly revolutionize the catheter development, especially for trauma care surgery.

2.5 SUMMARY

In the present chapter, we described the history of pressure sensors for biomedical application and the development of catheters with on-tip pressure sensors. Silicon based pressure sensing technologies have come a long way since its inception in the mid 1950s. Piezoresistive and capacitive based sensing technologies are the most common technologies employed so far for biomedical pressure sensing application.

We also described the operating principle and design of optic fiber based pressure sensing. The disadvantages of conventional techniques for in-vivo pressure sensing can be overcome using piezoelectric polymer based materials. The high-flexibility coupled with the high electromechanical coupling efficiency lends piezoelectric polymer, like PVDF, added advantage over conventional sensing technologies.

Chapter 3: PVDF and Material Characterization

3.1 INTRODUCTION

In this chapter we introduce the structure and properties of PVDF (Poly(vinylidene fluoride)) and its co-polymers. We compare the advantages of using PVDF-TrFE versus PVDF as our starting material for fabrication of our transducers. This chapter also describes the various techniques employed in the present study to characterize the different structures that can be fabricated using PVDF.

3.2 PVDF AND ITS CO-POLYMERS

PVDF exhibits numerous mechanical and electrical properties, such as piezoelectricity, pyroelectricity, nonlinear optical property, etc [64]. Originally, the possibility of PVDF being a ferroelectric polymer was predicted based on X-ray diffraction of the crystal structure, making it the first ferroelectric polymer to be discovered. Ferroelectricity is a property of certain materials which has a spontaneous electric polarization that can be reversed by the application of an external electric field. The distinguishing aspect of PVDF, however, is its associated properties of piezoelectricity. PVDF shows the highest piezoelectricity amongst the synthetic polymers. The effect on its crystalline structure due to nano-confinement fabrication of nanostructures using PVDF is new, however [76, 77]. PVDF is soluble in most of the polar organic solvents, viz. DMF, MEK, THF, DMAc, Acetone etc. Such solubility in a variety of solvents allows fabrication and patterning of PVDF in different shapes and forms. Further, there is huge scope of improvement or modification of PVDF properties by making PVDF composites using various additives [78-83]. In the present chapter, we

touch upon the properties of PVDF as a polymer and one its most widely used co-polymer with TrFE.

3.2.1 Poly(vinylidene fluoride)

Since the PVDF (Poly(vinylidene fluoride)) was observed by Kawai *et al.* in 1969, there have been many researches on PVDF [84-90]. PVDF is one of the semicrystalline polymers with at least three crystalline phases, famous for its pyroelectric, piezoelectric, and ferroelectric properties. Although the chemical structure of PVDF is relatively simple, the monomeric unit has s directionality of CH_2 (head) – CF_2 (tail), which gives the polymer its property of polarization. The PVDF can form a different crystal depending on the condition of the crystallization. These different crystal structures include nonpolar α-phase, polar β- and γ- phase, and so on. Figure 3.1 shows atomic structure of α- phase PVDF and β-phase PVDF respectively.

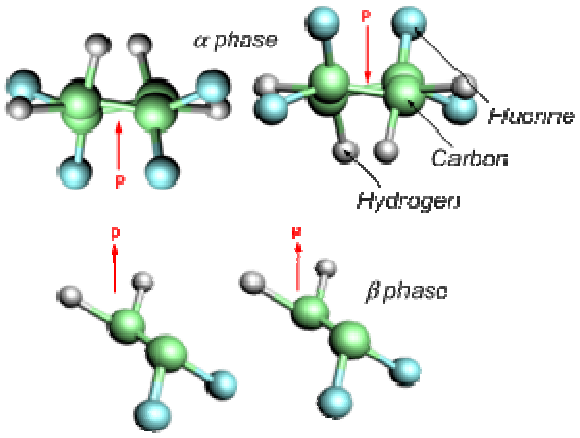

Figure 3.1 Schematic showing the molecular structure and dipole moment orientation of alpha phase, and beta phase of PVDF-TrFE. Permission obtained from [91]

Amongst these phases, β phase is important since it has largest effective dipole moment [70]. The crystal structure for β-phase PVDF show how the dipoles are aligned parallel to each other to create surface charge separation under stress or compression. Due to the random orientation of the dipoles in the α-phase, the dipoles cancel out each other resulting in no net surface charges [92]. When PVDF is cooled from the melt, the crystalline phase formed is the nonpolar alpha-phase with TGTG confirmation. The key to achieving high piezoelectricity of the PVDF polymer is forming β-crystalline phase, which significantly improves sensor and actuator performance. The beta-phase crystal has all transconformation that results in the most polar phase among other crystals, being used extensively in piezoelectric, pyroelectric, and ferroelectric applications. Untreated PVDF itself cannot have β phase without delicate mechanical stretching or electrical poling processes. Efforts to gain β-PVDF easily were connected to compile the consequences of the works, which include the growth from solution, epitaxy on the surface of potassium bromide and crystallization at high pressure. The β-phase is typically obtained by mechanical deformation of melt-crystallized films. Additionally, due to its incompatibility with the standard lithography process, many alternative fabrication methods such as screen printing and shadow mask process [70] have been developed.

Recently Li *et al.* reported the transition from α to β of ultrathin PVDF films prepared by melt state drawing method [93]. However, there exists no other well-defined way of getting β crystal of PVDF than mechanical stretching, which is quite different to be applicable to thin film processes. The γ-phase has similar structure to β crystal, however slightly different TTTGTTTG conformation [94].

Figure 3.2 Schematic showing the dipole moment orientation in an alpha phase (top) and a beta phase (bottom) crystalline domain of a spin-coated (XY plane) PVDF film

Using small angle X-ray scattering, it has been demonstrated previously that the molecular chains are aligned parallel to draw direction for PVDF polymer [95]. Van der Waal's forces predominate in the directions normal to the draw direction whereas the stronger covalent chemical bonds dominate along the chain axis (draw direction). Figure 3.2 shows the cross-sectional schematic of a mechanically stretched PVDF film for alpha phase (top) and beta phase (bottom) crystalline domains.

3.2.2 Poly(vinylidene fluoride)-trifluoroethylene

Tashiro *et. al.* have studied the structure and ferroelectric transitions of PVDF and trifluoroethylene (TrFE) co-polymers [64]. It was found that the crystal structure of

PTrFE is the same as the cooled phase which has the all-trans conformation. This structural model permits the formation of spontaneous polarization in TrFE.

In order to improve crystallization without the mechanical stretching, PVDF-TrFE, a copolymer PVDF, was introduced by [96]. The presence of TrFE in the copolymer of the $PVDF_x$ -$TrFE_{1-x}$ film introduces significant features to the PVDF homopolymer owing to a higher level of piezoelectricity than in PVDF [64]. PVDF/TrFE co-polymers with TrFE content higher than 50mol%, however, ferroelectric nature becomes weak with increasing TrFE content [64]. First, it increases the tendency to crystallize in the polar β-phase without the requirement of mechanical stretching to transform the nonpolar α-phase to the polar β-phase as in the case of PVDF as $0.6<x<0.85$ [66] where the copolymer at composition 75/25 mol. % exhibits the highest piezoelectric responses [95]. Secondly, addition on TrFE as copolymer introduces a defined curie transition temperature, above which the crystal transformation from a ferroelectric to a paraelectric crystal takes place, allows for extrapolation to the PVDF homopolymer, for which no curie temperature has been observed [64].

The forced formation of the polar beta phase by using PVDF-TrFE in place of PVDF has spurred the widespread usage of PVDF-TrFE for novel applications, where poling and mechanical stretching might not be feasible. Thin structures employing PVDF-TrFE find use as novel FETs [97-99], pressure sensors [66, 68, 91, 100, 101], miniature temperature sensors [102-104], ECG monitors [70], iVUS catheters [105-107], etc. A comparison of the different mechanical and electric properties of PVDF-TrFE and other piezoelectric materials is given in Table 3.1.

Table 3.1 Summary of ferroelectric properties of different materials, adapted from [11]

Material	Density (g/cm^3)	Piezoelectric constant, d (pC/N)	Pyroelectric coefficient ($\mu C/m^2K$)	Coupling factor (%)	Youngs Modulus (GPa)
PVDF	1.76	20	40	16	10-12
PVDF-TrFE	1.9	15-30	30-40	20	10-12
PZT-5	7.75	171	60-500	34	60-120
Quartz	2.66	2	-	9	-

3.3 QUALITATIVE MATERIAL CHARACTERIZATION

In order to assess the properties of the structures fabricated from PVDF, we used various material characterization techniques. Qualitative techniques provide us with information about the quality of structural morphology, distribution of crystalline domains, and elemental composition. Some of the qualitative techniques used in the present study for analysis of PVDF structures are:

3.3.1 Cross polarized microscopy

PVDF is a birefringent material that interacts differentially with differently polarized light. It is due to this property of PVDF that anisotropic crystalline structures of PVDF can be easily observed using cross-polarized microscopy. Cross-polarized microscopes uses two linear polarizers, on either side of the sample, aligned perpendicular to each other. Therefore, all the source light (background) appears dark in such an image. The portion of this beam that interacts with the crystals of PVDF ends up bending to differential refractive index of the material (sample). Thus, all the crystalline domains in such a sample appear bright colored.

Figure 3.3 Cross-polarized microscopy images of a commercial PVDF-TrFE (10µm) film observed at different magnifications. The images show highly crystalline regions near the edges of the PVDF film

Cross-polarized microscopy is an easy technique to study the crystalline orientation and grain size of the sample. Further, it can also be used to qualitatively determine what percentage of the structure might be crystalline in nature and how the crystalline domains might be distributed in a sample. Figure 3.3 and Figure 3.4 shows cross-polarized microscopy images obtained for commercial PVDF-TrFE films at different magnifications.

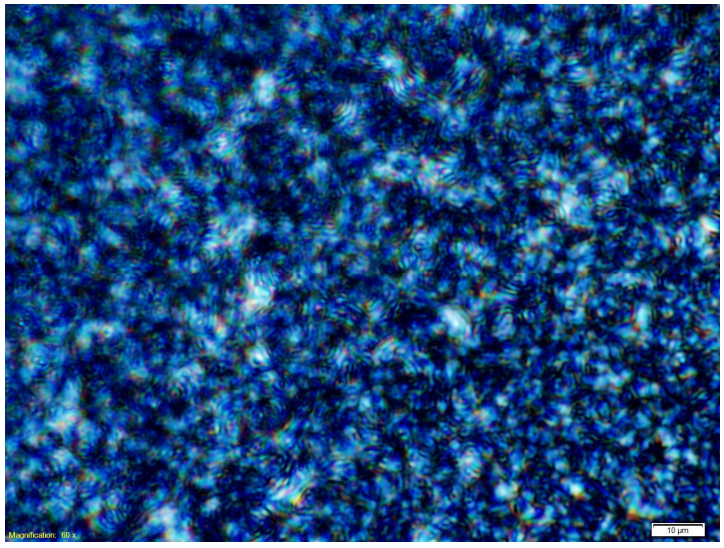

Figure 3.4 Cross-polarized microscopy image of a commercial PVDF-TrFE (10µm) film observed at 60x

3.3.2 FTIR Spectroscopy

Fourier transform infrared spectroscopy (FTIR) is a technique which is used to obtain an infrared spectrum of absorption or transmission of the sample under question [85]. Since PVDF is a piezoelectric polymer, the dipole moments in PVDF structure exist due to certain orientation of the fluorine atoms with respect to the carbon atoms. Using FTIR, it is easy to detect the molecular orientation of these dipoles from the fingerprint spectra of its absorbance characteristics.

Typically, several scans (250 scans) are performed on the sample at a scan rate of $2cm^{-1}$ for higher sensitivity from thin samples. In order to collect highest signal possible from the fabricated thin films or nanofibers, FTIR spectroscopy was done in grazing angle incidence mode, rather than transmission mode.

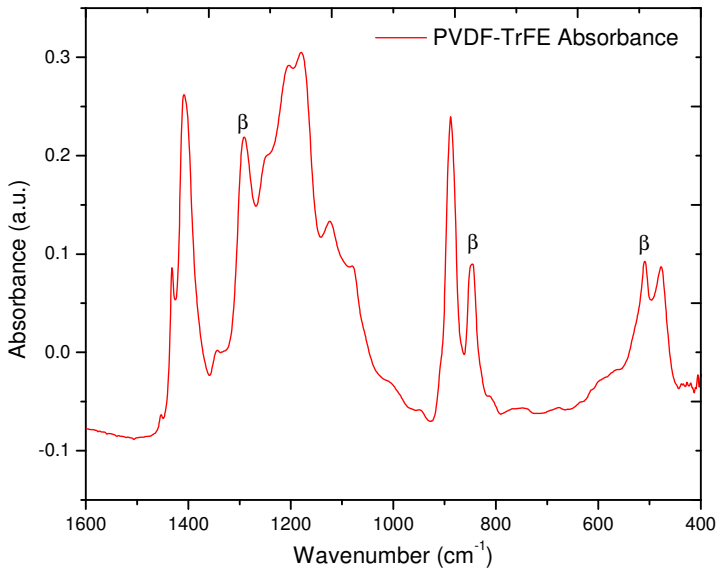

Figure 3.5 FTIR spectrum obtained for a PVDF-TrFE thin film under grazing angle incidence reflection mode

Figure 3.5 shows a typical FTIR spectra observed for a PVDF thin film in grazing angle incidence reflection mode. Whereas Figure 3.6 shows the FTIR spectra obtained using the same sample in transmission mode. A quick comparison of the two graphs shows the similar fingerprint spectrum observed with a difference in the beta phase peak intensities (observed around 511, 840 and 1290cm^{-1} [85, 93, 108]). Therefore, grazing angle incidence reflection mode gives better information about the beta phase structure, compared to the transmission mode.

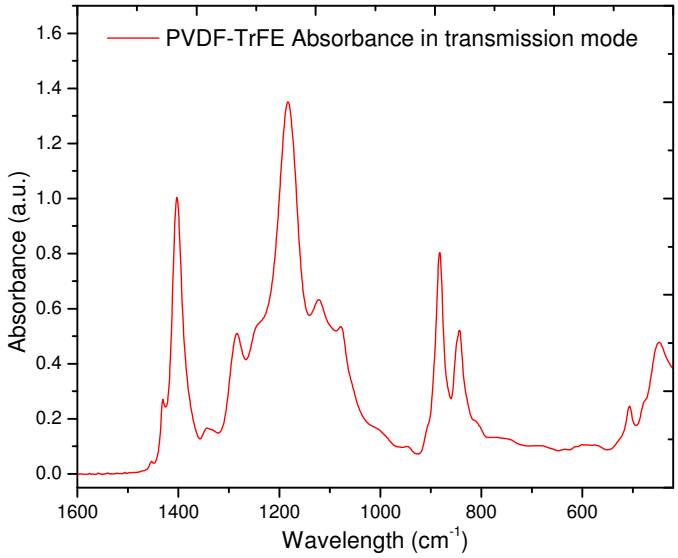

Figure 3.6 FTIR spectrum obtained for a PVDF-TrFE thin film in transmission mode

3.3.3 Raman Spectroscopy

Raman spectroscopy is a complimentary technique to FTIR spectroscopy that uses a laser to study vibrational, rotational, and other low-frequency modes in a polymer

[108]. The laser light interacts with molecular vibrations, phonons or other excitations in the polymer, resulting in the energy of the laser photons being shifted up or down.

In the present study, sample for raman spectroscopy was spin coated on an aluminium disk. Raman spectroscopy was done using Renishaw InVia Raman spectroscope using green laser (514.4 nm) with exposure set to 30 seconds.

3.3.4 Scanning Electron Microscopy

Scanning electron microscope (SEM) produces images of a sample surface with a focused beam on electrons thermionically emitted from a gun [109]. SEM is capable of reveling important morphological features and overall structure of the micro or nano sized particles with great resolution.

Patterned nanofibers or film surface morphology was imaged using scanning electron microscopy. For all PVDF based samples, metallic coating of gold-palladium was done on the sample to avoid charging of the samples. Figure 3.7 shows a SEM image obtained from a PVDF electrospun fiber.

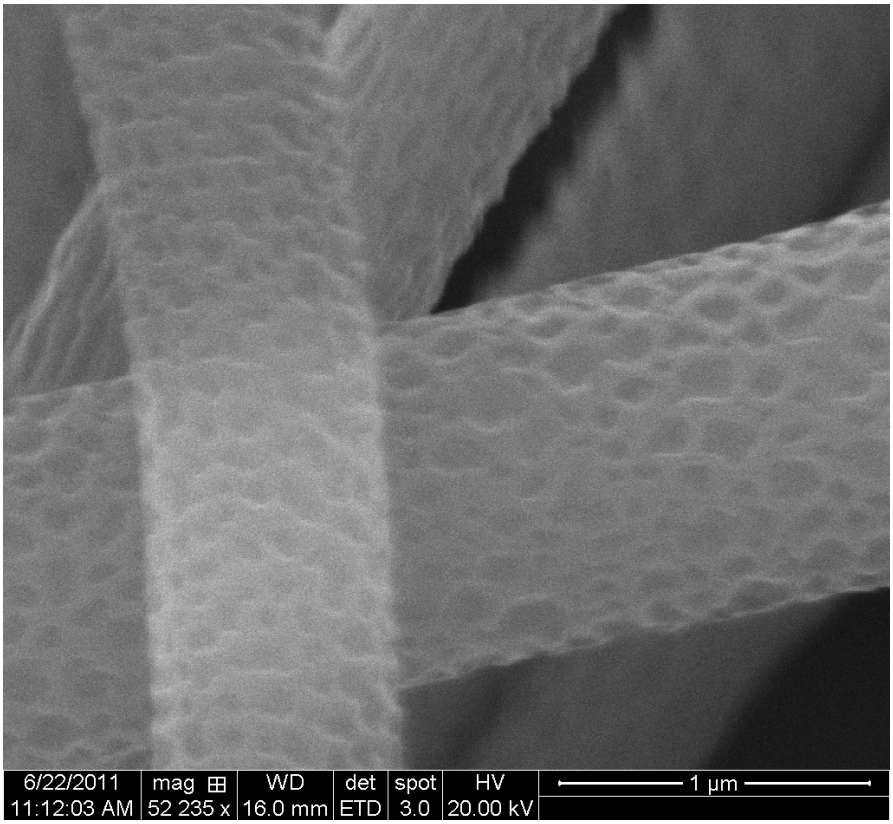

Figure 3.7 SEM image of a PVDF fiber electrospun using 20% (w/v) PVDF solution from MEK

3.3.5 Transmission Electron Microscopy

Transmission electron microscopy (TEM) is a technique that uses a beam of electrons to pass through a very thin specimen sample [110]. The image that is formed is a result of the interaction of the electrons transmitted through the specimen. TEMs are capable of imaging higher resolution that helps resolve fine details such as single nanoparticles.

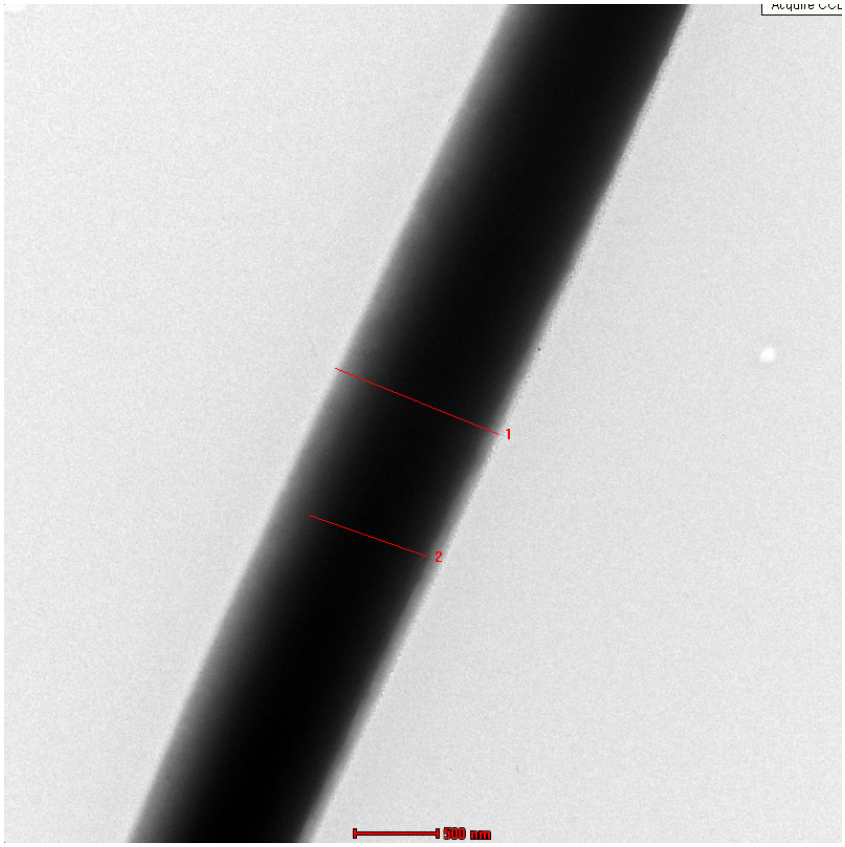

Figure 3.8 TEM image showing a core-shell electrospun fiber. The core and the shell show distinct contrast due to the differential interaction with the electron beam. (Core = PMMA, Shell = PVDF)

For TEM imaging of an electrospun structure, the fibers were directly electrospun on top of TEM grids. The TEM grids were placed on the current collector (Chapter 4) surface. In order to avoid the charging of the fibers due to the electron beam, we used finer mesh TEM grids (400 or higher, TedPella) coated with carbon and fomvar. Carbon coating on the TEM grids help stabilize the fibers. Sometimes, if the fibers under observation in a TEM are big (>1µm in diameter), the fibers might be ribbons. Additionally, SEM imaging can reveal the surface morphology or structure of the fibers.

3.3.6 Energy-dispersive X-ray spectroscopy

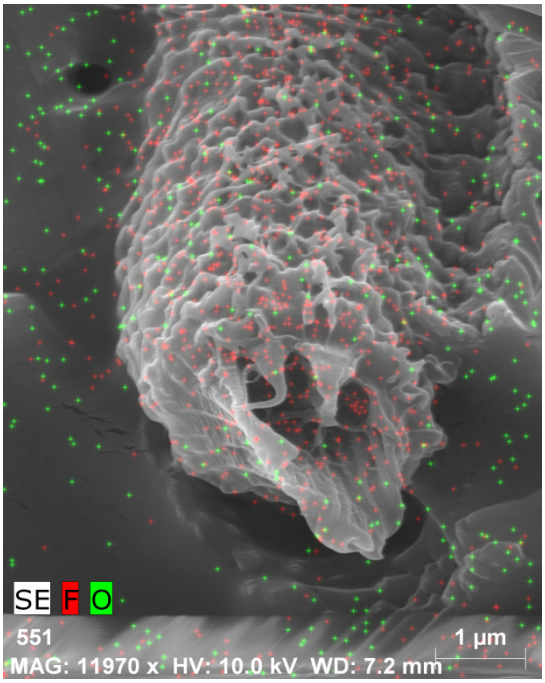

Figure 3.9 Photograph showing EDS imaging of PVDF fiber (fluorine atom) over a SEM image of the same

Energy dispersive X-ray spectroscopy relies on the use of x-ray excitation for elemental detection. Combined with the SEM or TEM instrument, EDS is capable of hypermap imaging of structures along with elemental analysis simultaneously. EDS uses raster scanning methodology to detect for the desired element. Figure 3.9 shows such a map of fluorine atom detection using EDS coupled to SEM imaging system.

3.3.7 Laser scanning confocal microscopy

Laser scanning confocal microscopy (LSCM) combines the capability of a confocal microscope to selectively focus at a certain depth along with excitation using an

external laser for fluorescence imaging [111]. This allows for easy imaging of all the fluorophores in a single plane to be viewed simultaneously. Also, by automating the focal plane control, it is possible to obtain fluorescence information at different z-positions though the sample and reconstruct digitally for assembly of a 3D figure.

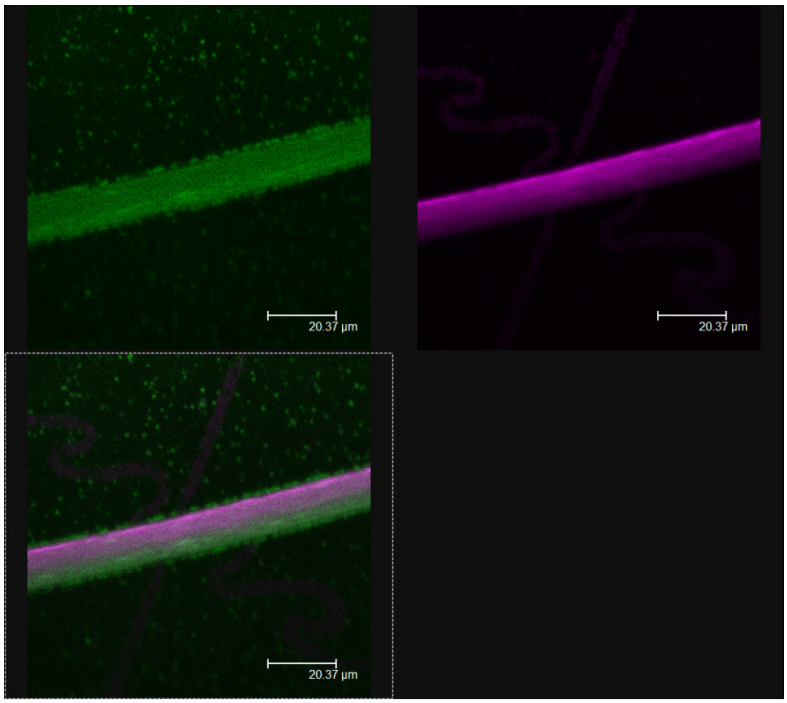

Figure 3.10 Photo showing a core-shell electrospun fiber images using LSCM (Core = PMMA and fluorescein from MEK; Shell = PVDF and rhodamine B from DMF)

Figure 3.10 shows a LSCM image obtained from a core-shell fiber using two different fluorescent dyes added to the different solutions used to fabricate the structure. Fluorescein (shown in green) is a yellow dye and rhodamine B (shown in purple) is a red dye by nature. Therefore, two different lasers (Argon laser) were used to excite the respective fluorophores close to their excitation wavelengths. The emission is then

collected using different photomultiplier tubes (PMT) and converted to intensity maps, which are artificially colored. The two maps are then overlapped to create a composite image of the sample.

3.4 QUANTITATIVE

While qualitative techniques are important to get an idea about the nature of the structure fabricated, it is very important to be able to compare two samples quantitatively for reasonable prediction of the expected output. Quantitative analysis techniques can help us compare the percentage of crystallinity between two samples by determining the absolute crystallinity of the sample under observation. Some of the quantitative techniques used in the present study are:

3.4.1 Differential scanning calorimetry

Differential scanning calorimetry (DSC) measures the amount of heat required to raise the temperature of the PVDF sample, plotted as a function of the sample temperature. The amount of heat consumed or released by the sample is analyzed by comparing with a reference, which is maintained at nearly the same temperature as that of the actual sample [112].

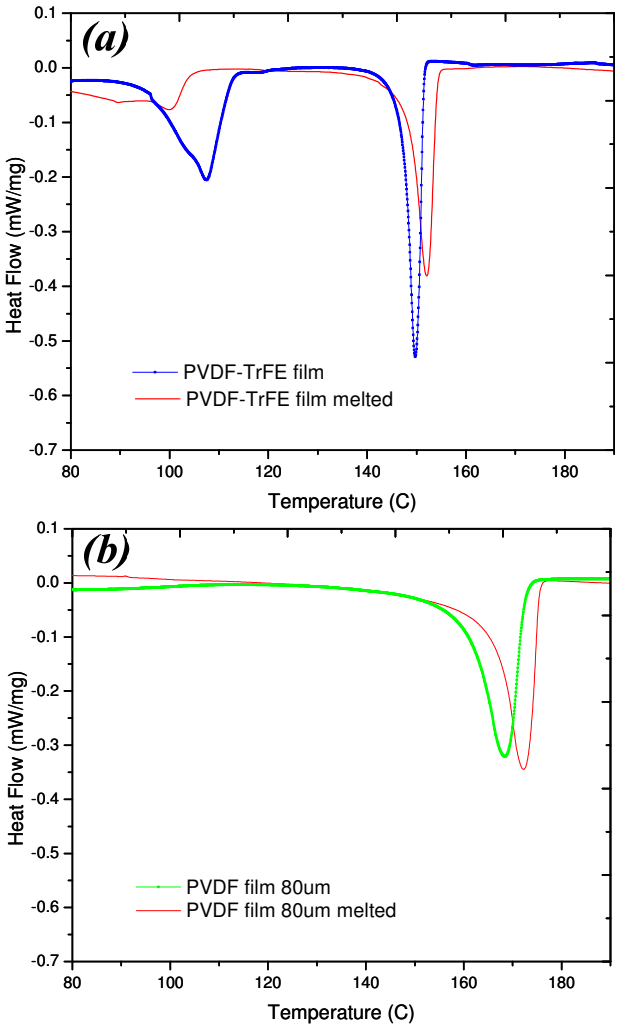

Figure 3.11 Weight normalized DSC curves of (a) commercial PVDF-TrFE film, and (b) commercial PVDF film

DSC can reveal very important information about polymers like the melting temperature, crystallinity of the film, and curie temperature of piezoelectric polymers. All the DSC curves are normalized by the weight of the sample for comparison, as shown in Figure 3.11. From Figure 3.11a, we observe the melting point of PVDF-TrFE films to be

around 150ºC and the melting point of TrFE to be around 110ºC. There is no similar melting peak observed for commercial PVDF film in Figure 3.11b. Further, the area under the curve and peak characteristics gives us a measure of the film crystallinity. Sharper and higher magnitude peaks, as in Figure 3.11a for PVDF-TrFE film, indicates higher crystallinity in a PVDF-TrFE film when compared to a melted PVDF-TrFE film.

3.4.2 Electrical hysteresis

Electrical hysteresis involves charging one of the electrodes of a PVDF film using an external power supply. Such a charging of the PVDF film causes generation of charge on the surface of the film, which can be measured using a charge amplifier connected to the other electrode of the PVDF film. The output from the charge amplifier is fed to a data acquisition system along with the input voltage. A schematic of the setup is shown in Figure 3.12.

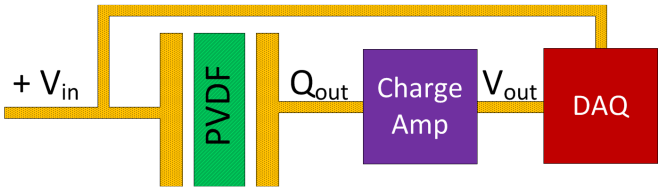

Figure 3.12 Schematic of hysteresis setup

Quantification of the charge generated by PVDF film as a function of the input voltage can be used to determine the percentage crystallinity of the PVDF film. Figure 3.13 shows the electrically hysteresis done on PVDF film at different voltage sweep frequencies. It was found that 100mHz works best for measuring electrical hysteresis of

the film. Further, the y-intercept of the electrical hysteresis loop is a direct measurement of the remanent polarization in a PVDF film.

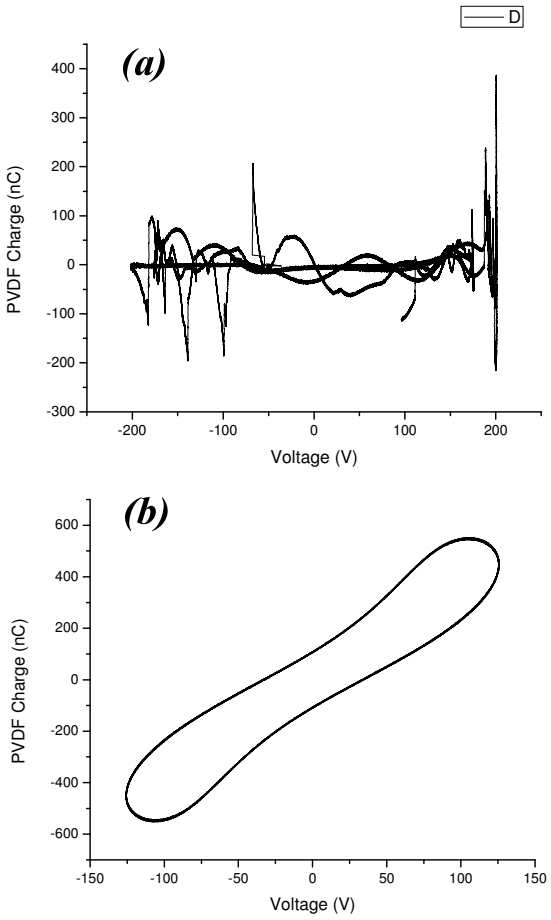

Figure 3.13 Electrical hysteresis of PVDF film carried out at (a) 10mHz, and (b) 100mHz voltage sweep

Using the value of the remanent polarization for the sample, film crystallinity can be easily calculated using the following:

$$Fraction\ of\ film\ that\ is\ crystalline = \frac{P_r}{165mC/m^2}$$

Where, Pr is the remanent polarization (or y-intercept) obtained from the sample, and 165mC/m^2 is the polarization of a PVDF film if the entire film was crystalline in nature [95].

3.5 SUMMARY

In the present chapter, we compared and contrasted the properties of PVDF and PVDF-TrFE and concluded that PVDF-TrFE offers the flexibility of fabricating novel nanostructures without the need for any additional mechanical stretching or poling. Therefore, PVDF-TrFE will be used in the present study.

We also discussed the various qualitative and quantitative techniques that can be used to analyze the properties of PVDF-TrFE based structures. These techniques, combined together, can provide in-depth insight on the molecular orientation and additional modifications that can be made to boost the pressure sensor's sensitivity.

Chapter 4: Fabrication of PVDF-TrFE Structures

4.1 INTRODUCTION

In this chapter, we introduce the fabrication techniques for PVDF based structures. In particular, we fabricated PVDF into three different form factors: (a) Thin-films (1µm), (b) Highly aligned nanofibers, and (c) Highly aligned core-shell nanofibers. These structures were fabricated using standard clean-room compatible techniques. The compatibility of the fabrication structures with most of the existing silicon microfabrication techniques ensures the future opportunities of the sensor fabrication on a large scale.

In addition to fabrication of these PVDF structures, material characterization was also done for each individual form factor. Thin-film characterizations were done in great details to compare the reported fabrication techniques with the commercial techniques for highly crystalline PVDF structures. Ensuring high crystallinity in thin-film structures enables fabrication of highly sensitive sensors. In pursuit of fabrication of highly sensitive, yet compact sensors, 1µm thin films were studied and compared against thicker (conventionally fabricated) PVDF films.

Fabrication of nanofiber structures using PVDF for sensing application is relatively new [71]. Therefore, in the present study, some of the characterization

techniques used for PVDF thin-films were extended for nanofiber based structures as well. We further discuss the custom built setup employed for the fabrication of the desired nature of nanofibers.

4.2 REVIEW OF PVDF BASED STRUCTURES

Thick PVDF or PVDF-TrFE films have been fabricated conventionally. Due to the resonance frequency of the material lying in kHz to MHz region, PVDF has been exploited towards ultrasound transducer applications [64, 95, 113] and high frequency sensors, like hydrophones, pyroelectric sensors, etc [95]. For all these applications, the aim is to acquire noise free, high quality signal, which is usually achieved using high surface area in thin film format. Further, since these applications required the film to be highly durable, thick PVDF films (100µm – several mm) were typically used.

Focus towards using thin-films is a very recent trend, fuelled by the IC chip industry, to exploit the high-k dielectric nature of the PVDF thin films. Films as thin as sub-100nm have been employed for this purpose.

Recent studies have also highlighted the importance of PVDF based nanofibers [77, 114] over thin films. In the present chapter, we report the characterization and properties of all the above mentioned structures. Later in the chapter, we introduce novel core-shell structures, fabrication and characterization of the same.

4.3 SPIN COATING OF PVDF-TRFE THIN FILMS

The spinning process is of primary importance to the effectiveness of pattern transfer. The quality of the PVDF film determines the density of defects transferred to the device under construction. The application of too much PVDF solution results in edge covering or run-out, hillocks, and ridges, reducing manufacturing yield. Too little solution may leave uncovered areas.

Different concentration solutions of PVDF-TrFE in methyl-ethyl-ketone (MEK or 2-butanone) were prepared by dissolving the appropriate quantities of PVDF-TrFE (70:30) powder overnight on a magnetic stirrer at 40 ºC. For the present study, three different solutions, having PVDF-TrFE concentrations of 8 %, 15 %, and 20 % weight/volume in MEK, were prepared. The resulting solution is optically clear by nature. About 1mL of this prepared solution is dispensed on a 4" wafer to spin-coat the entire wafer surface. The spin coating recipe used consists of two important steps: (a) ramp (acceleration) at 500rpm/s for 10s; and (b) rotation at 1000rpm for 30s, to result in a smooth and uniform film.

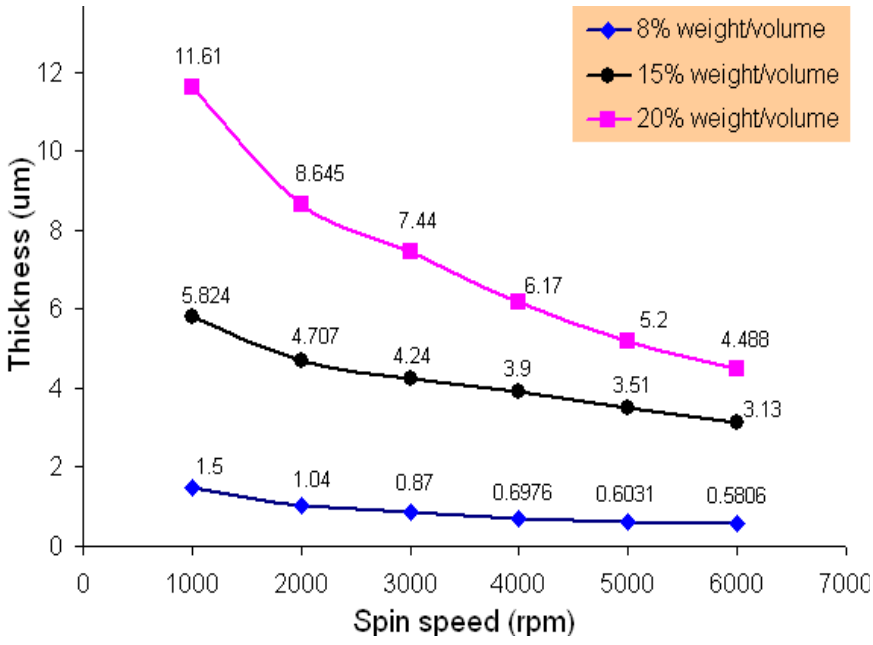

Figure 4.1 Film thickness vs. spin speed with various weight/volume in MEK solution

Figure 4.1 shows film thickness for PVDF-TrFE films that was obtained using different solution concentrations, versus spin speed. The film thickness decreased as spin speed increased.

In the present study, and for material characterization, we used 8 % w/v PVDF-TrFE copolymer with 2000 rpm for 30 sec to get 1 μm thickness and 20 % w/v PVDF-TrFE at 4000 rpm for 30 sec to get 6 μm thickness. The surface of the fabricated films can be imaged for presence of pin holes using SEM (scanning electron microscopy) or AFM (atomic force mircroscopy). Figure 4.2 shows the SEM images showing defect free PVDF-thin-films spin coated on the surface of a silicon wafer.

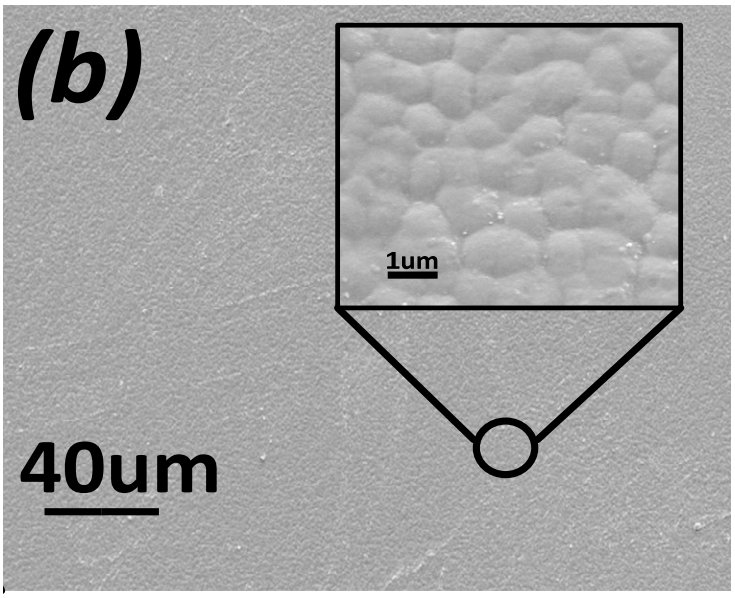

Figure 4.2 SEM image showing the defect-free surface of the fabricated PVDF film

The surface properties of the spin-coated PVDF films were found to be similar when the silicon substrate was replaced with kapton (polyimide) film. This enabled ease of film fabricated procedure to flexible films, which was necessary for the flexible devices fabrication (Chapter 5).

The fabricated PVDF films showed poor adhesion on the silicon substrate. The film was cured in vacuum oven at 130 ^{o}C for 5 hours for strong adhesion. Figure 4.3 *(a)* shows the SEM images of 20 % w/v PVDF-TrFE, showing poor adhesion on the silicon substrate under regular heat treatment and Figure 4.3*(b)* 8 % w/v PVDF-TrFE, shows the strong adhesion under vacuum oven heat treatment.

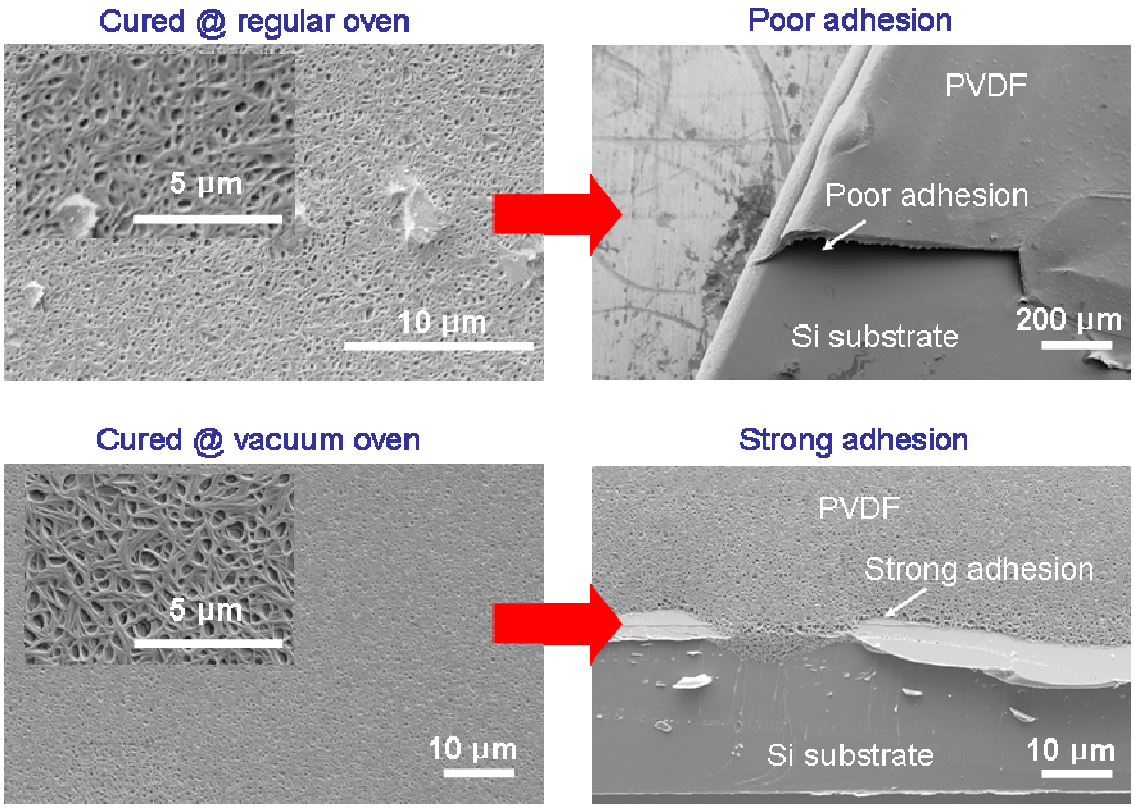

Figure 4.3 SEM images of PVDF-TrFE thin film on substrate. (a) 20% wt PVDF film showing poor adhesion under regular heat treatment; and (b) 8% wt PVDF film, showing strong adhesion under vacuum-oven heat treatment

4.4 CRYSTALLINITY OPTIMIZATION

As describe before (Chapter 3), PVDF is a semi-crystalline material and may exhibit any of its four phases, α, β, γ, and δ. Amongst these phases, β phase is important since it has largest effective dipole moment [70]. The key to achieving high

piezoelectricity of the PVDF polymer is forming β-crystalline phase, which significantly improves sensor and actuator performance. Thus there are two important parameters on which the final sensor performance could be dependent: (a) crystallinity of film, and (b) percentage of β phase crystalline. For a highly sensitive pressure sensor fabrication, it is important not only to fabricate highly crystalline PVDF films, but also that most of those crystalline domains exist in β phase. The crystallinity of the PVDF films can be affected or altered by one of the following: (i) mechanical stretching, (ii) annealing temperature, (iii) solvent, or (iv) poling.

4.4.1 Mechanical stretching

In the present case, due to the nature of the thin films fabricated, it is difficult to peel off the thin films form the substrate for further mechanical stretching. Therefore, we analyzed the effect of stretching PVDF films due to spin-coating of the samples. To analyze the impact of mechanical stretching on film crystallinity, we investigated the difference in different film thicknesses using FTIR, Raman spectroscopy and DSC.

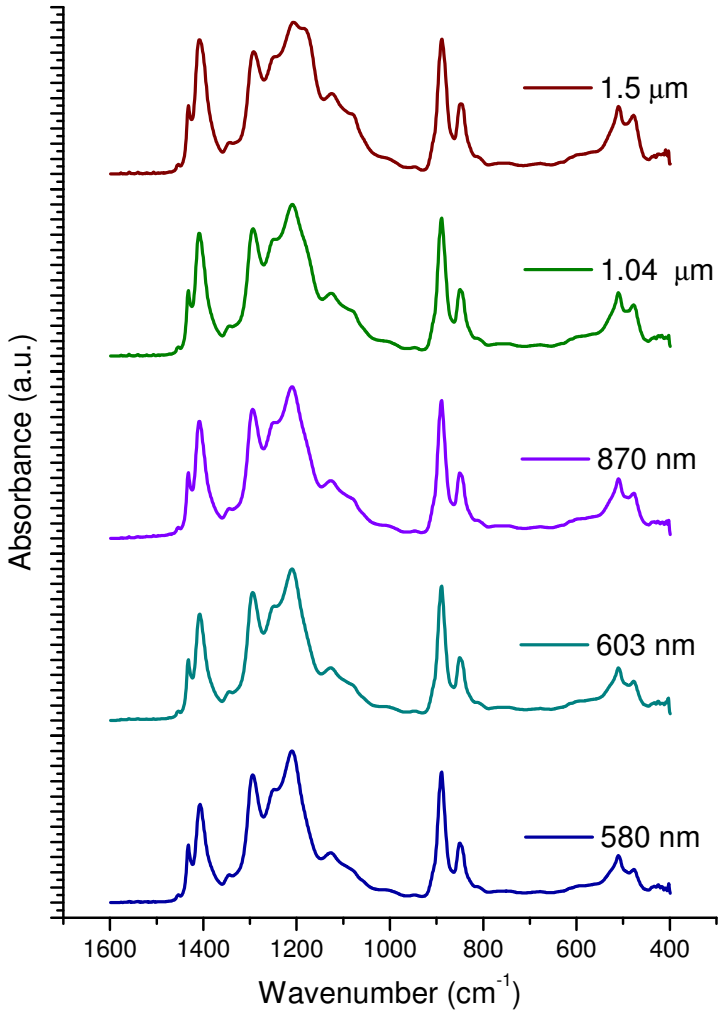

Figure 4.4 Plot showing similar FTIR spectrum obtained for different thicknesses of PVDF films

Figure 4.4 shows the FTIR spectrum for the different PVDF films fabricated in the present study. All the spectrum were normalized with respect to the 1400cm^{-1} peak. Comparison of the spectrum obtained from different samples indicates minimal difference in the crystalline structures of the different films. Previously, published reports have indicated an increase in crystallinity with confinement of PVDF structures [ref].

However, there are two main differences between such studies and the present work: (a) those studies involving increase in the PVDF crystallinity used PVDF as the starting material whereas in the present study, we have used PVDF-TrFE co-polymer; and (b) the studies reported changes in crystallinity for sub-100nm feature sizes fabricated out of PVDF whereas in the present study, fabrication of thicker structures (1µm) films would give us the desired sensitivity for pressure sensing applications.

Figure 4.5 showing the Raman Spectroscopy peaks for two different PVDF film thicknesses are highly distinct. We notice a clear sharpening in the β-phase crystal phase (840 cm^{-1}) on curing the 1µm and 6µm thick PVDF-TrFE films. Further, we notice that the α-phase crystals (800 cm^{-1}) in the PVDF-TrFE films decreases or get eliminated as the film is annealed at 110ºC. This phenomenon has also been reported elsewhere [108]. The intensity of the peak from PVDF absorbance (1430 cm^{-1}) remains unaltered, however.

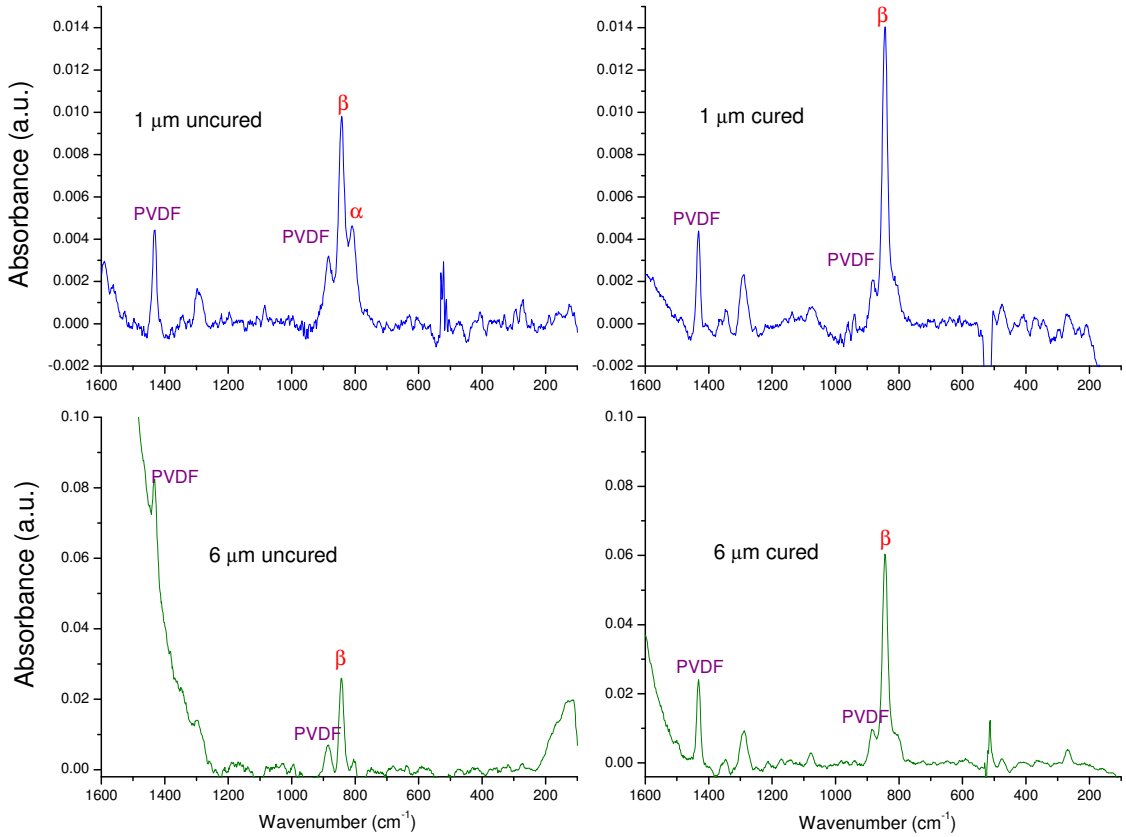

Figure 4.5 Raman Spectroscopy measurements for the various PVDF-TrFE films used in the present study, showing enhancement of beta phase on curing of films

Raman spectrum shows mainly the presence of the β-phase crystal domains throughout the films. Less noticeable, however, is the presence of the α-phase crystal structures also. Further, from raman spectroscopy, we can determine the percentage of PVDF:TrFE from the absorbance information (Chapter 3). By finding out the absorbance of PVDF at 1430cm^{-1} and TrFE at 1297cm^{-1}, we estimated the molar ratio as:

$$\text{Percentage of PVDF:TrFE} = A_{1430}/(A_{1430}+A_{1297}) = 70:30$$

From the above information, we obtained the molar ratio of PVDF:TrFE (70:30), as expected.

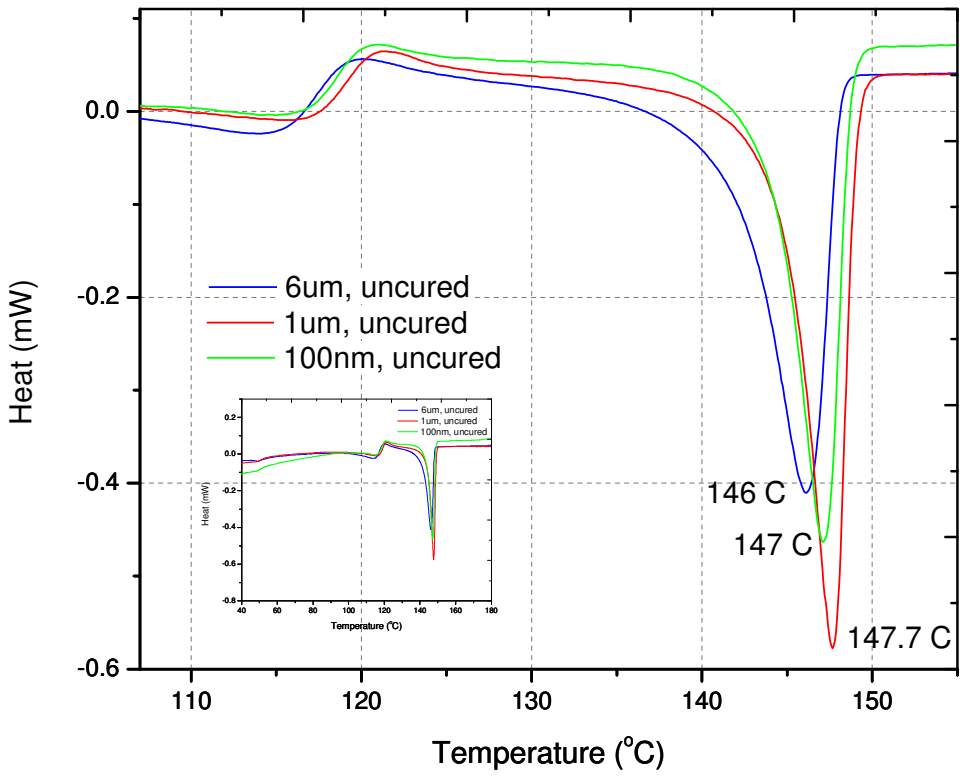

Figure 4.6 Plot showing the weight normalized DSC curves of PVDF-TrFE films for different thickness. Inset shows the entire DSC spectrum

It is easy to compare the overall crystallinity of a polymer using Differential scanning calorimetry (DSC) results. Figure 4.6 shows higher crystallinity obtained from 1µm thick PVDF films compared to 6 µm and 100nm films. Further, we also see the representative curve for curie temperature (T_c) for PVDF-TrFE at 118ºC. Curie temperature is the temperature, which when exceeded, the piezoelectric material losses its piezoelectricity. The second peak, around 147ºC, corresponds to the PVDF melting peak.

Sharpness of this peak and higher area under the curves are representative features of highly crystalline polymers. Therefore, 1µm films were found to have the highest crystallinity amongst the different PVDF films studied.

4.4.2 Annealing

Annealing process involves heating the samples to a certain temperature in order to provide the structures sufficient energy for molecular re-orientation, releasing stress involved due to spin-coating or increased adhesion. As we showed above (Figure 4.3), heating the PVDF films increases adhesion to the silicon substrate. Since the T_c for the spin coated PVDF films in the present case was 118ºC, we annealed our PVDF films at 110ºC, to avoid any loss in polarization due to high temperatures. The films were annealed at 110ºC for 1h inside a controlled oven. Figure 4.7a shows the DSC curve comparing 1µm and 6µm cured PVDF films. The plot still shows higher crystallinity observed from 1µm thick film compared against the 6µm film. Even though we found higher crystallinity from 1µm cured film, this does not imply that annealing of PVDF at 110ºC is beneficial for the prepared samples. Figure 4.7b shows the DSC curve for a melt sample of PVDF showing the loss in polarization (Tc = 118ºC) of PVDF films upon recrystallization.

The curie transition peak was found to be replaced with the melting peak for TrFE. In order to systematically study the effect of annealing on PVDF, it is important to compare the effects on the same sample. The effect of different annealing temperatures

on 1µm PVDF thin film was studied using FTIR and the results have been plotted in Figure 4.8.

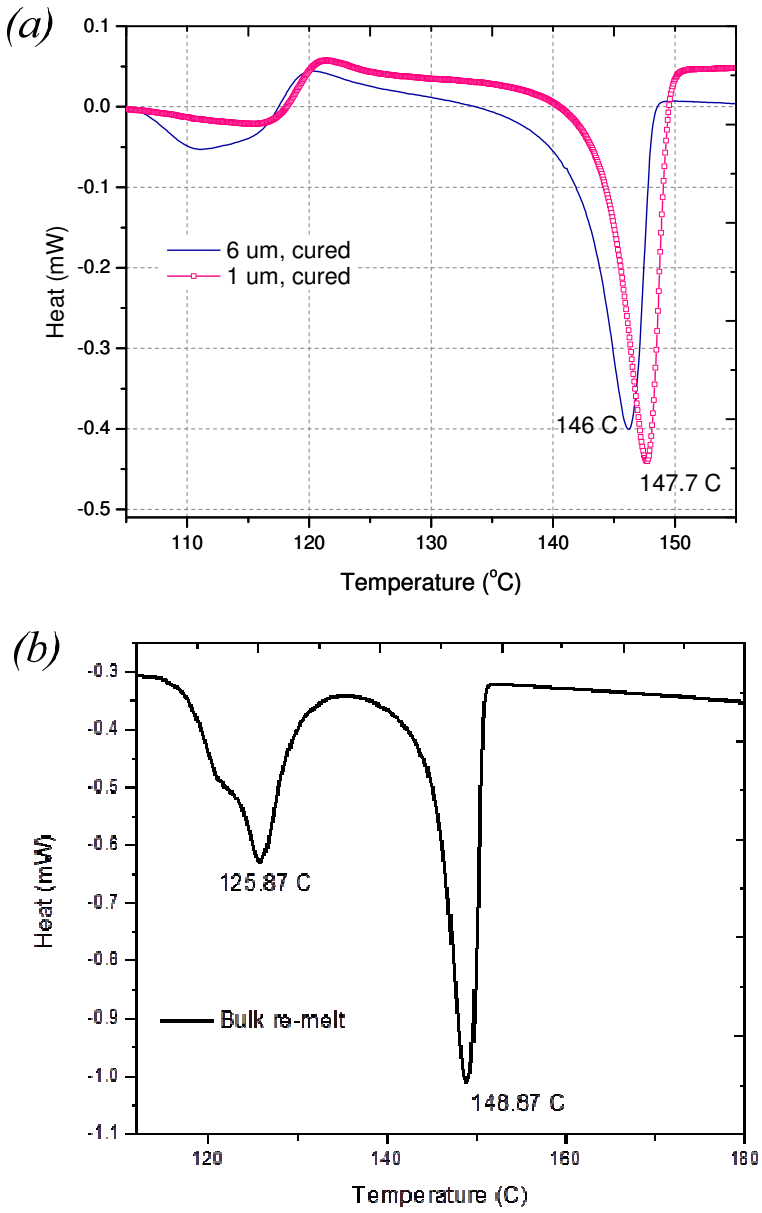

Figure 4.7 Weight normalized differential scanning calorimetry (DSC) measurements: (a) comparison of a 6µm thick PVDF films versus a 1µm thick PVDF film with higher crystallinity obtained from 1µm thick films; and (b) heat flow in a melted PVDF film

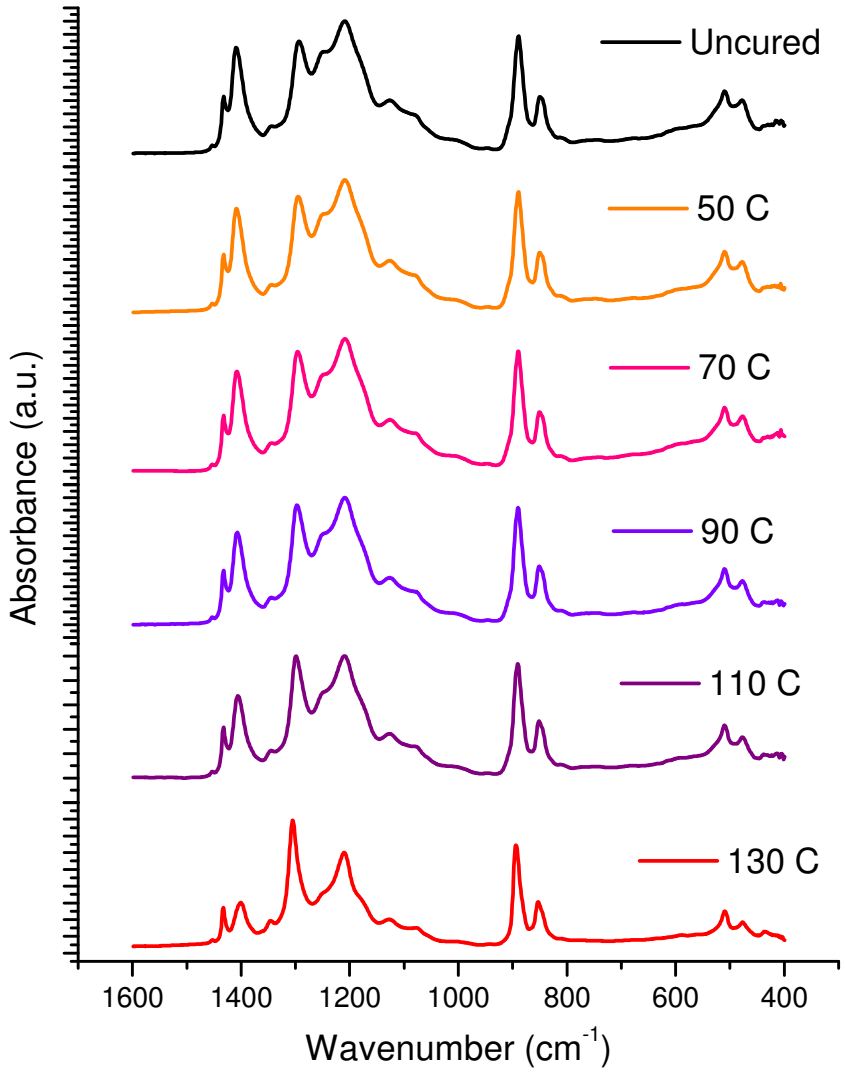

Figure 4.8 FTIR plots lot of 1µm PVDF film annealed at different temperatures

These FTIR plots were normalized with respect to the peak at 1200cm^{-1}. From the plots, an increase in the beta phase crystalline structure (absorbance at 1290 cm^{-1}) was observed with increase in temperature. Films annealed at 130ºC showed the highest crystallinity amongst all the samples. However, such high annealing temperature was

above the curie temperature of PVDF and was therefore, not a preferred annealing temperature.

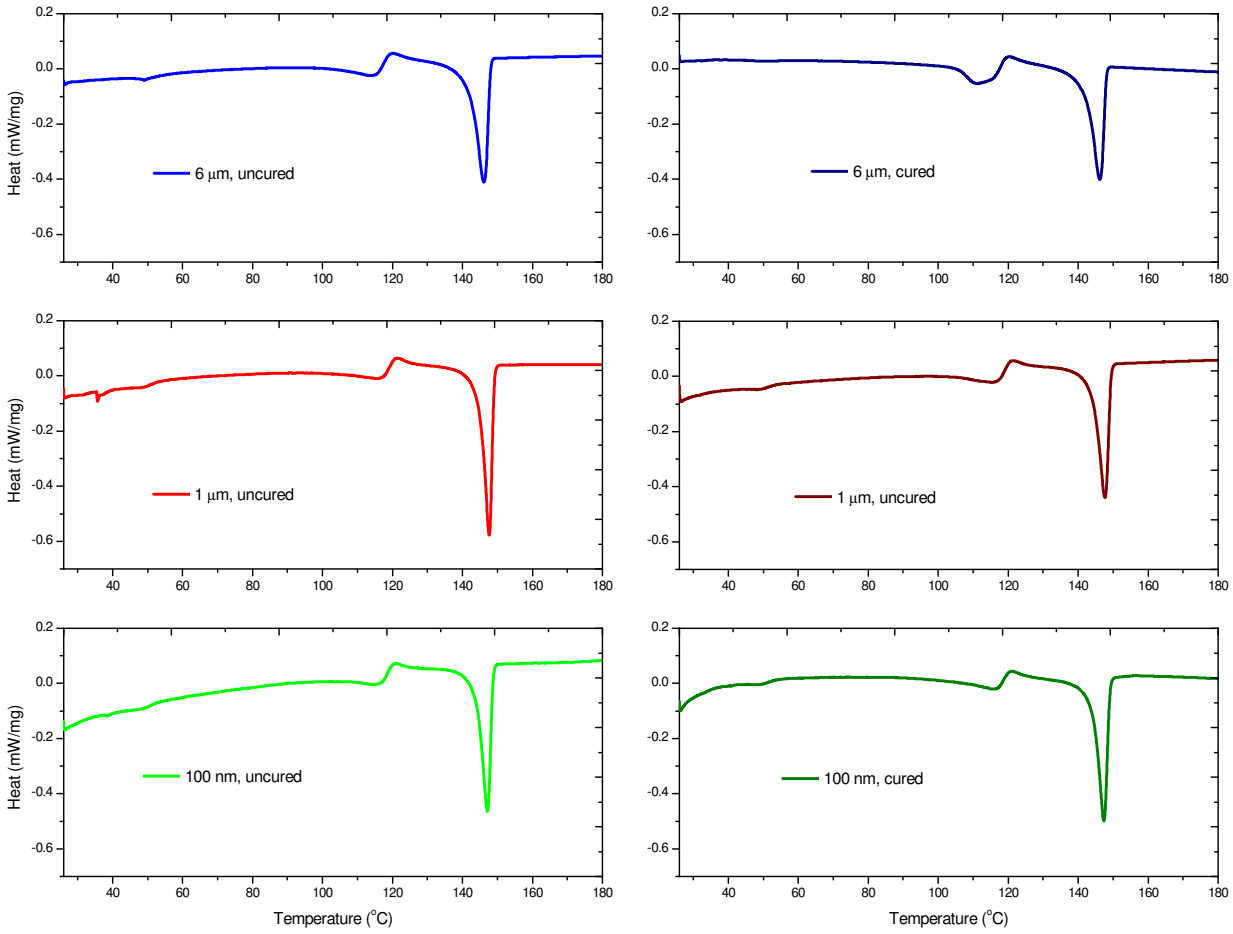

Figure 4.9 Plots of weight normalized DSC curves for cured and uncured PVDF films of different thickness (6μm, 1μm and 100nm)

A quick comparison of the different films annealed at 110ºC is shown in Figure 4.9. From the plots, we notice there is a slight decrease in the area under the curve for the 1µm thick film after annealing. The other films do not show any difference in the cyrstallinity on annealing, however. Combing the information from Figure 4.8 and Figure 4.9, we can conclude that annealing of films might not substantially increase the crystallinity of the film. Annealing, however, does show an increase in the beta phase structure of the spin-coated PVDF films.

4.4.3 Solvent

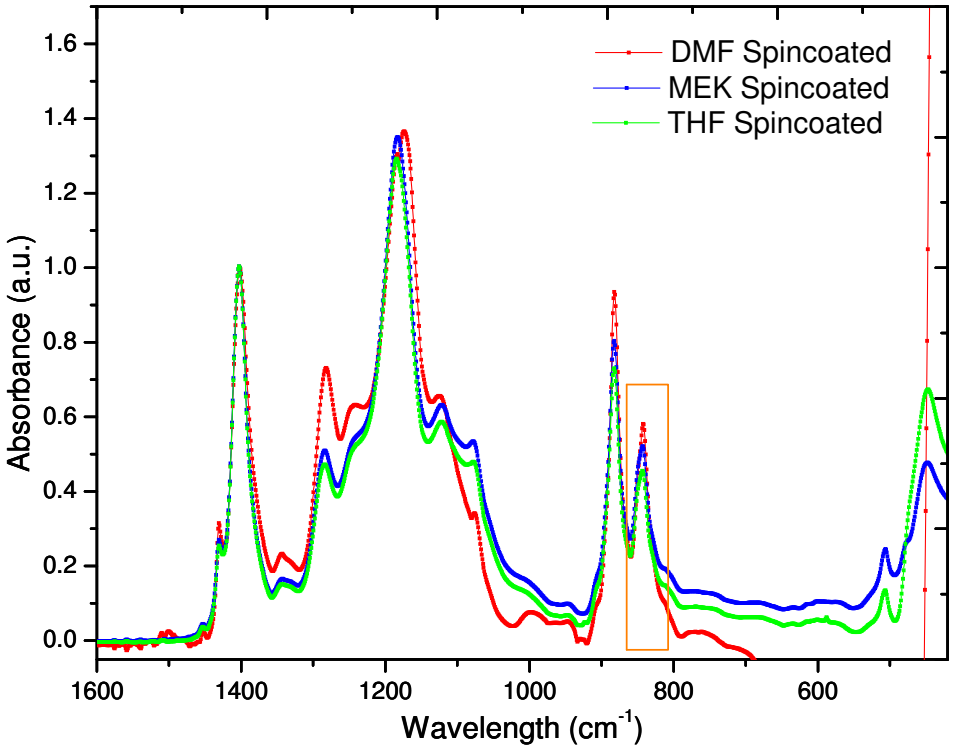

Figure 4.10 FTIR plots for PVDF films spin coated using different solvents: DMF, MEK and THF. The plots are normalized with respect to the 1400cm^{-1} peak and show similar beta phase crystalline structures for different solvents used in the fabrication of PVDF films.

The rate of evaporation of a solvent can force the formation of a specific crystalline phase. We used four different solvents to spin-coat PVDF films: DMF (dimethylformide), MEK (methylethyleketone, THF (tetrahydrofuran) and Chloroform. 8% w/v PVDF solutions were prepared using the above four solvents. Out of the four solvents, chloroform was highly volatile to result in a uniform film. The remaining solutions were used to spin coat on a copper coated substrate and analyzed using FTIR spectroscopy. Figure 4.10 shows there was minimal difference in the beta crystalline phase ($840cm^{-1}$, $1290cm^{-1}$) due to the change in the solvent used. The uneven nature of the DMF spincoated sample was due to the poor nature of the sample and due to introduction of baseline correction in the data.

Even though there was minimal difference in the beta phase of the PVDF films, the use of a particular solvent can have a significant impact on the crystalline structure of PVDF, as reported previously [refs: solvent effect]. In the present study, we compared the crystallinity of drop casted films versus spin coated films obtained using the different solvents using cross-polarized microscopy and differential scanning calorimetry (DSC). Figure 4.11 shows the photographs obtained for different samples using the various solvents. As cross-polarized microscopy generates contrast from the rotation of the polarized light passing through the sample, the crystalline domains in the photographs turn out to be light-blue highlighted. From Figure 4.11, we observe that all the drop casted films show higher crystallinity compared to the spin-coated films. This is because of the substantially higher thickness of the drop casted (>100µm) films compared against the spin-coated films (1µm). Further, drop cast film of PVDF from MEK and THF show a more even distribution off the crystalline domains, compared to DMF. Films made from DMF showed crystalline regions near the periphery off the grain boundaries (one such

boundary is shown in Figure 4.11). Furthermore, spin coated films from DMF did yield a continuous membrane. The crystalline structures were located near the high stress regions, however (as visible for spin coat image from DMF in Figure 4.11).

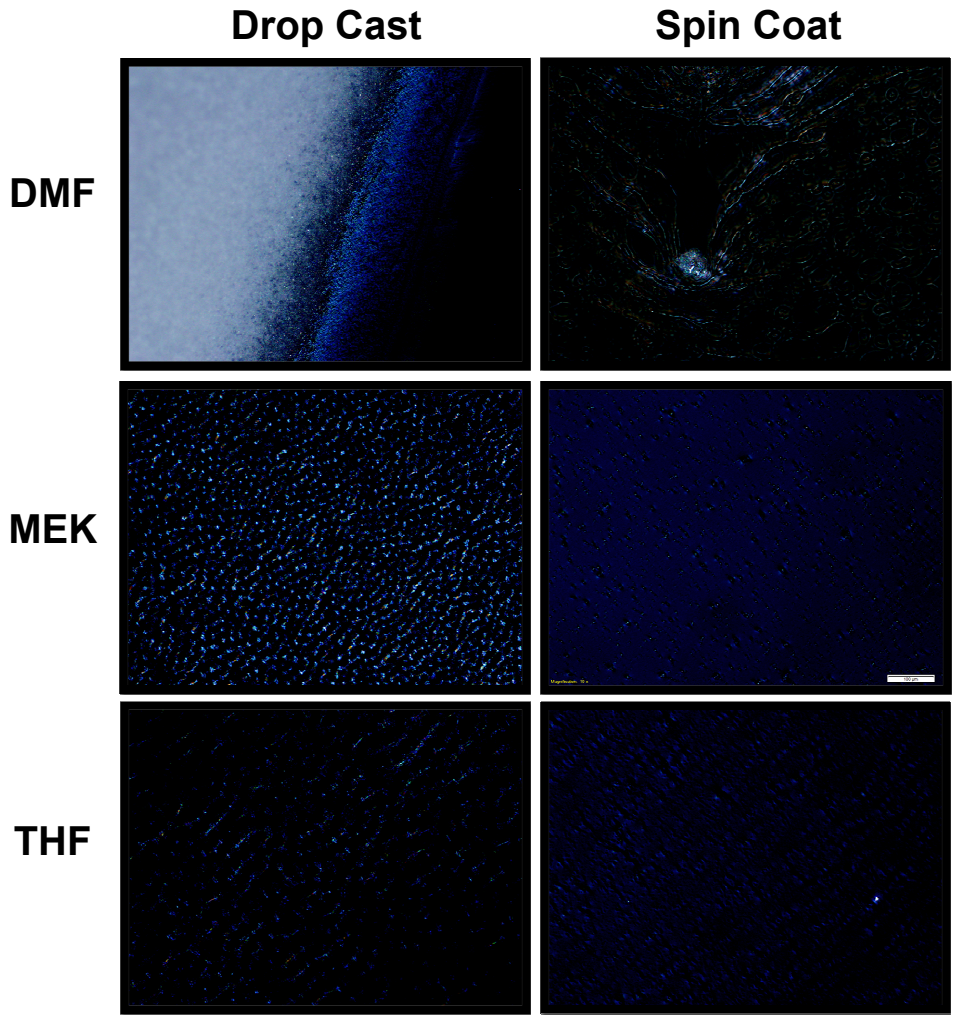

Figure 4.11 Comparison of cross-polarized optical microscopy images of PVDF films drop casted and spin coated using different solvents.

A comparison on the other hand, the spin coated films using MEK and THF result in less crystalline, yet well distributed, films compared to the drop casted films. Amongst MEK and THF, PVDF films spin coated from MEK resulted in higher crystalline domains compared to the films spin coated from THF. This might be due to the higher dipole moment of MEK (2.76D) compared to that of THF (1.63D) [*SI Chemical Data Book* (4th ed.), *Gordon Aylward* and *Tristan Findlay*, Jacaranda Wiley], even though their boiling points are nearly the same.

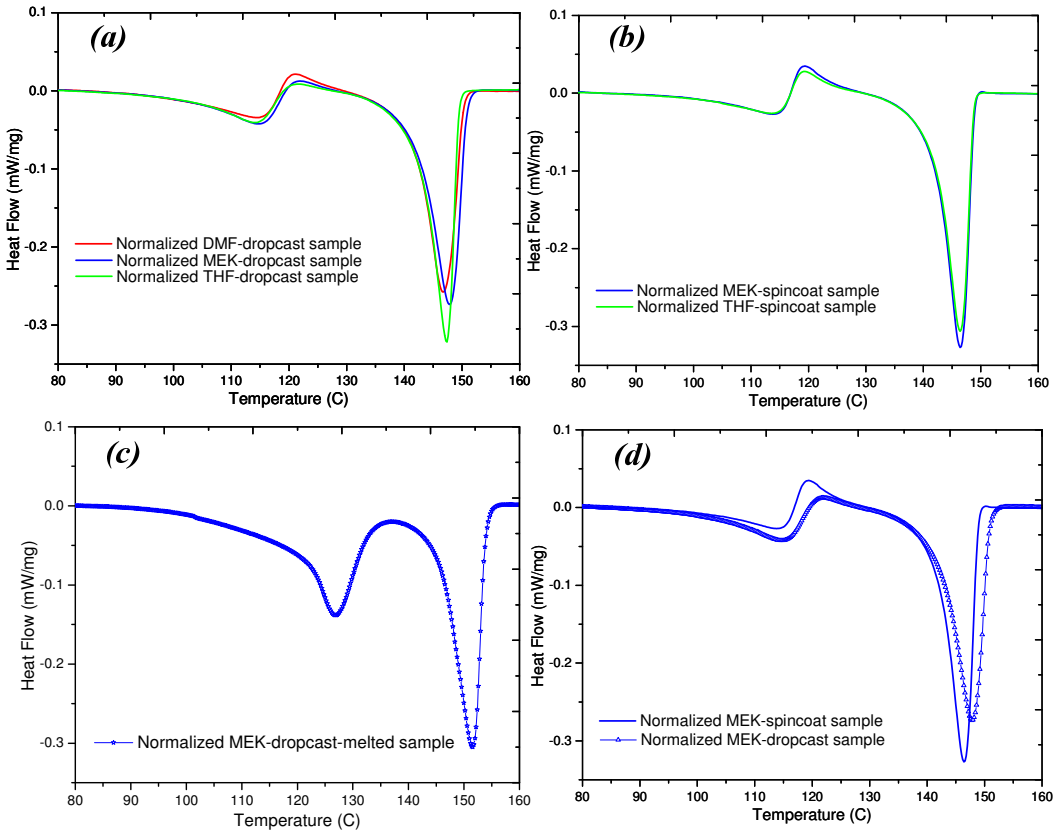

Figure 4.12 Weight normalized DSC curves for: (a) dropcast samples using different solvents, (b) spincoat samples using different solvents, (c) recrystallized drop cast sample from MEK, and (d) comparison of dropcast and spin coat samples from MEK

Differential scanning calorimetry (DSC) provides a detailed analysis in to the overall crystallinity of these samples. Figure 4.12a compares the weight normalized DSC curves obtained from the dropcast samples using different solvents. From Figure 4.12a, we infer that both DMF and MEK result in similar crystalline samples. However, THF gives slightly higher crystalline drop cast films. This does not hold true, however, in the case of spin coated samples, where both MEK and THF result in similar cyrstallinity being observed (Figure 4.12b). In order to confirm the piezoelectricity for drop cast samples, we melted the drop cast film fabricated from MEK and performed DSC of the recrystallized sample. Figure 4.12c shows the loss in the polarization of the recrystallized films. Comparison of spin coated versus dropcast samples shows us a significant increase in the crystallinity of a spin coated sample compared to drop casted (Figure 4.12d), defined by sharper peak and larger surface area under the curve.

Summarizing the data obtained using FTIR, cross-polarized microscopy and DSC for effect of different solvents on the structure of PVDF films, we found that MEK is capable of resulting in higher crystalline spin-coated films. Further, due to its ease of use, we used MEK in most of our present study.

4.4.4 Poling

Even though addition of TrFE to PVDF as a co-polymer forces the crystallization of PVDF primarily into beta phase, it is not necessary that all the dipoles in the PVDF-TrFE film will be aligned parallel to each other. Poling is a process that involves

exposure of the material to high electrical field gradients along with temperature, to force the re-orientation of molecular dipoles (Figure 4.13).

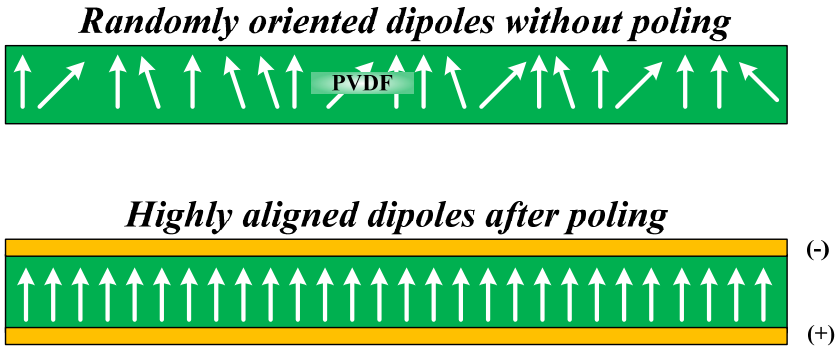

Figure 4.13 Schematic showing possible arrangement of dipoles before and after poling

Literature suggests subjecting the material to voltage gradients of as high as 120MV/m and at temperatures of 60-110ºC for poling the films [refs]. However, if extremely high voltage gradients can be achieved (100-800MV/m); flash poling at room temperature can also result in dipole reorientation [64, 95].

Figure 4.14 shows the schematic of the custom built poling setup. 3D rapid prototyping was employed to fabricate the desired structure. Steel disks (20mm diameter; 1mm thickness) were connected to external wires and used as electrodes.

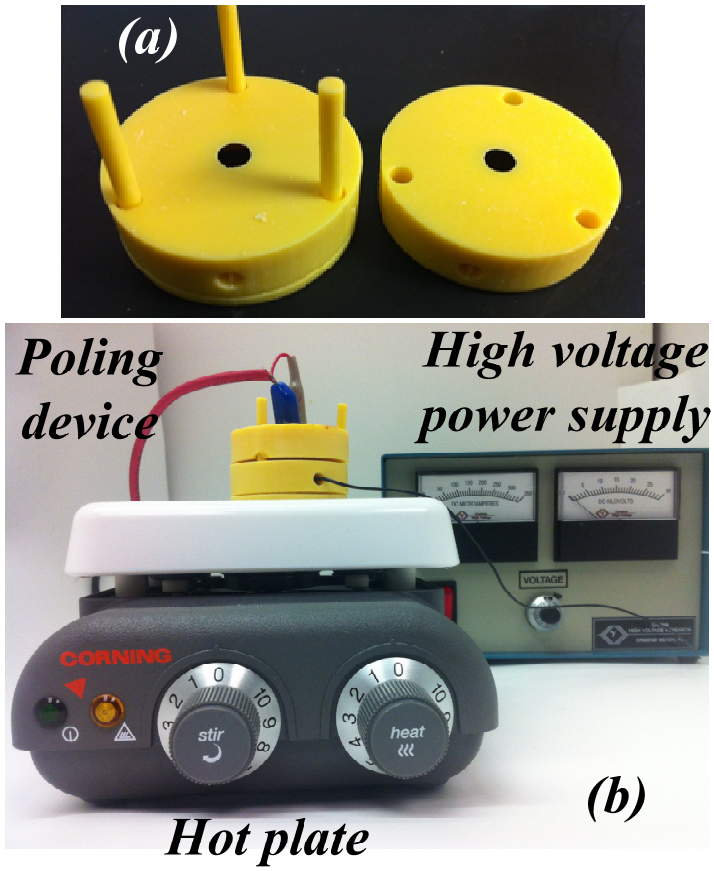

Figure 4.14 Photograph showing (a) poling chamber without steel electrodes, (b) complete poling setup

PVDF thin film sample was sandwiched between the steel disks and poled at 3kV, 90ºC for 0.5h. The whole setup was placed on a hot plate for the heating. After 0.5h, the hot plate was switched off, still keeping the high voltage power supply on, till the sample cooled down to room temperature. The poled samples were then analyzed using FTIR spectroscopy. For comparison, we also analyzed commercial PVDF (20µm) and PVDF-TrFE (9µm) films using FTIR spectroscopy (Figure 4.15a). Figure 4.15b shows the FTIR spectrum obtained from spin coated PVDF (MEK as the solvent) sample (in black) and

annealed, but not poled sample (in red). Clearly, the plot shows no enhancement or change in the crystalline structure of PVDF.

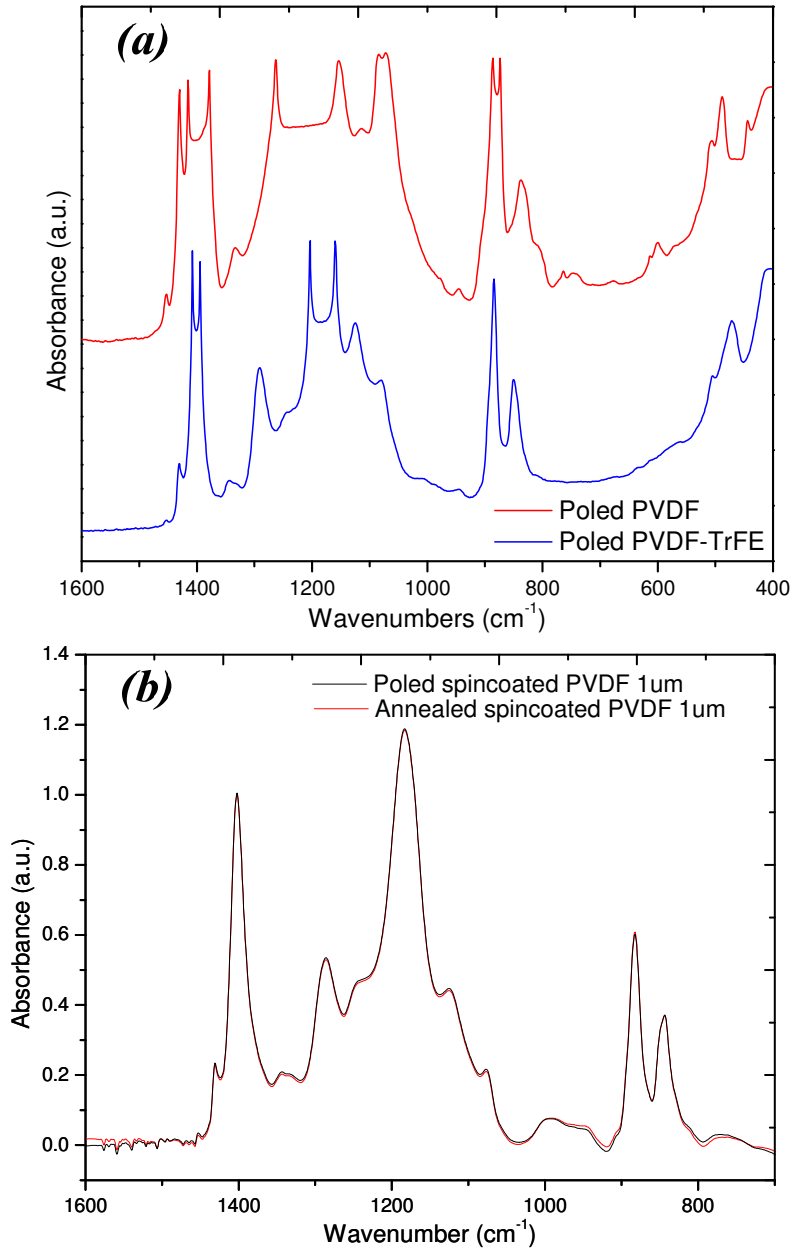

Figure 4.15 (a) FTIR plots for commercially obtained poled films of PVDF (only) and PVDF-TrFE (in transmission mode); and (b) Plot comparing FTIR spectrum (in transmission mode) of Poled and annealed PVDF films

In order to cross verify that there was no change in the permanent polarization of the film due to poling, we also measured the film capacitance using an LCR meter (B&K Precision Corp.) Electrodes were deposited on either side of the thin film (see Chapter 5) to be able to make electrical connectivity to external probes. The results obtained from poling have been summarized in Table 4.1. From the information, there was insignificant increase in the capacitance of the films on poling.

Table 4.1 Change in PVDF film capacitance due to poling. All the values were averaged and within 1% deviation from the mean

	Capacitance before poling (pF)	Capacitance after poling (pF)
Device 1	0.54	0.59
Device 2	1.23	1.31
Device 3	0.91	0.92

Therefore, impact of poling towards increasing the piezoelectricity in spin-coated thin film structures was negligible. This might be due to the fact that we used PVDF-TrFE in the present case, unlike PVDF as previously reported [76, 77, 98]. Further, spin-coating of the solution might result in the desired state of highest crystallinity possible from the thin films. It is also possible to bring about poling in the devices while performing electrical hysteresis experiments at voltages close to the electrical breakdown of the PVDF films. Further, electrical hysteresis also provides for an alternative method to measure the film crystallinity.

For electrical hysteresis, similar thin film (1µm) coated with electrodes on either side was used in the testing setup (Chapter 3) and the voltage across the electrode was swept between -200V to +200V. The charge generated (polarization) for different voltage sweep cycles are plotted in Figure 4.16.

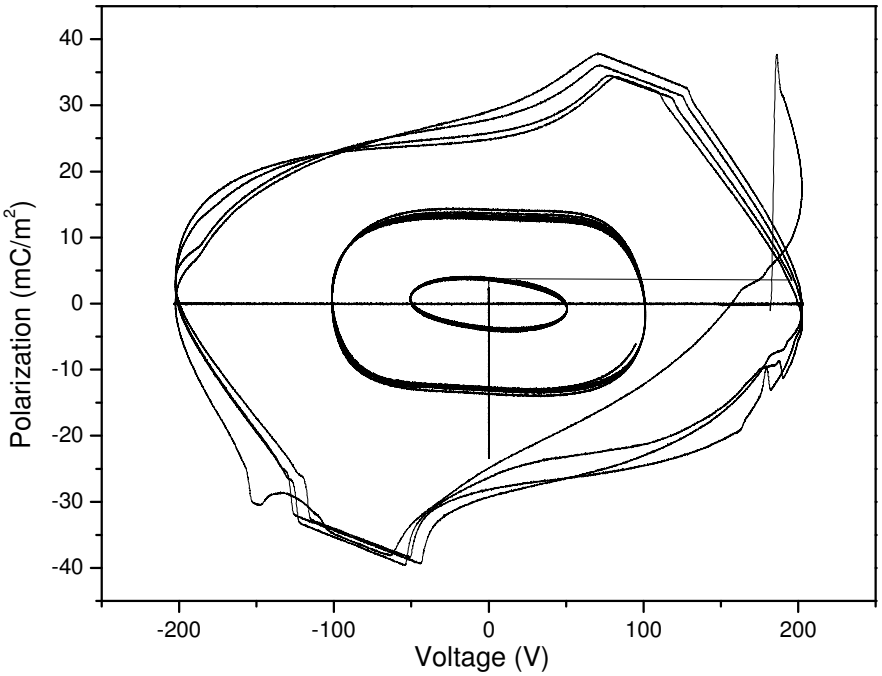

Figure 4.16 Plot showing three different electrical hysteresis experiments (loops) performed on 1µm PVDF film with peak voltages of 50V, 100V and 200V. Electrical breakdown of the PVDF films was observed at voltages higher than 200V

From the electrical hysteresis plots, we can easily determine the total remanent polarization of the PVDF film through the value of the y-intercept when the voltage across the film is zero. In the present case, the value of y-intercept and therefore of the

remanent polarization, P_r = 30 mC/m^2. Since the net polarization if the film were 100% beta crystalline film would be 165mC/m^2, [ref] the total crystallinity of spin-coated PVDF films can be calculated using:

$$\Sigma = k.Pr$$

Where, Σ = crystallinity and k = proportionality constant

Using the above, we find out the spin-coated films were 24% crystalline. Further, we showed above that the spin-coated, annealed films were showed predominantly beta phase structure only. Therefore, the spin coated films were showed ~25% beta phase crystalline domains, which is comparable to the 30% crystallinity observed from commercial films [115].

4.5 ELECTROSPINNING OF PVDF-TRFE NANOFIBERS

Electrospinning is the most popular way to produce ultrathin polymeric nanofibers. Electrospun fibers and their corresponding mats also have their own unique properties, such as average fiber diameters in the submicrometer range, high porosities, large surface areas, fully interconnected pore structures, tunable surface chemistry and sufficient mechanical strengths. These outstanding properties make electrospun fibers attractive for a wide range of applications, including dressing for wounds, tissue engineering, filteration, textiles, sensor and electronics applications [71, 116-118].

Electrospinning is a process through which nanofibers are produced under the influence of an electric field. The process involves subjecting a polymer solution held at the needle tip by its surface tension, to an electric field. The high electric fields involved in electrospinning results in substantial charge accumulation to be able to overcome the surface tension. As the intensity of the electric field increases, the solution at the tip of the needle elongates to result in to a conical shape known as the Taylor cone [119-122]. When the electric field reaches a critical value at which the repulsive electric force overcomes the surface tension force, resulting in a jet of solution that gets deposited on the ground collector plate.

In the electrospinning of polymer solutions, a number of parameters are known to affect the physical properties of the fibers, including the fiber shape, diameter, surface morphology, and porosity [71].

There have been few previous studies on the electrospinning of PVDF into nanofibers [71, 114, 123]. The high electric fields involved in electrospinning result in simultaneous pulling and poling of the fibers, resulting in fibers with dipole moments oriented along the length of the fibers. Further, it has been previously shown that the higher strain gradients and higher electromechanical coupling coefficients associated with nanofibers can result in significantly higher signal output compared to PVDF thin films [71]. Wang *et. al.* [124] fabricated a hybrid nanogenerator where they electrospun PVDF nanofibers between two collector plates to generated aligned nanofibers for sensing. Taking it a step further, Lin *et al* [71, 94] showed highly controlled patterning of PVDF nanofibers using near-field electro spinning for energy generation application. However, there have been no studies on the use of high-density highly aligned nanofibers

for sensing application. In order to create highly sensitive and robust pressure sensors, we fabricated highly aligned nanofibers in the present study.

4.5.1 Setup

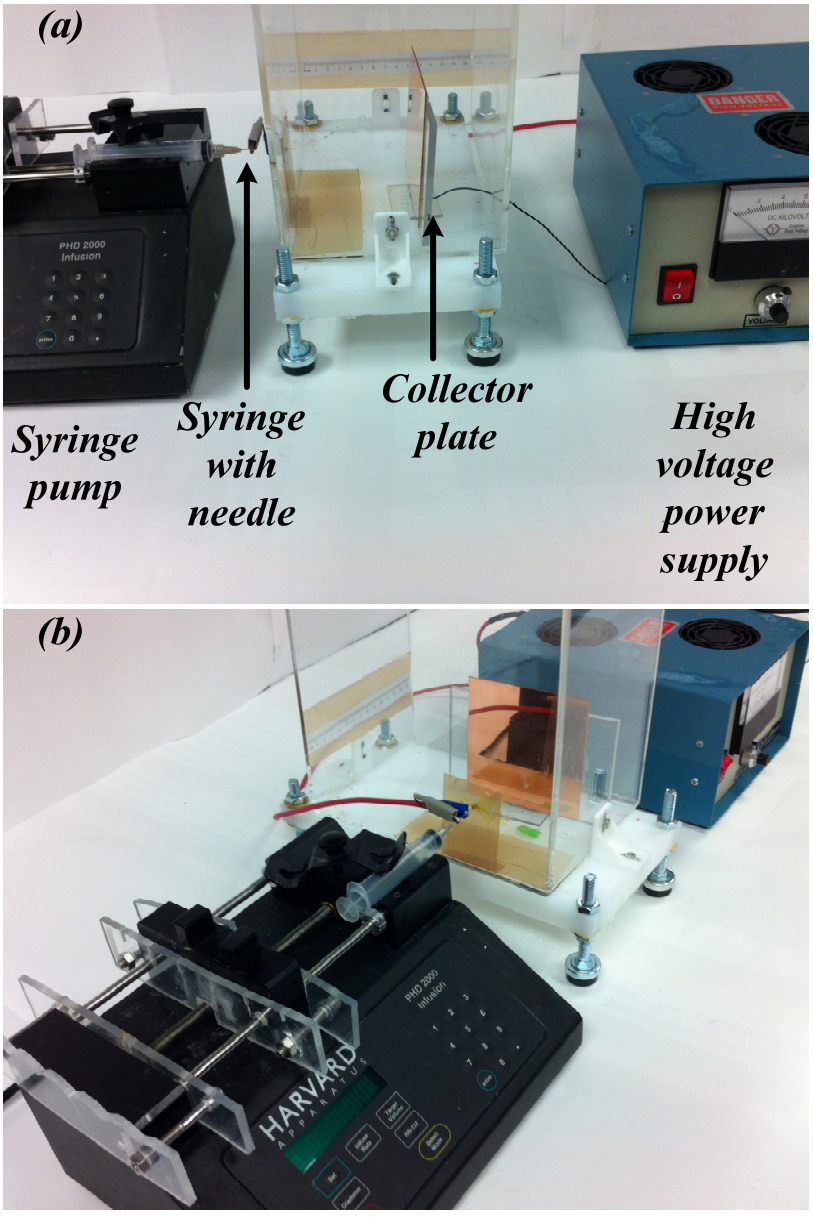

Figure 4.17 Photograph showing a conventional electrospinning setup: (a) front-view, and (b) side-view

Electrospinning setup typically consists of a solution-filled syringe on a syringe pump whose needle is connected to external high voltage (Figure 4.17). Across the tip of the needle, a collector plate or electrode is placed at a certain distance, which is connected to the ground of the external high voltage supply. Figure 4.17 shows the actual setup used for electrospinning of fibers in the present study with a copper plate (ground collector) placed 7cms away from the needle tip inside an acrylic box. The acrylic box is used to prevent electrostatic charging of the surroundings.

4.5.2 Parameter optimization

There are multiple variables in an electrospinning setup that need to be optimized in order to fabricate uniform fibers. Some of these include:

4.5.2.1 Concentration of PVDF

The concentration of the polymer is directly proportional to the viscosity of the solution. Viscosity of the polymer solutions is important in determining the solution flow rate and adjusting the surface tension of the solution for electropinning. From Figure 4.18, we notice that the polymer concentration has a significant impact on the morphology and the diameter of the fibers obtained. Using 12% (w/v) of PVDF solution yields in beaded fibers. As we decrease the concentration of PVDF, the bead count was found to increase. Using 14%-18% (w/v) of PVDF solution showed to electrospin the desirable diameter and morphology of the fibers.

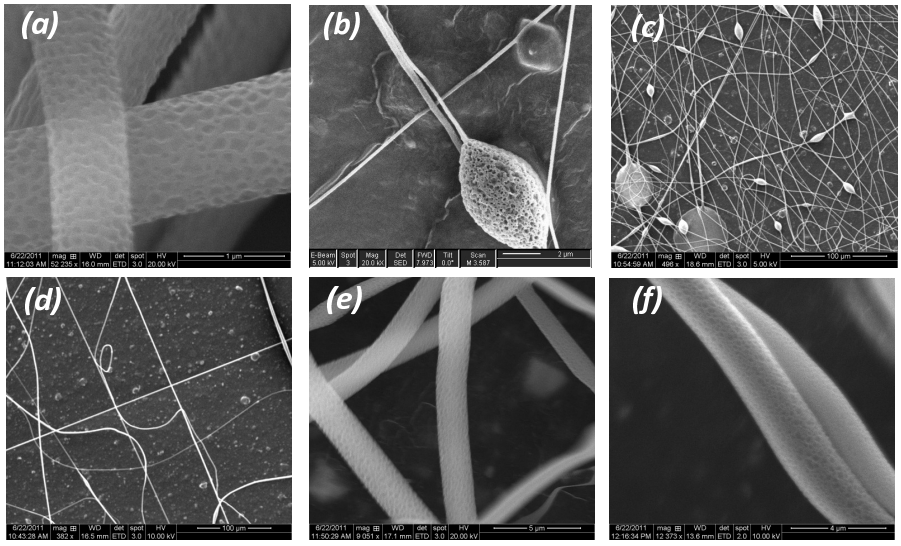

Figure 4.18 SEM images of electrospun fibers for different PVDF concentrations in MEK, alongwith their average diameters: (a) 8%: 500 nm, (b) 12%: 450 nm, (c) 14%: 1.07 µm, (d) 16%: 1.6 µm, (e) 18%: 1.9 µm (f) 20% (w/v): 2.0 µm

4.5.2.2 Choice of solvent

The nature of the solvent used can have a significant impact on the fibers that are electrospun. Solvent not only acts as a carrier for the polymer molecules to the needle tip, but is also responsible for the polymerization into fibers from the jet stream. Therefore, the solvent needs to be volatile enough for successful fabrication of fibers. Lack of solvent evaporation, before the jet stream hits the collector plate, can result in formation of nanoribbons or flatter fibers. Conventionally, use of MEK, THF, DMF, chloroform and DMAc has been preferred as electrospinning solvents [71, 72]. In the present study, we have used MEK and DMF as the solvents for our electrospinning purposes. MEK, being highly volatile in nature, is a good solvent of choice for short-distance electrospinning. Whereas, the low volatility of DMF can be compensated with higher

electrode-collector separation, allowing for DMF in the jet stream to evaporate before fiber formation.

4.5.2.3 Solution flow rate

The solution flow rate, coupled along with the fiber formation velocity, determines the amount of solution that accumulates in the Taylor's cone. Higher flow rates could lead to substantial accumulation, followed by solvent evaporation and eventually blocking of the needle outlet. Low flow rates, on the other hand, can lead to discontinuities in the electrospinning process, which can be a serious concern for core-shell fibers (introduced later in this chapter). Further, low flow rates can result in extremely thin nanofibers [125].

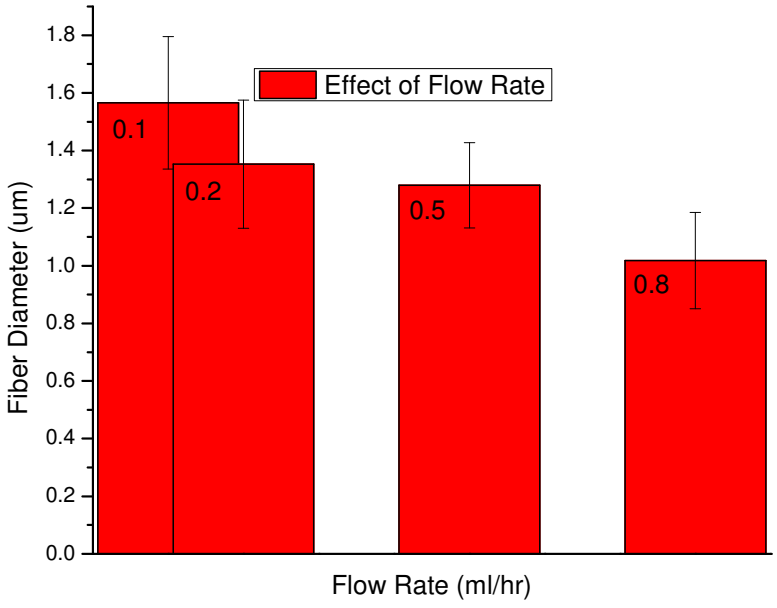

Figure 4.19 Plot showing the variation of electrospun fiber diameter as a function of flow rate for 12% PVDF/MEK solution

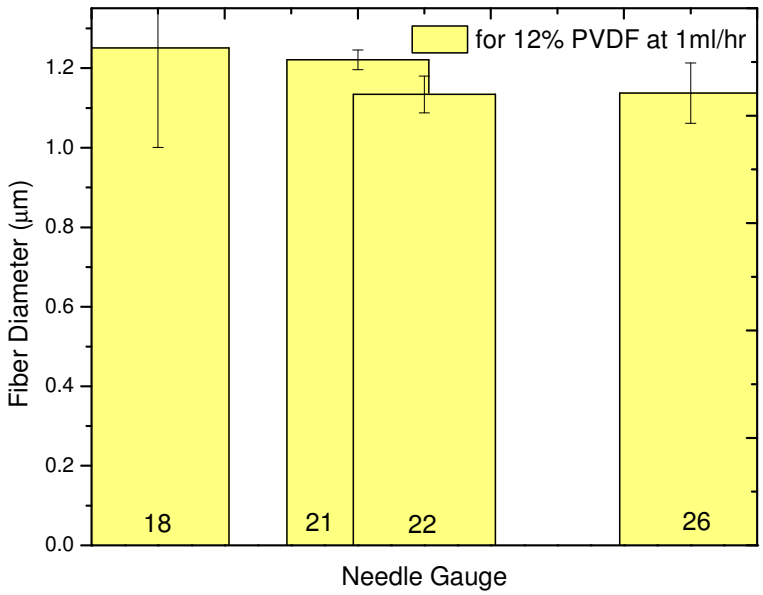

Figure 4.20 Plot showing the variation of the fiber diameter as a function of the needle diameter (gauge) for 0.3ml/h flow rate on the syringe pump

The flow rate is easily controlled from the syringe pump. Figure 4.19 shows the fiber diameter decreased with an increase in the solution flow rate. However, the variation in fiber diameters were found to be insignificant. This leads us to conclude that there was negligible variation in the fiber diameter due to any change in the flow rate.

The diameter of the needle used for electrospinning can also affect the solution flow rate and therefore alter the fiber morphology or diameter. But we did not observe any significant difference in fiber diameter due to variation in needle gauge as well (Figure 4.20).

4.5.3 Ground collectors for highly aligned nanofibers

Conventionally, people have used a metallic plate or sheet connected to ground, as the collector plate. Grounded plates are convenient collectors for electrospinning of non-woven fiber mats. However, in order to deposit highly aligned nanofibers, the ground collector geometry needs to be altered. Change in ground geometry helps re-orient the fiber patterning with the help of altered electric field.

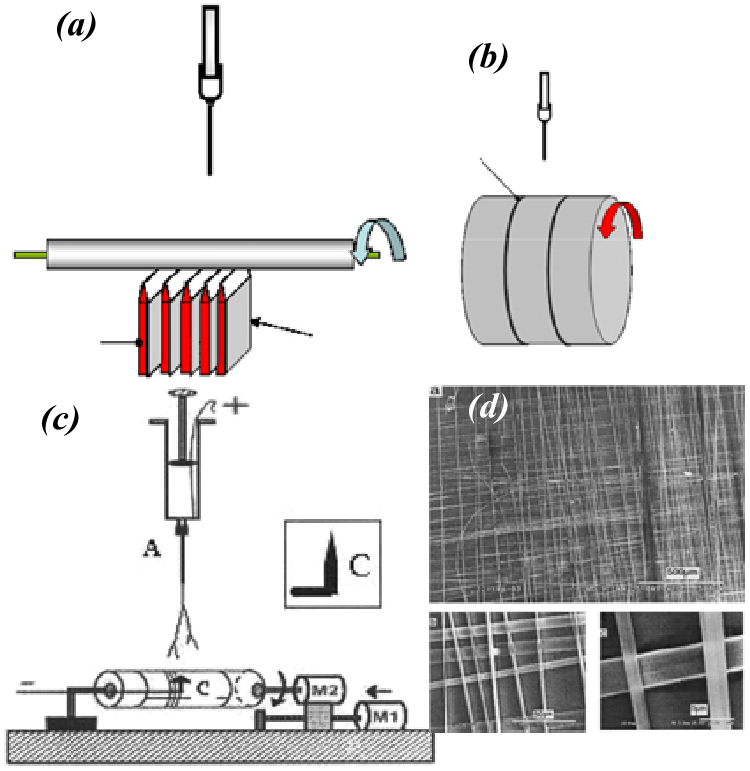

Figure 4.21 Schematics of ground collectors for electrospinning of highly aligned nanofibers: (a) knife blades, (b) parallel wires, (c) pointed needle; and (d) SEM images of patterned nanofibers. Sources: [126, 127]

In order to pattern highly aligned nanofibers, people have used rotating drum assembly, knife blades, near field, needle tip as ground collectors previously. Figure 4.21 shows some of the ground collectors that have been reported previously.

Albeit these setup did yield in aligned nanofibers, it was difficult to fabricate high density of highly aligned nanofiber mats. In the present study, we describe the setup of mesh electrodes and rotation drum assembly collector electrodes to achieve high density highly aligned nanofiber mats and also study the factors that affect the fabrication of such fiber mats.

4.5.4 Mesh electrodes

Mesh type electrodes are an extension of the parallel type electrodes used previously for fabrication of electrospun nanofibers (Figure 4.21b). Figure 4.22 shows a photograph of the mesh type electrode used in the present study. The mesh used in the present case was a stainless steel 316 mesh (1x1cm^2, 2mm diameter wire, McMaster Carr), fixed on to a polypropylene substrate. Ground wire was connected to the mesh electrode by soldering the terminal directly. For test samples of the electrospun fiber mat, kapton (polyimide, McMaster Carr) film was placed on top the mesh electrodes and detached upon completion of the elctrospinning process.

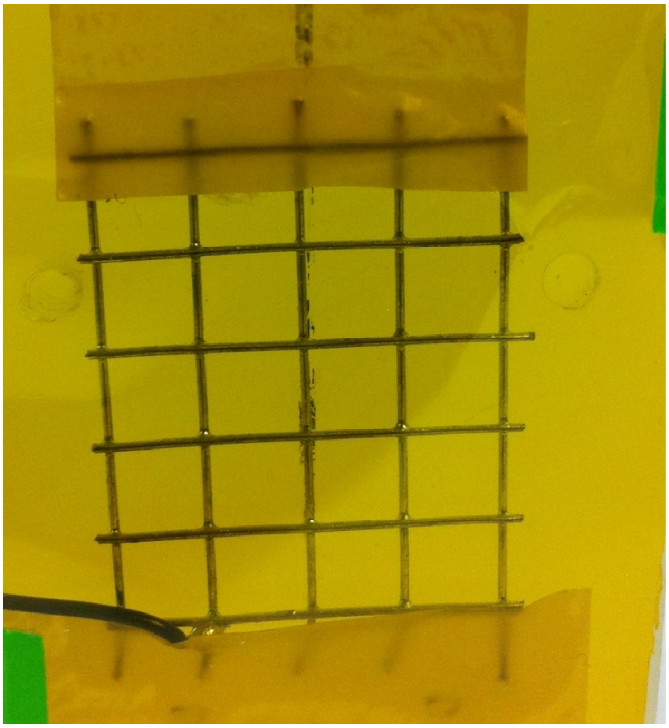

Figure 4.22 Photograph of a stainless steel based mesh ground collector for electrospinning of aligned nanofibers

4.5.5 Rotating drum electrodes

Most of the studies on aligned nanofibers have reported the use of a rotating drum so far [73, 122, 128]. Conventionally, the entire rotating drum would be grounded and the nanofibers would be deposited on the drum in an aligned fashion because of the high rotating speeds of the drum. In the present study, we initially started with such a rotating drum setup by grounding the entire rotating drum. However, lack of capability to fabricate high density of aligned nanofibers led up to optimize the rotating drum geometry.

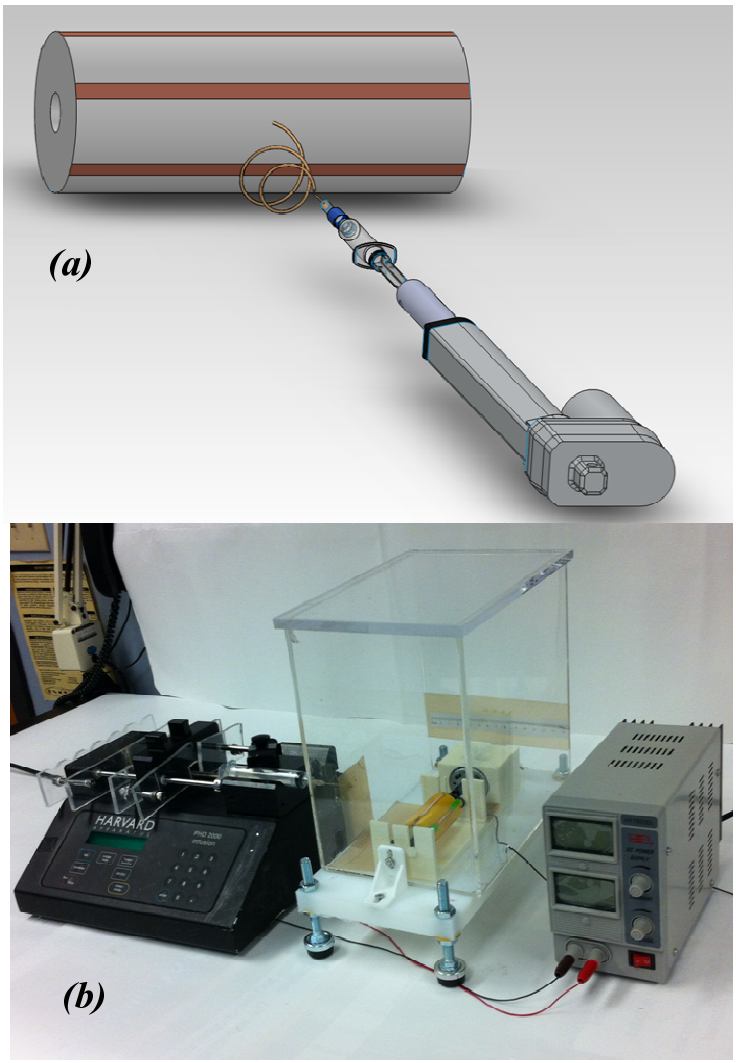

Figure 4.23 (a) Schematic of the Rotating drum setup with parallel ground copper wires, and (b) photograph of the actual rotating drum setup

The present version of the rotating drum setup is shown in Figure 4.23. The drum itself is constructed out of an ABS-like plastic, using a laser sintering machine (Dr. Brijesh Gill, UT Houston). The diameter of the rotating drum is 1.2" (30.5mm) and the length of the drum was 3.5" (89mm). Grounded copper wires (3mm diameter) were connected to the ground wire, which was passed through the hollow shaft and connected

to external ground near the rotating motor holder. The entire assembly, comprising of motor holder and the rotating drum holder, was also fabricated using the same laser sintering machine. The DC motor powering the rotating drum was controlled through and external power supply and the rotational speeds could be controlled in the range of 0-4000rpm. Typically, a kapton film was rolled over the rotating drum assembly for the patterning of aligned nanofibers.

4.5.5.2 Highly aligned Nanofibers

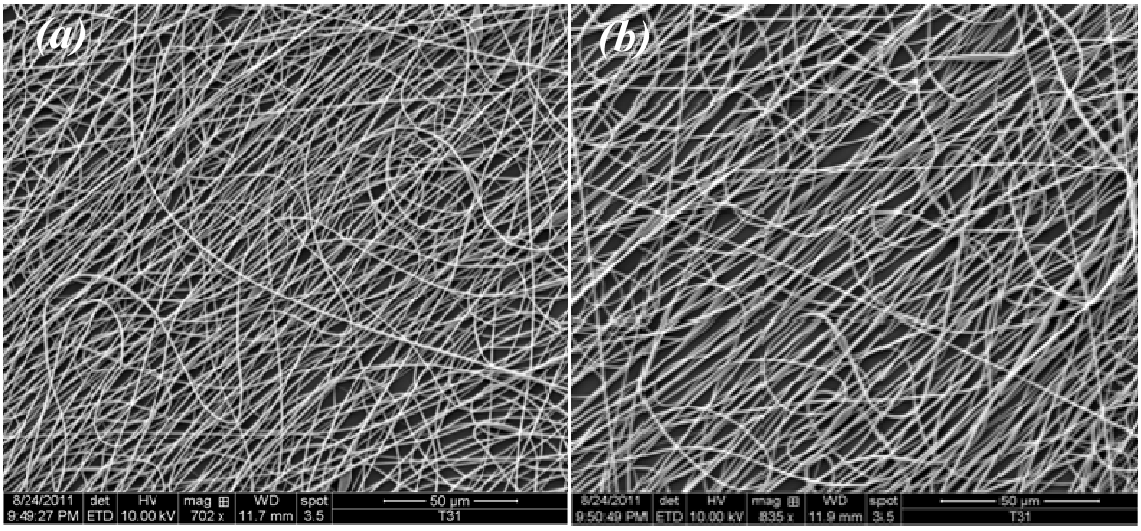

Figure 4.24 SEM images of aligned nanofibers electrospun using mesh electrodes

Figure 4.24 shows the aligned nanofibers patterned using mesh type electrodes. From the SEM images, we observe that even though there was a general orientation of the fibers, there a lot of fibers that were not aligned. The fibers were electrospun from at 14% (w/v) PVDF solution in MEK, with flow rate of 0.5ml/h and 1kV/cm (8cms

spacing) voltage gradient. The total duration of the electrospinning was 20mins. The average fiber diameters were found to be 1.45 ± 0.18µm.

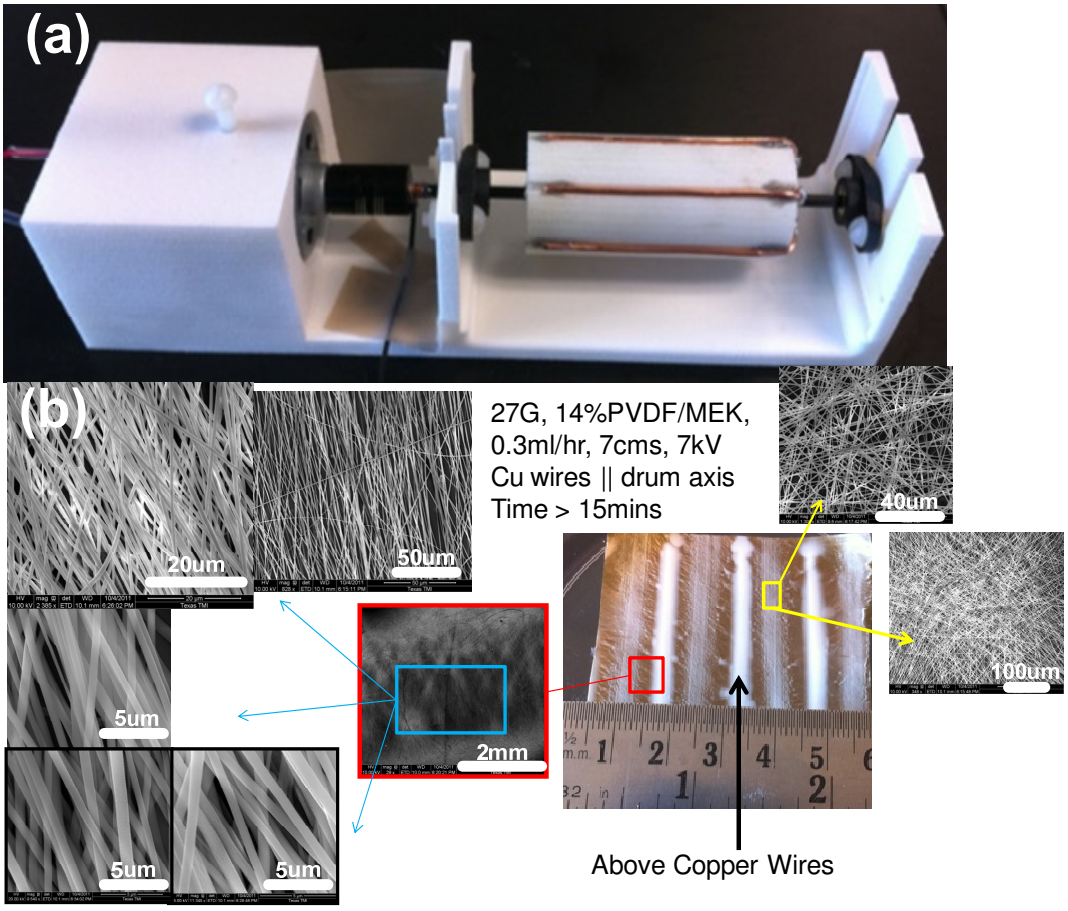

Figure 4.25 (a) Photograph showing the rotating drum assembly with DC motor coupled to the shaft of the drum; (b) Photograph and SEM images showing the various parts of the depostied fibers from rotating drum setup and nature of aligment in these fibers

When similar experiments were done using a rotating drum assembly, better alignment of the fibers was obtained. Figure 4.25 shows the rotating drum setup in the

holder along with the images of the nanofibers fabricated. The electrospinning conditions for patterning highly aligned nanofibers is also described in Figure 4.25.

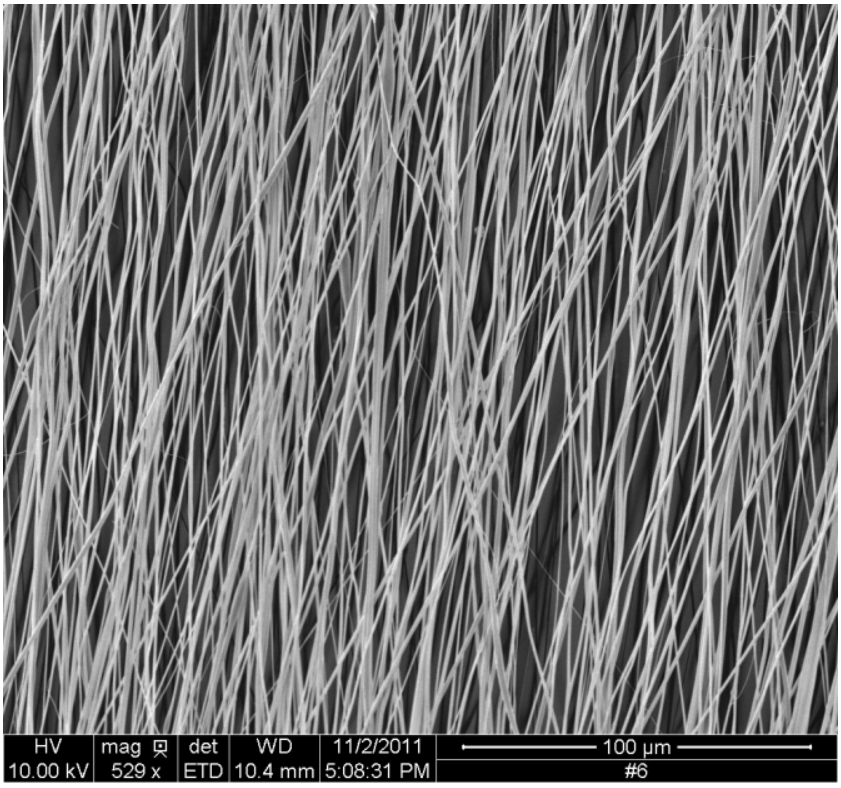

Figure 4.26 SEM image of a high-density highly aligned fiber sample fabricated using the rotating drum setup for 45mins.

It was generally found that the highly aligned nanofibers stretch in the area between the two ground copper wires. While, when the portion of the substrate directly above the copper wires was found to have random orientation of nanofibers (Figure 4.25b). Similar effect has also been reported before [117]. The average fiber diameter

fabricated was found to 737 ± 75nm for this experiment, which was carried out for 20mins only.

In another experiment, which was carried on for a longer period of time (45mins), we found that the present rotating drum setup is capable of patterning high-density of highly aligned nanofibers. Figure 4.26 shows a SEM image of the sample.

The average fiber diameter in this case was found to be 963 ± 86nm in diameter. In general, we found the rotating drum assembly works better compared to the mesh type electrodes for patterning of high-density highly aligned nanofibers.

For a better comparison methodology, we quantified the fiber alignment based on the protocol described in [129]. Since the described protocol was for quantification of fiber alignment from optical microscopy images, we altered the protocol to account for the differences in the illumination in SEM images. The modified protocol is shown in Figure 4.27. In order to process the images using this protocol, we used ImageJ (NIH) along with the Oval profile intensity plugin. In the present study, we did not rotate the FFT (fast fourier transform) image by 90º to account for the shift in angle. The oval profile plugin allows us to plot the total sum of the gray pixel intensities along the blue line (Figure 4.27) for a sweeping angle of 0-360º.

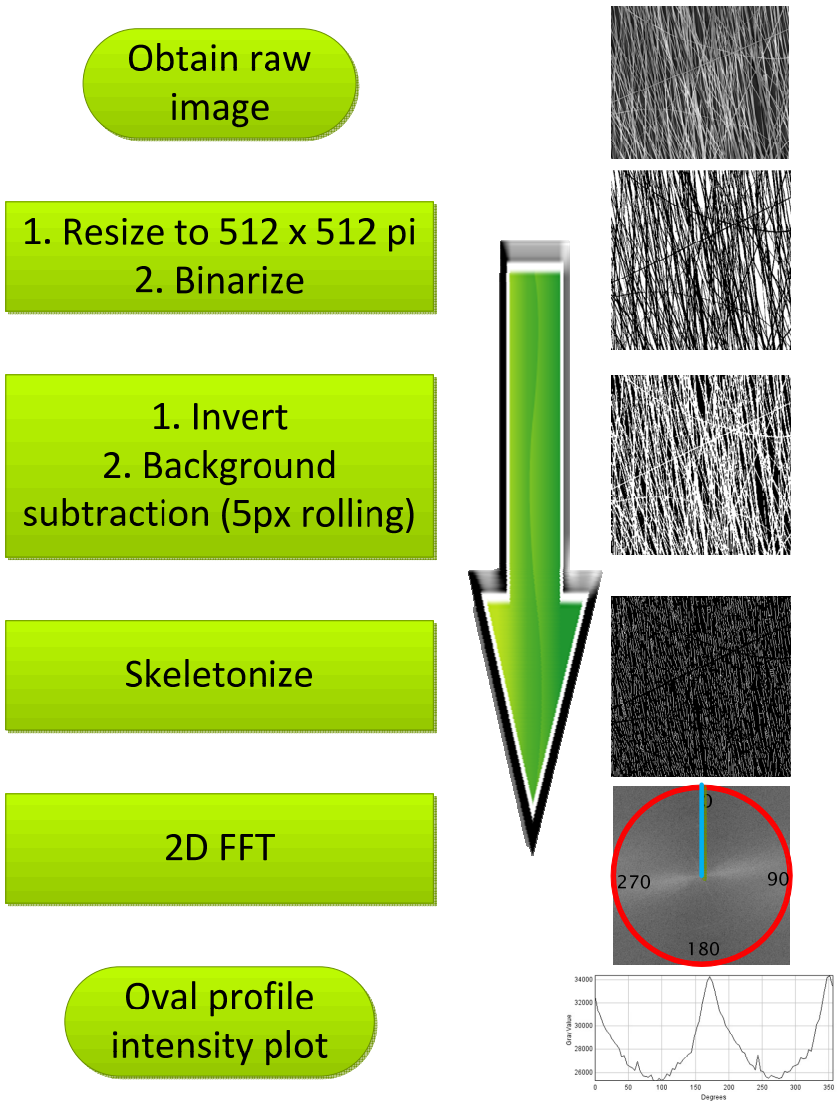

Figure 4.27 Schematic showing the flowchart for quantification of fiber alignment alongside the output obtained for individual step for a SEM image

Using the above technique, we studied the effect of fiber alignment due to variation in rotating drum speeds. Figure 4.28 shows the SEM images obtained from different parts of the rotating drum for varying speeds of the drum. All the electrospinning experiments were carried out for 20mins using 14% (w/v) PVDF solution

in MEK. From Figure 4.28, we find that as the rotating drum speed is increased, the density of fibers that are aligned increases correspondingly. Whereas the density of the fibers deposited directly above the ground copper wires (random oriented fibers) decreases for increasing rotating drum speeds. Each SEM figure was processed as per the method described in Figure 4.27 and the corresponding 2D FFT images obtained for each SEM image has been presented in Figure 4.28.

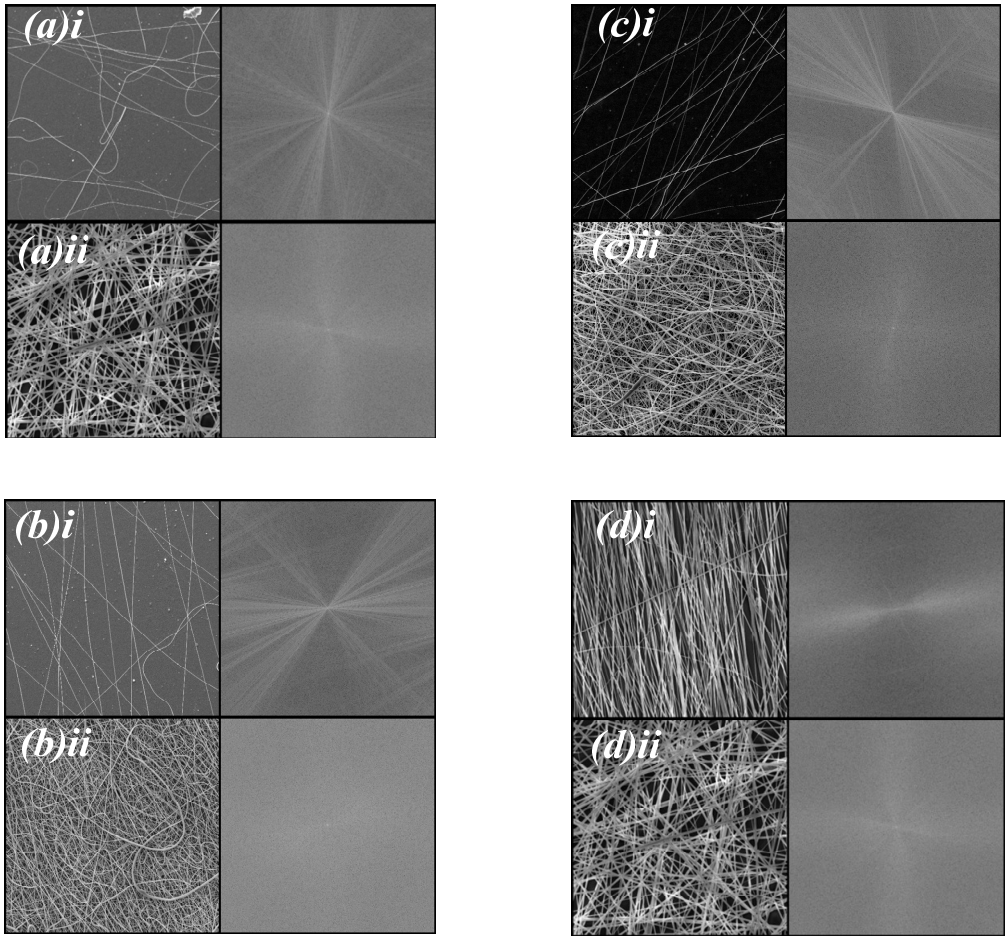

Figure 4.28 SEM images alongside the corresponding 2D FFT figures for different speeds of the rotating drum: (a) 3.3rpm (717 ± 44nm), (b) 245rpm (608 ± 90nm), (c) 487rpm (586 ±65nm), (d) 3500rpm (737 ± 75nm). Figures corresponding to 'i' refer to the aligned fibers portion of the substrate, whereas the 'ii' refers to the random oriented fibers portion of the substrate

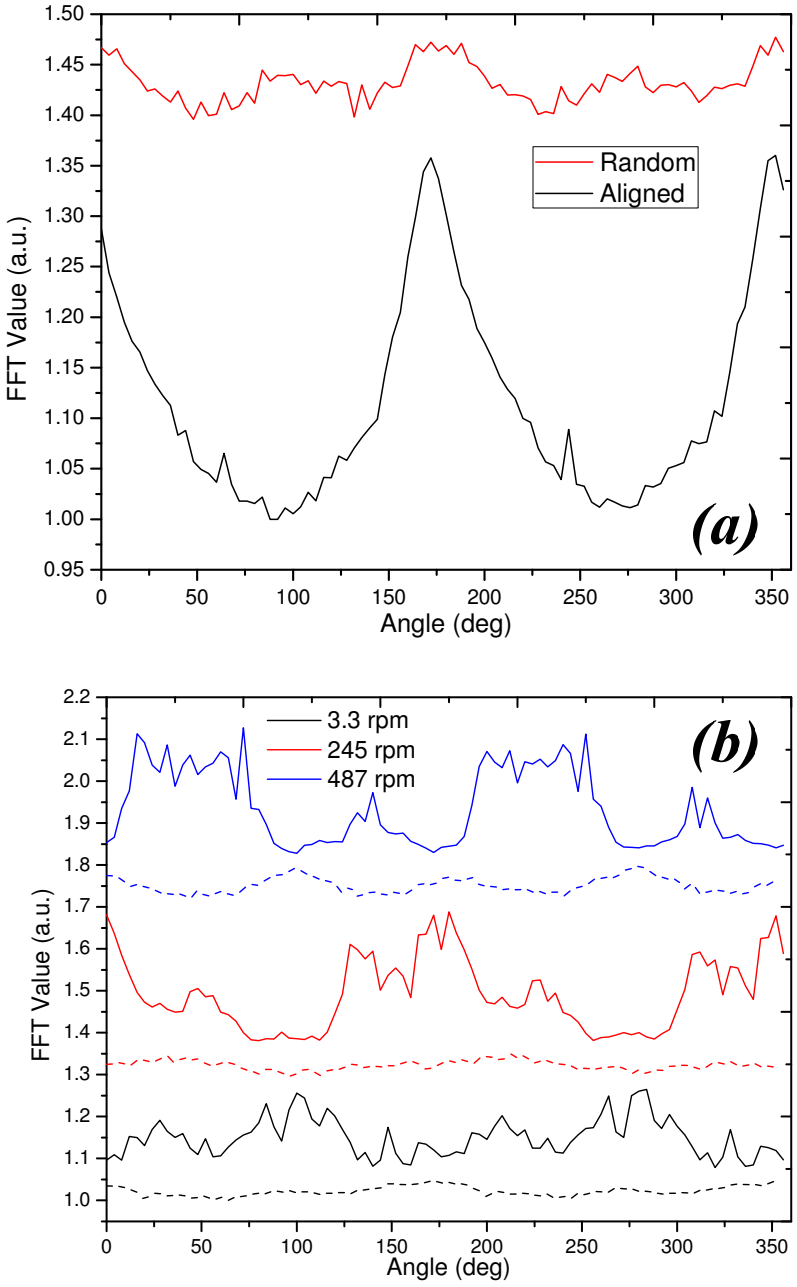

Figure 4.29 Plots of oval profile intensity for (a) aligned and random portion of fibers at 3500rpm, (b) aligned (solid) and random (dash) portion of fibers at different speeds of rotating drum

Results of using oval intensity plot on the 2D FFT images have been summarized in Figure 4.29. Figure 4.29 compares the FFT value (grey pixel intensity summation) as a function of the angle sweep. All the curves were normalized as per the lowest FFT value in the intensity plot. The individual plots were shifted for ease of comparison.

From Figure 4.29a, we notice that aligned fiber intensity plots has two peaks in a 0-360º intensity plot. Presence of two peaks, separated by an angle of 180º indicates aligned fibers, represented by the periodicity in the 2D FFT plots.

On the other hand, randomly oriented nanofibers are expected to show four peaks over the same range of 0-360º intensity plot [129]. From Figure Figure 4.29a, we clearly see this trend. Further, the presence of two dominant peaks is a good indication of presence of aligned nanofibers obtained from high rotating drum speeds. Furthermore, it was found that the amplitude of the intensities of randomly oriented nanofibers was much lower compared to those of aligned nanofibers. This difference in the amplitude could be easily used as key parameter to distinguish between aligned and randomly oriented nanofibers. On similar lines, Figure 4.29b shows that as the rotating drum speed is increased, the fibers tend to align better, indicated by the diminishing amplitude of the peaks and emerging prominence of two peaks at higher rotation speeds. However, the randomly oriented nanofibers (dash curves in Figure 4.29b) do not show appreciable change in fiber alignment.

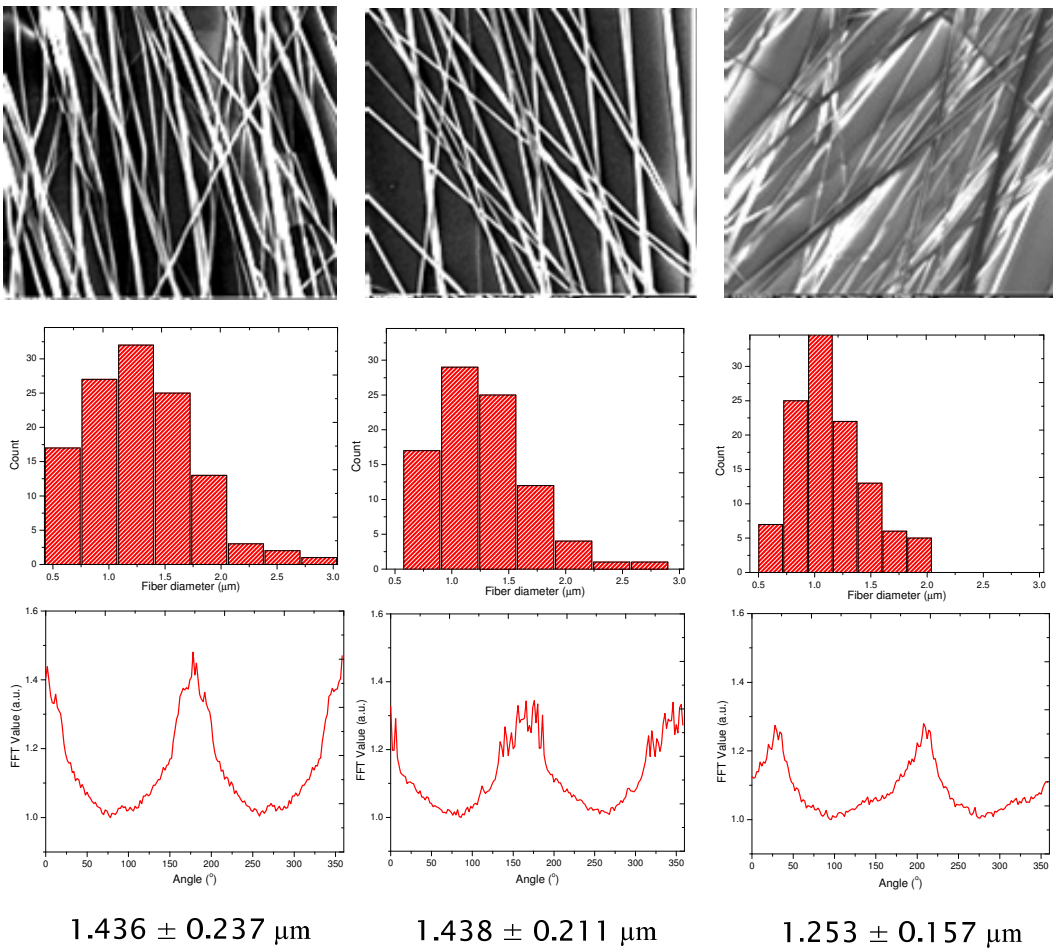

Figure 4.30 Figure showing the SEM images, fiber diameter distribution, FFT value of fiber alignment and the average fiber diameters for three different highly aligned electrospun fiber samples

In order to find out the variability between different samples of highly aligned electropsun fibers, three different electrospinning samples were analyzed for fiber alignment and diameter distribution. All the variables, including electrospinning time, voltage gradient, drum rotation speed, were maintained constant. Figure 4.30 summarizes the fiber distribution over the three different samples fabricated. We observe similar fiber diameters and fiber count distribution for two of the three different samples electrospun.

The third sample also showed good alignment of the fibers and a sharper distribution of fiber diameters (average fiber diameter of 1.253 ± 0.157μm) compared to the other two samples. From the present study, we conclude that similar patterning of fibers is possible over large number of samples by keeping the electropsinning variables constant.

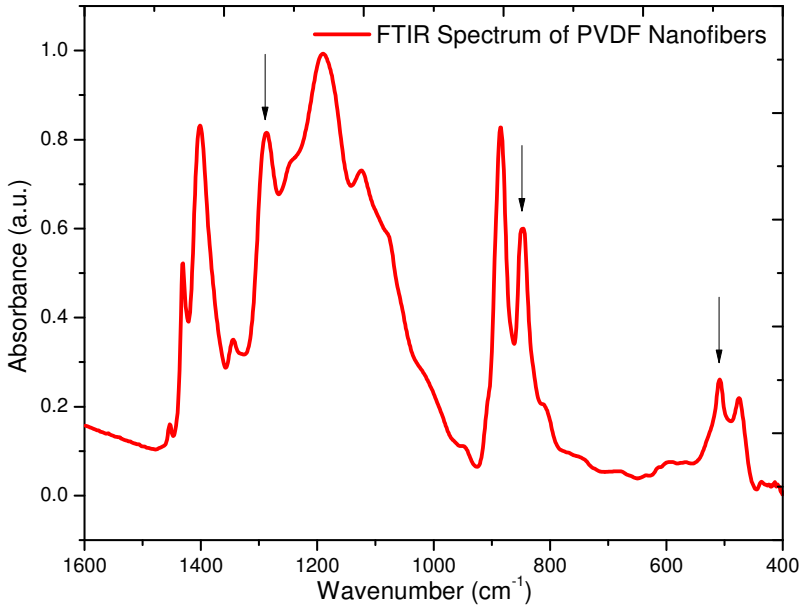

Figure 4.31 FTIR plot of randomly oriented nanofibers on a copper coated substrate. Arrows indicate peaks corresponding to beta crystalline phase

In order to study the effect of electrospinning on the structure of PVDF fibers, we studied the fibers using FTIR and DSC. Figure 4.31 shows the FTIR spectrum obtained from electrospun fibers on a 4" silicon wafer coated with copper. The FTIR spectrum was obtained for eight different spots on the wafer in grazing angle incidence mode and then averaged to obtain the curve shown in Figure 4.31. A quick comparison of the FTIR

spectrum of electrospun fibers with Figure 4.8 curves indicates the presence of high beta crystal phase in nanofibers. Further, from the peak intensities obtained, it was found the fibers deposited at the center of the substrate were richer in beta phase content, compared to fibers deposited towards the edges of the substrate.

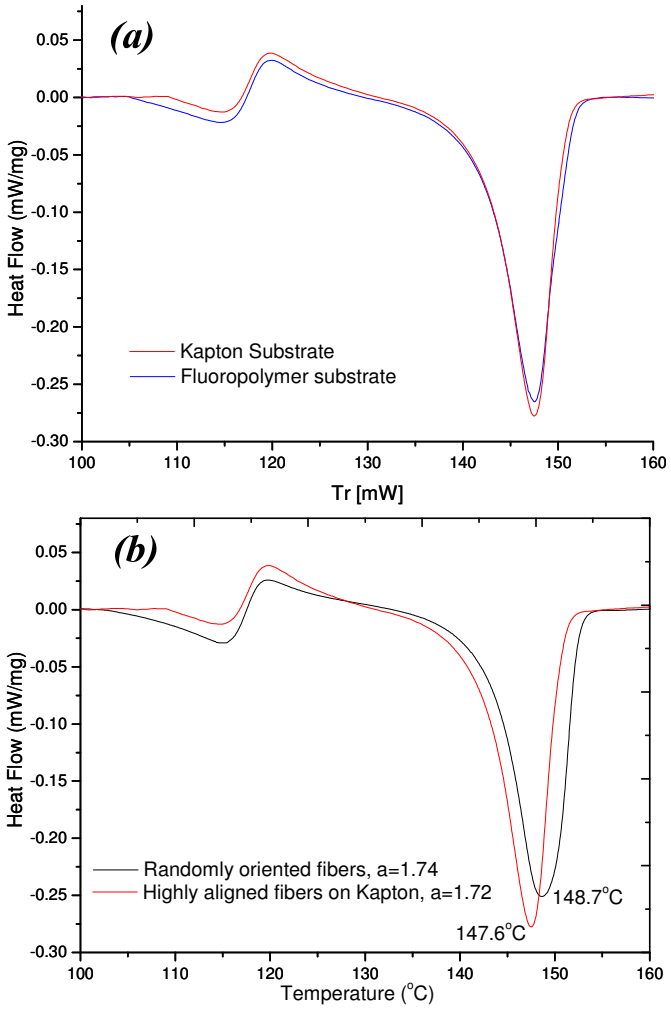

Figure 4.32 Weight normalized DSC curves for: (a) aligned nanofibers patterned on Kapton substrate and fluoropolymer substrate, and (b) random patterned nanofibers and highly aligned nanofibers

Figure 4.32 shows the DSC curves obtained for nanofiber samples. Highly aligned nanofibers (14% w/v PVDF/MEK) were patterned on fluoropolymer substrate (ACLAR, Electron microscopy sciences) as detachment of fibers was much more easier compared to fibers electrospun on kapton film. However, both the substrates gave similar results for cyrstallinity of the fibers. From Figure 4.32b, we infer that the aligned nanofibers show slightly higher cyrstallinity compared to randomly oriented nanofibers. However, the increase in crystallinity was insignificant.

In summary, we found developed high speed rotating drum for patterning high-density highly aligned nanofibers. Further, we quantified the alignment of the fibers using 2D FFT plots of the SEM images and observed that higher rotation speeds allow us to pattern highly aligned nanofibers. We also demonstrated the ability to fabricate highly aligned nanofibers with cyrstallinity similar to those of thin films. Even though the crystallinity of the nanofibers might be similar, nanofibers can be expected to significantly boost the device sensitivity by virtue of higher flexibility and lower material consumption.

4.5.5.3 Core-shell nanofibers

In the present study, we fabricated core-shell nanofibers with the purpose of making pressure sensors. Therefore, as described earlier, it was important to fabricate a conductive core, which could act as one of the electrode. Further, in order to electrospin core-shell nanofibers, the solution dispensing mechanism had to be altered slightly, such that it allowed concomitant flow to two solutions with the shell solution encapsulating the

core solution. Figure 4.33 shows the schematic of the modified setup and a photograph of the actual setup.

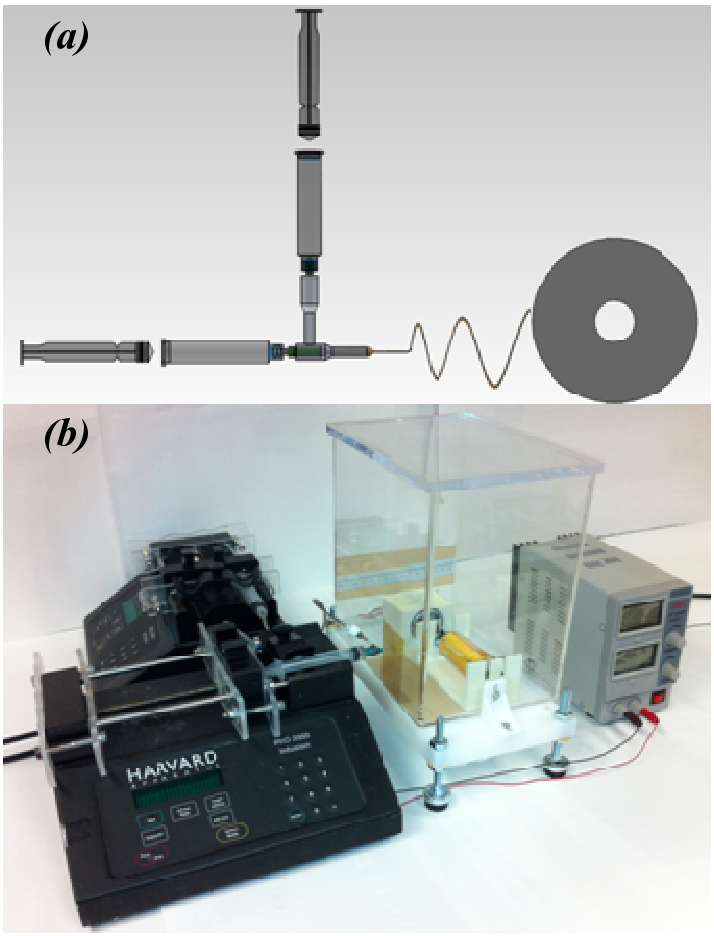

Figure 4.33 (a) Schematic of the Core-shell electrospinning setup along with the rotating drum (front view) and (b) photograph of the actual setup

For core-shell electrospinning, we optimized the needle-in-needle design such that the inner needle is perfectly aligned, concentric to the outer needle. Further, the whole two-needle assembly needs to be air-tight, in order to avoid and leakages and

solidification of the solution due to solvent evaporation. It was found that keeping the tip of the inner needle slightly protruding from the tip of the outer needle helps in the electrospinning of core-shell structures. Since the two solutions used for core-shell electrospinning are composed of different materials having different viscosities, different syringe pumps were used to balance the flow rates of the two solutions.

Initially to avoid the mixing of the two solutions, we used a water soluble polymer, PEO (polyethylene oxide), as the core material and PVDF in MEK as the shell material (Table 4.5). However, very few core-shell fibers were observed along with difficulties electrospinning of water based solvent, due to low volatility and electrostatic repulsion.

For ease of electrospinning, we shifted the core-solution from water based to organic solvent based. However, in order to successfully fabricate pressure sensors from core-shell nanofibers, it is necessary to have a conductive core that is capable of transferring the charge generated from PVDF-TrFE to the terminal conducting electrode. Based on previous literature suggesting the use of gold nanoparticles for fabrication of conductive nanofibers [130], we initially employed the use of silver nanoparticles (20-40nm, Alfa Aesar) mixed with PMMA (poly(methyl methacrylate), 15% w/v) in DMF as the solvent. The electrospinning conditions and results have been summarized in Table 4.5 for the various polymers and compositions used.

In order to measure the resistance of the core-material that was used to fabricate core-shell structure, we employed the testing setup as shown in Figure 4.34. Two silver wires (1.5mm diameter, alfa aesar) were wrapped around a glass slide, separated by a gap

of 1cm. This glass slide was pressed against the testing sample on another glass slide. The two silver wires were then connected to an external digital multimeter to measure the sample resistance.

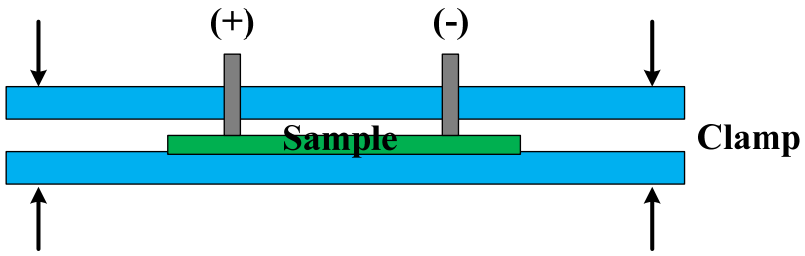

Figure 4.34 (a) Schematic of the resistance testing setup, and (b) photograph of the actual setup

Table 4.2 Summary of the resistance values of the different materials used as conductive core material for core-shell electrospinning

Solution Sample	Resistance (k ohms)
10% Ag NPs + 15% PMMA/DMF	$> 10^3$
10% Ag NPs + 15% PMMA/Chloroform	$> 10^3$
14% PVDF-TrFE/2mg Graphene/DMF	$> 10^3$
PANI/CSA/m- Cresol/ PMMA/ chloroform/ unfiltered	100
1.4% PANI/m-Cresol /PMMA/filtered	71
1.4% PANI/m-Cresol/PMMA/un-filtered	10
PANI/Sulfonic Acid + 5% PMMA	2.4
10% PANI + 15% PMMA/Chloroform	.49
PANI/CSA/m-Cresol/Chloroform/filtered	156
PANI/CSA/m-Cresol/PMMA/chloroform/filtered	220
PANI/ Sulfonic Acid/15% PMMA/ Chloroform	.7

Using the described testing setup, we measured the resistance of different materials. The resistance values along with the actual polymer tested have been summarized in Table 4.2. For the silver nanoparticles (Ag NPs), the resistance of the fibers was found to be very high, beyond the measurable limits of the digital multimeter. When EDS (energy dispersive x-ray spectroscopy) was done for these fibers, it was found that silver nanoparticles aggregated (Figure 4.35).

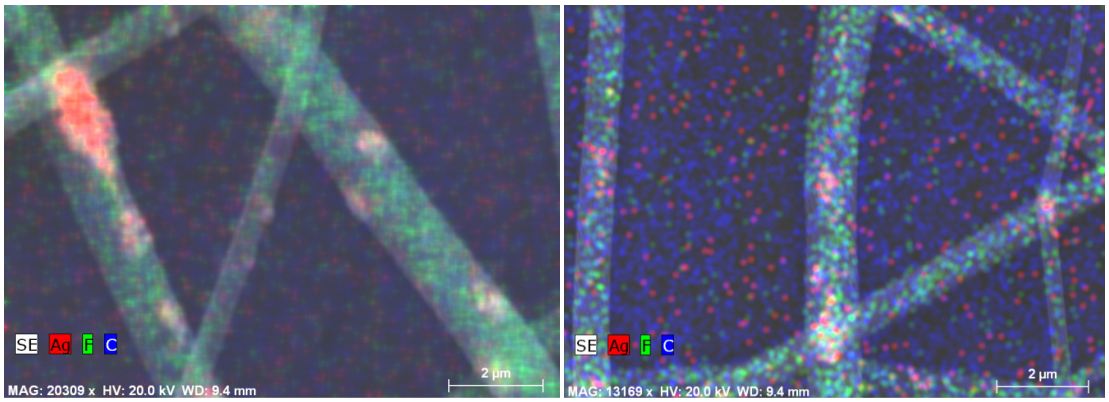

Figure 4.35 EDS images of PMMA loaded silver nanoparticles. The images show the aggregating of silver nanoparticles in fibers as the reason for high resistance of the fibers

Ultrasonication of silver nanoparticles for long hours also did not seem to create uniform suspension of silver nanoparticles. Further, addition of metallic nanoparticles in other studies as well did not reveal very high conductivities [130].

In place of metallic nanoparticles as additives conductive polymers offer a better alternative. Some of the common conducting polymers include PANI (polyaniline), PEDOT:PSS (poly(3,4-ethylenedioxythiophene) poly(styrenesulfonate)). PANI, by itself, is not very conductive and grainy, which can easily clog the electrospinning needle.

Filtered PANI, however, is not as conductive even when doped with CSA (10-camphorsulfonic acid) or prepared in m-cresol as the primary solvent Table 4.2.

However, the resistance of the material is also a function of the thickness. Therefore, in place of measuring the resistance, measurement of resistivity or conductivity is a better parameter for comparison. Table 4.3 summarizes the measure conductivity of the used conducting polymer compositions in the present thickness, using the same testing setup described in Figure 4.34.

Table 4.3 Summary of conductivity of some of the conductive polymers used in the present study

Material	Conductivity (S/cm)
1.4% PANI/CSA/m-cresol (unfiltered) + 15% PMMA/Chloroform	0.0606
1.4% PANI/CSA/m-cresol (filtered) + 15% PMMA/Chloroform	2.963
1.4% PANI/CSA/m-cresol (unfiltered)	851
2.6% PEDOT:PSS in water	684
2.6% PEDOT/water/PVP (dropcast)	60

From the table, we found that PEDOT:PSS in water gives similar conductivity, comparable to PANI doped with CSA in m-cresol solution (unfiltered). Further, PEDOT solution was not grainy like PANI, making it suitable for electrospinning. Table 4.5

summarizes the samples fabricated using PEDOT solution and the various electrospinning conditions used for the same.

For imaging of the core-shell fibers fabricated, we employed TEM imaging. However, TEM could not be relied for all prepared samples as some of the samples were thicker than 500nm. For fibers thicker than 1µm in diameter, confocal imaging of selectively dyed materials can help image core-shell fibers. Table 4.4 summarizes the characteristics of fluorescent dyes used in the present study.

Table 4.4 Excitation and emission wavelengths of the dyes used in the present study

Dye name	Excitation wavelength (nm)	Emission wavelength (nm)
Fluorescein	494	521
Rhodamine B	554	627
Rhodamine 110	498	520
1-Pyrenebutyric Acid	341	376
Fluram	390	475

Table 4.5 Electrospinning conditions and materials used for fabrication of Core-Shell electrospun fibers (CSEF) listed out in chronological sequence

Core	Shell	Electrospinning conditions and comments	Images	Core-shell?
PEO (1%) /Chloroform (0.3ml/h)	PVDF (14%) / MEK (0.15ml/h)	Horizontal setup on copper plate		Very few
PVDF (14%) + Fluorescein (1%) / MEK (0.8ml/h)	PVDF (20%) / MEK (0.5ml/h)	Horizontal setup on copper plate		Few
PVDF (20%) + Ag NPs (1%) / MEK (0.2ml/h)	PVDF (30%) / MEK (0.4ml/h)	Horizontal setup on copper plate		Yes

PMMA (13%) + Fluorescein (1%) / MEK (0.2ml/h)	PVDF (20%) / MEK (0.4ml/h)	Horizontal setup on copper plate, 7cms/9kV Fibers fused together	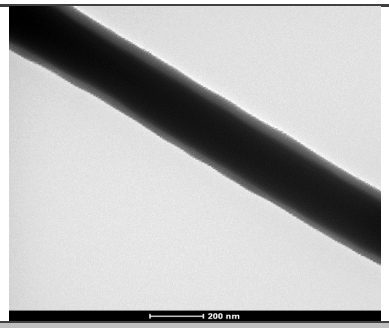	Yes
PMMA (13%) + Fluorescein (1%) / Chloroform	PVDF (25%) / MEK (0.8ml/h)	Horizontal setup on copper plate 16cms, 25kV, Long distance ES		Few
PMMA (13%) + Fluorescein (1%) / Chloroform	PVDF (20%) + Rhodamine B (1%) / DMF	Horizontal setup on copper plate 16cms, 15kV Mesh electrodes	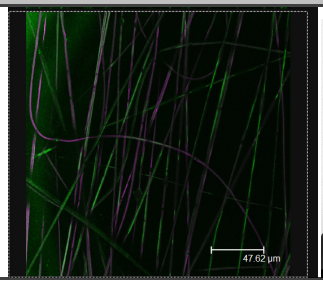 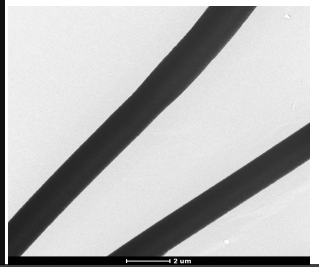	Few

PMMA (13%) + Fluorescein (0.5%) / Chloroform (0.55ml/h)	PVDF (18%) + Rhodamine (<0.1%) / DMF (0.8ml/h)	Horizontal setup on copper plate 16cms, 16kV, reduced dye conc = good TEM contrast	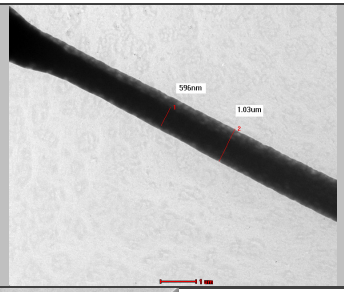	Yes
PVP (2.63g) + PEDOT (1.25g) / DMF (0.2ml/h)	PVDF (14%) / MEK / 1ml/h	Vertical setup on mesh electrodes, 7cms, 7kV, Great TEM contrast due to solvents	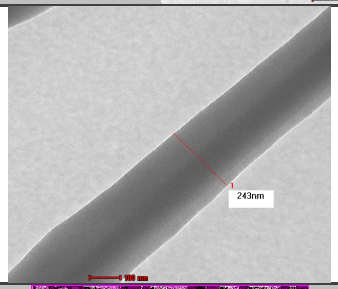	Yes
PVP (0.2g) + PEDOT (1.6g)/ DMF (1ml/hr)	PVDF (14%) + Rhodamine (0.1%) / DMF-MEK (25:75) (1.5ml/h)	Vertical setup on mesh electrodes, 14cms, 15kV	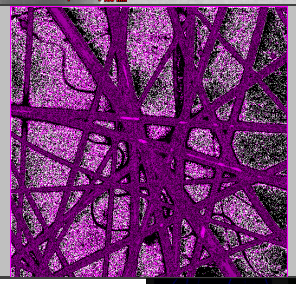	Undetermined
PVP (0.2g) + PEDOT (1.6g) + Rhodamine B (0.1%) / DMF (1ml/h)	PVDF (14%) + 1-pyrene butyric acid (0.2%) / DMF-MEK (25:75) (3ml/h)	Vertical setup on mesh electrodes, 12cms, 15kV, Uniform electric field	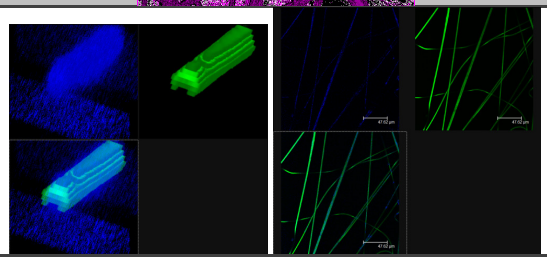	High percentage, easily imaged

From the spectra information, coupling an UV dye along with red dye would work best for imaging of core-shell materials. As Table 4.5 shows from the images obtained for different fluorescence dyes and different electrospinning conditions. Switching from the horizontal electrospinning to vertical setup aided in the ease of electrospinning and formation of a good Taylor's cone with the help of gravity. Increasing the electrospinning distance also helped in formation of thinner, complete fibers. Electrospinning at shorter distance (<10cms) did not allow all the solvent to evaporate and resulted in formation of flatter fibers. However, the Taylor's cone would solidify quickly, leading to discontinuous electrospinning of CSEF. Therefore, the shell solvent was changed from purely MEK based to a mixture of MEK and DMF (75:25 ratio). Addition of DMF to the solvent mixture increased the effective boiling point and allowed more time for the PVDF to remain in dissolved state. These series of optimizations enabled fabrication of core-shell fibers with good consistency and controlled patterning.

The best dye combination was observed with fluorescein and 1-pyrenebutyric acid or fluorescein and fluram. Fluram, being an expensive dye, fluorescein and 1-pyrenebutyric acid was used as an alternative for electrospinning or imaging of core-shell fibers. Figure 4.36 shows confocal laser fluorescence microscopy images of core-shell fibers electrospun directly on to a rotating drum assembly for patterning highly aligned core-shell fibers. From the images, we observe good percentage of core-shell fibers present, shown by simultaneous fluorescence of fluram and rhodamine B.

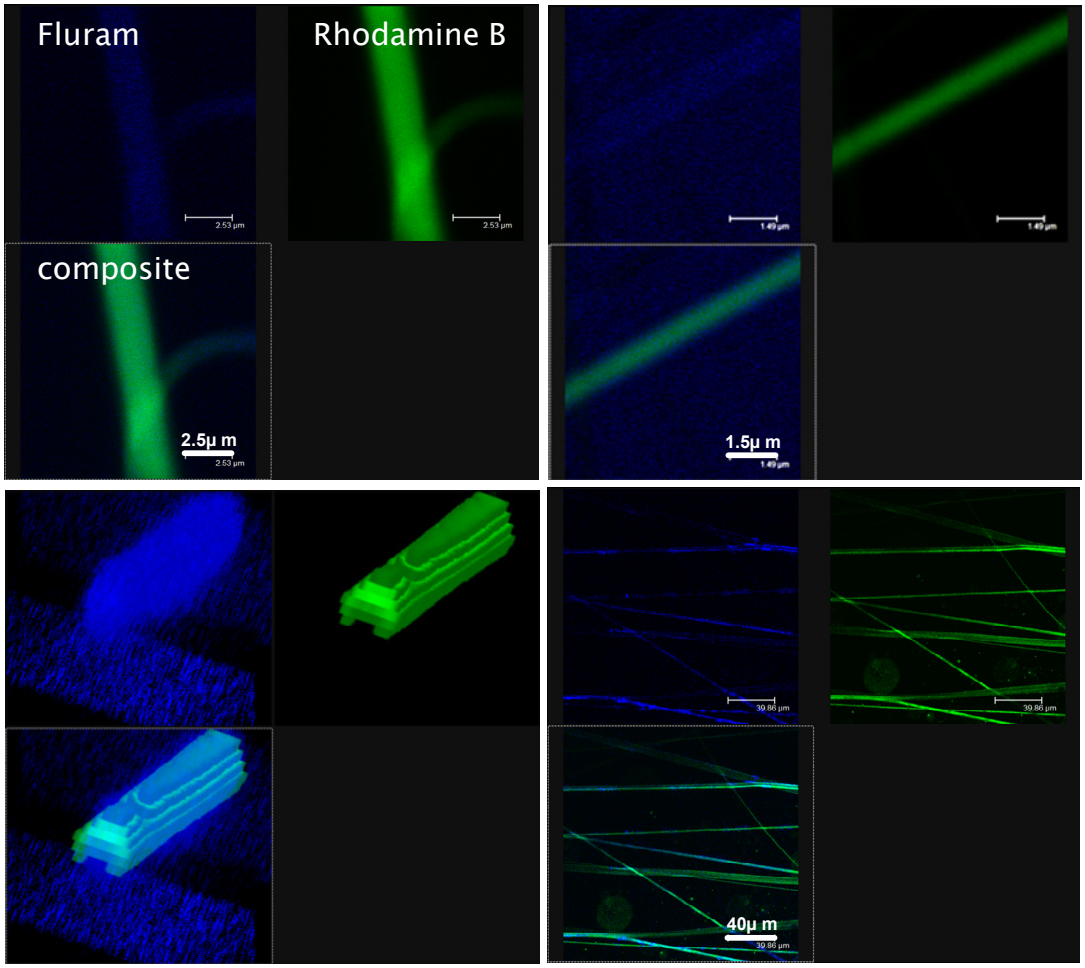

Figure 4.36 Confocal laser fluorescence microscopy images of core-shell electrospun fibers using Rhodamine B for the core (PEDOT) and Fluram for the shell (PVDF)

Presence of core-shell fibers was cross verified using transmission electron microscopy. Figure 4.37 shows the TEM images of all the core-shell fibers electrospun directly on the rotating drum setup. TEM imaging was highly suitable for imaging of core-shell fibers of couple hundred nanometers thickness. The darker core is visible in most of the fibers. The contrast between the core and shell gets lowered by the presence of fluorescent dye in the shell.

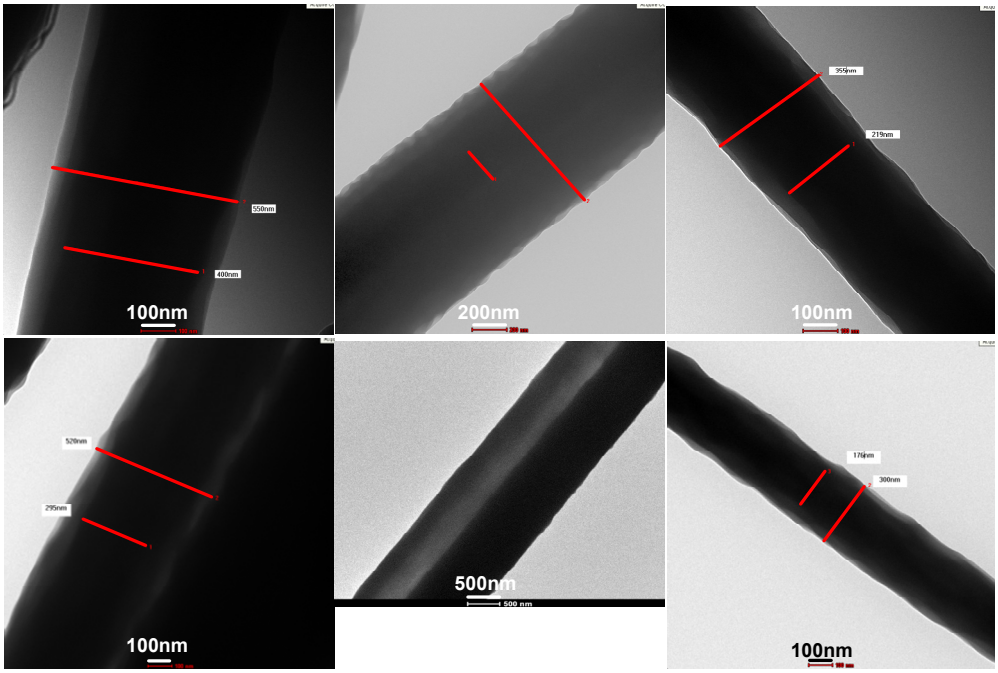

Figure 4.37 TEM images of fabricated core-shell electrospun fibers

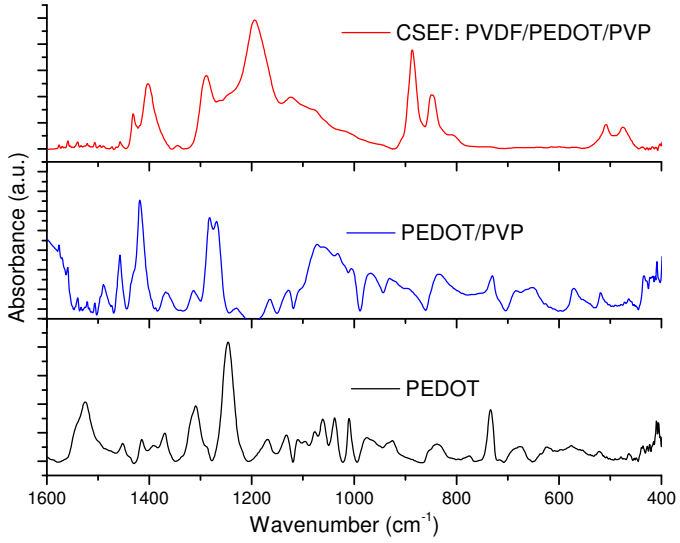

Figure 4.38 Plot comparing FTIR spectrum obtained from core-shell electrospun fibers against the spectrum of spin-coated PEDOT-PVP mixture and PEDOT film

We also attempted to detect any variation in the FTIR spectrum due to presence of PEDOT and PVP in the core fiber. Figure 4.38 shows a comparison of FTIR spectrum from core-shell electrospun fibers against spin coated films of PEDOT and PEDOT-PVP solutions. From the spectrum, we do not notice any effect of presence of PEDOT from the FTIR spectrum of CSEF fibers.

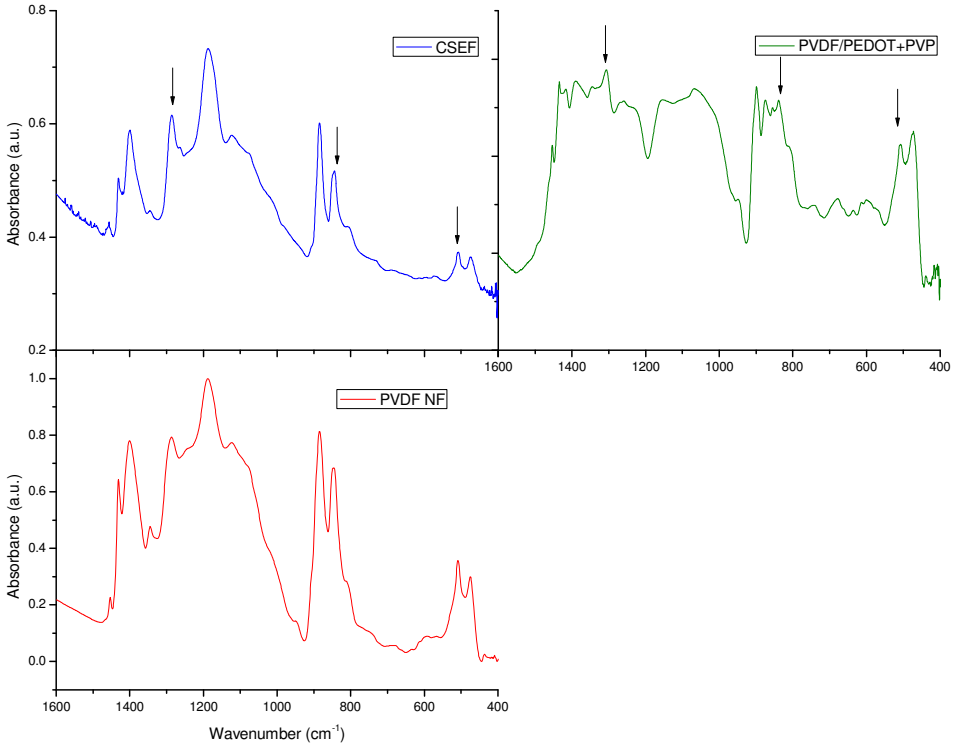

Figure 4.39 FTIR spectrum plots of core-shell electrospun fibers compared against randomly oriented PVDF nanofibers and a layer of PVDF spin coated on top of PEDOT-PVP layer

Similar spectrum was observed from Figure 4.39 of core-shell electrospun fibers. While a PVDF spin coated layer on top of a PEDOT layer shows presence of PEDOT (Figure 4.39), core-shell fiber spectrum was similar to electropsun PVDF fiber mat (indicated by arrows pointing to beta phase wavenumbers). FTIR spectrum of core-shell electrospun fiber mat at various incident points yielded the same spectrum, indicating that the PEDOT core fiber was very thin for sufficient absorption of signal. This was also a good indicator of presence of core-shell fibers, in place of formation of co-spun fibers or splitting of Taylor's cone leading to electrospinning of just PEDOT fibers on the surface.

4.6 SUMMARY

In the present study, we demonstrated that curing of PVDF films increase the beta crystalline phase considerably, using techniques like Raman and Fourier transform infrared spectroscopy. We also showed that the 1μm thick PVDF film based devices demonstrate higher crystallinity compared to the 6μm thick films [91]. These results were further supported by techniques like differential scanning calorimetry (DSC) in the present study. Thinner films show inherently higher crystallinity due to higher stretching during the spin-coating process, without the need for additional electrical poling. Further, electrical poling of the thin films did not contribute substantially towards increasing the film crystallinity. Using techniques like electrical hysteresis, we determined that the crystallinity of our fabricated PVDF films were comparable to the commercially fabricated films.

Towards the fabrication of nanofibers for fabricating more sensitive devices, we assembled the electrospinning setup and optimized all the parameter for fabrication of

nanofibers from PVDF. We used custom fabricated current collectors for patterning high-density highly aligned nanofibers. We also characterized the alignment of the fibers using 2D FFT of the aligned nanofibers SEM images. It was found that higher rotational speeds of the rotating drum led to better alignment of the fibers.

The assembled electrospinning setup was slightly modified for electrospinning of core-shell fibers. We optimized the core material for highest conductivity from an electrospinnable solution. PEDOT based solution was found to be the ideal conducting polymer for the core material. Flurorescein and 1-pyrenebutyric acid were used as the dyes for confocal fluorescence imaging of core-shell fibers. The ease of fabrication of aligned nanofibers and aligned core-shell electrospun fibers allows for development of highly sensitive pressure sensing applications in biomedical field.

Chapter 5: PVDF structure and sensor fabrication

5.1 INTRODUCTION

In the present chapter, we describe the various techniques to assemble devices from the various PVDF structures that were presented in Chapter 4. We describe the fabrication process of thin-film based pressure sensors on silicon wafer as the substrate and later to fabricate the flexible devices. We also present the various shapes and designs of the thin film based sensors that were fabricated and tested in the present study.

We describe the different designs for nanofiber based PVDF sensors. We also compare and contrast the advantages of using core-shell electropsun fibers versus the regular nanofiber based devices though the use of simulation studies. The simulation studies leverage the device design described in the present chapter to predict the signal output that can be achieved by switching from aligned nanofiber based devices to core-shell electrospun based devices.

5.2 THIN FILM SENSOR DESIGNS

Figure 5.1 summarizes the fabrication process for silicon based devices using SU8 to protect the patterned PVDF films from getting damaged. Starting with a silicon wafer, photoresist (AZ5209) was patterned to define the bottom Al electrode (2000 Å thick) using the lift-off process. The PVDF-TrFE was spin coated on the Al-patterned wafer. We used 8 % and 15 % weight/volume PVDF-TrFE copolymer with 1000 rpm for 30 sec to get 1μm and 6μm thickness films, respectively. As a Reactive Ion Etch (RIE) mask to

etch the thin metal film, we replaced AZ5209 photoresist with SU-8 to have a undamaged film. Then the SU-8 mask was removed by remover PG (Clairant, Inc). Dry etch was performed under 100 sccm oxygen gas environment with 200 W RF power and 5 mT pressure. The thin film etch rate was 150 nm/min. Finally, top Cu electrode (2000 Å thick) was patterned by wet etch and the photoresist mask was removed by dry etch.

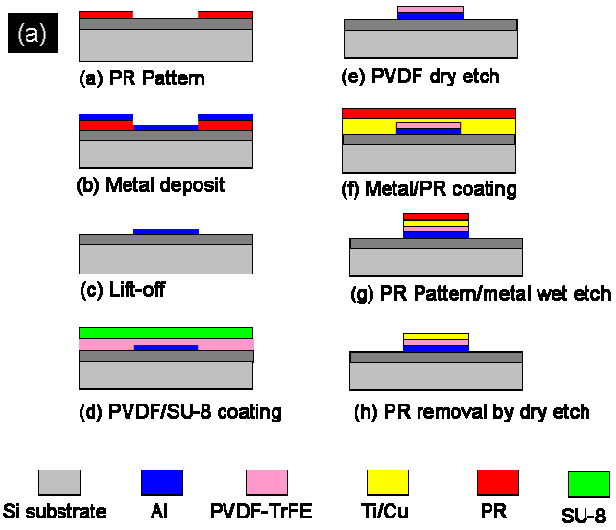

Figure 5.1 Fabrication process using a SU-8 RIE mask

Figure 5.2 shows the various devices that were fabricated using the above technique. Devices as small as 2.5mm to 10mm (one dimension of electrode) were fabricated. Further, devices were patterned with multiple top electrodes and multiple PVDF sensing membranes. However, testing of these devices proved to be difficult due to the incomplete removal of SU8 from top and the harsh chemicals used in the current

process. In order to circumvent this, we re-designed the same process to avoid using SU8. In place of SU8, AZ photoresist itself was used as the mask to pattern the features.

Figure 5.2 Photograph of the actual PVDF thin-film based sensors fabricated (top) and the fabricated MIM structured pressure sensors of single and quadruple membrane devices (bottom)

Figure 5.3 summarizes the revised process. Using this process, two different designs of electrodes on PVDF were fabricated: (1) Parallel type: electrodes on the same side, where the electrode can be further patterned into dual and quadruple shape; and (2) Sandwich type: PVDF thin film sandwiched between the electrodes. The different device designs have been illustrated through Figure 5.4 and Figure 5.5. For the fabrication of these devices, starting with a silica coated wafer, photoresist was patterned to define the bottom Al electrode (2000 Å thick) using the lift-off process. It was important to have

silica grown wafer in place of a regular silicon wafer as silica aids in the adhesion of PVDF thin-film to the surface. PVDF-TrFE was spin coated on the Al-patterned wafer. Then another patterned photoresist was used as a Reactive Ion Etch (RIE) mask to pattern the PVDF-TrFE thin film. The dry etch was performed under 100 sccm oxygen gas environment with 200 W RF power and 5 mT pressure. The PVDF-TrFE thin film etch rate was 150nm/min. The photoresist mask was etched simultaneously with an etch rate of 100nm/min and dry etch was continued until the photoresist mask was etched fully.

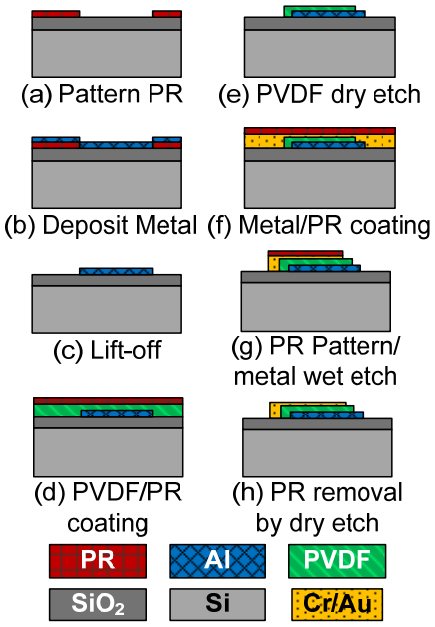

Figure 5.3 Schematic showing the fabrication process without using SU8

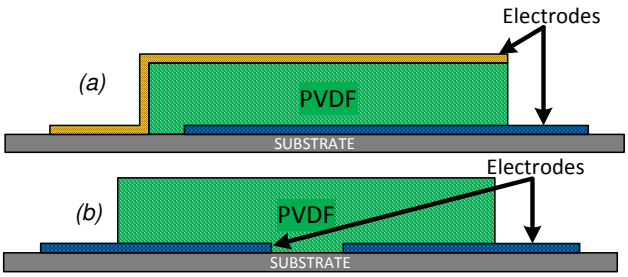

Figure 5.4 Schematic of the cross-section of: (a) sandwiched design, (b) Parallel design, for the PVDF-TrFE films that can be fabricated

Top Cu electrode (2000 Å thick) was patterned by wet etch and the photoresist mask was removed by dry etch. Using this recipe, we fabricated single, dual, triple and quadruple membrane geometries in the following bottom electrode sizes: 1x1 and 1.5x1.5 cm^2. Further, parallel electrode devices were also patterned using just the top mask to pattern the electrodes on one side of the membrane. Figure 5.6 shows few of such fabricated devices.

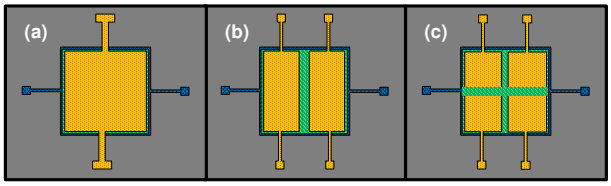

Figure 5.5 Schematic showing the top-view of: (a) single, (b) dual, (c) quadruple, electrodes in sandwiched structure. The bottom electrode could be 0.5x0.5, 1x1 or 1.5x1.5 cm^2

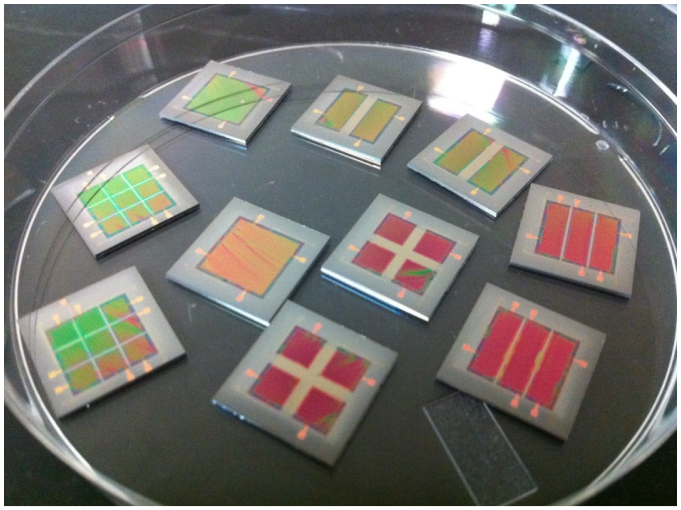

Figure 5.6 Photograph showing the various 1.5x1.5cm2 devices fabricated on the silica coated wafer

These devices were all fabricated on silicon wafer or on a hard substrate so far. To fabricate flexible sensors, adhesive backed Kapton (polyimide) tape (McMaster Carr, 0.0025" thick) was placed on the SiO_2 surface of the substrate with the remaining process being the same (Figure 5.3). However, in order to fabricate highly conductive electrode and electrode pads, the thickness of the metal deposition was increased to 3000 Å. Kapton was chosen as the substrate due to its robust chemical, mechanical, thermal, electric and biocompatible properties. Once complete, the devices were peeled off the wafer and placed on the desired surface for testing. Figure 5.7 shows the flexible devices that were fabricated using the current technique. The individual devices were easily diced either using a scalpel blade or scissors.

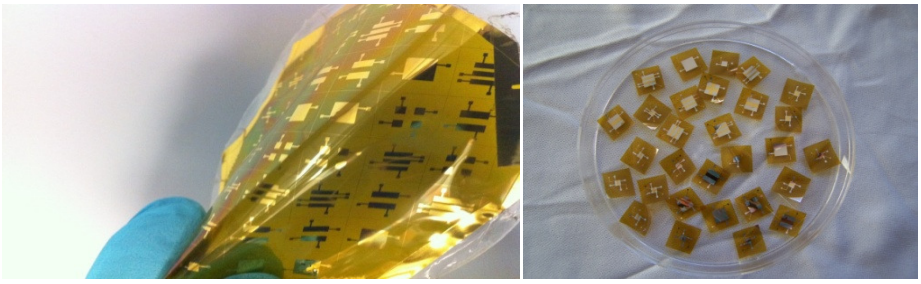

Figure 5.7 Images of the first-generation flexible pressure sensors on kapton film

Since kapton film is polymeric and carries surface static charge, it was anticipated to generate false signal when coupled along with the charge amplifier. In order to overcome this, we coated the entire bottom surface area available, with ground electrode material. Figure 5.8 shows the fabricated structures with completely covered bottom electrode (aluminium).

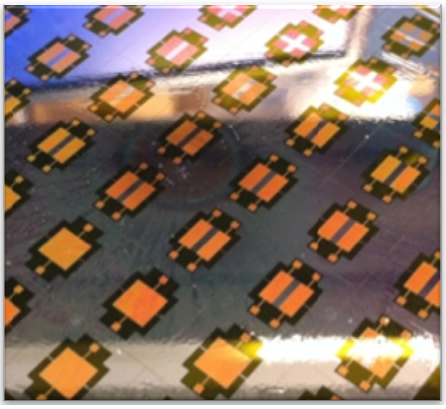

Figure 5.8 Photograph of the second generation of flexible devices with aluminium (bottom electrode) covering maximal surface area to avoid external electrostatic interference

Even though the thickness of the metal electrode layer was increased for the flexible sensor devices, all these designs showed poor connectivity with the external electrical wirings. This was primarily due to the thin nature of the patterns connecting the electrodes to the electrode pads. In order to circumvent this problem, we redesigned the device pattern. Further, since these devices were required to be compatible with catheter-surface mounting, we designed the new devices to be in a longer format. Figure 5.9 shows the final design of these flexible PVDF based devices fabricated in the present study. Copper was used as the bottom electrode and aluminium was used as the top metal electrode. Only the area where the two metal electrodes overlap was functional in nature. Therefore, the functional device geometries were $2x10mm^2$, $1x10mm^2$, $2x5mm^2$ and $1x5mm^2$. All these geometries were fabricated on a single wafer for multiple simultaneous testing. We also patterned few devices with completely covered bottom electrode in $2x10mm^2$ format, as visible in Figure 5.9.

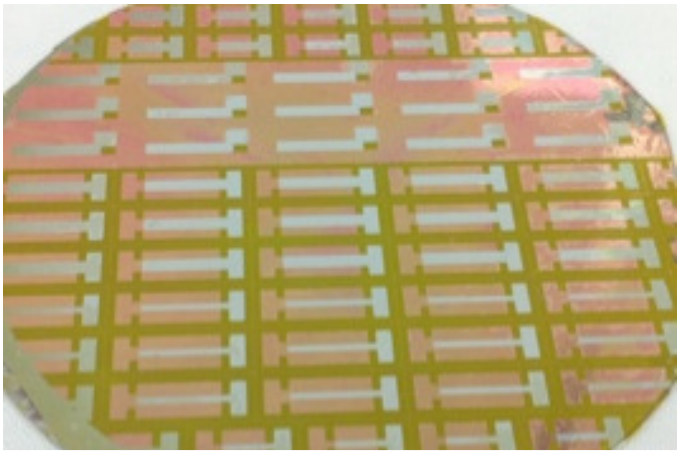

Figure 5.9 Photograph of the final design of flexible devices using copper as the bottom electrode and aluminium as the top metal electrode

5.3 NANOFIBER SENSOR DESIGNS

The goal of the present study is to fabricate flexible pressures sensors that can be mounted on catheter. Figure 5.10 shows the schematic of dual pressure sensors mounted on either side of a balloon along with the schematic of aligned nanofiber based pressure sensor.

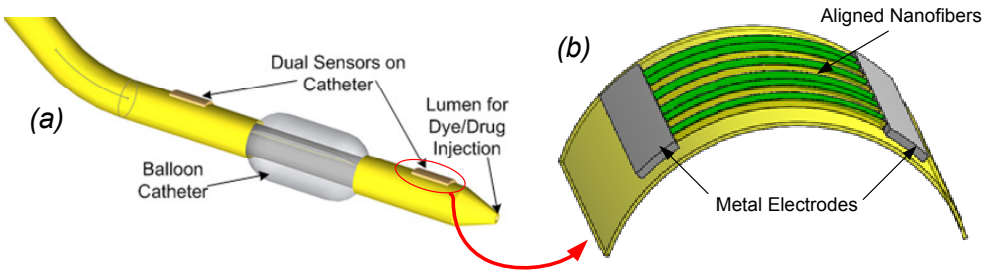

Figure 5.10 Schematic showing (a) placement of pressure sensors on either side of balloon on a catheter, and (b) highly aligned nanofibers based pressure sensor

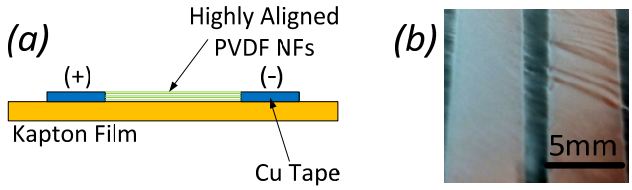

Figure 5.11 (a) Cross-section schematic of the device fabricated on flexible kapton (polyimide) film; and (b) photograph (top-view) of the actual device fabricated with aligned nanofibers stretching between the copper tape electrodes from a rotating drum assembly

In order to fabricate highly aligned nanofiber based devices, initially copper tape (5mm wide) strips were placed adjacent to each other on a flexible kapton film with 1mm

spacing between them. This entire kapton film was wrapped around the rotating drum assembly and highly aligned nanofibers were electrospun directly on top of substrate, as shown in Figure 5.11.

Moving forward, copper tape on kapton film was replaced with patterned metal deposited directly on kapton film. The devices had a functional surface area of 10x4mm^2, as shown in Figure 5.12. Copper (350nm) metal electrode was deposited using photoresist lift-off and e-beam deposition.

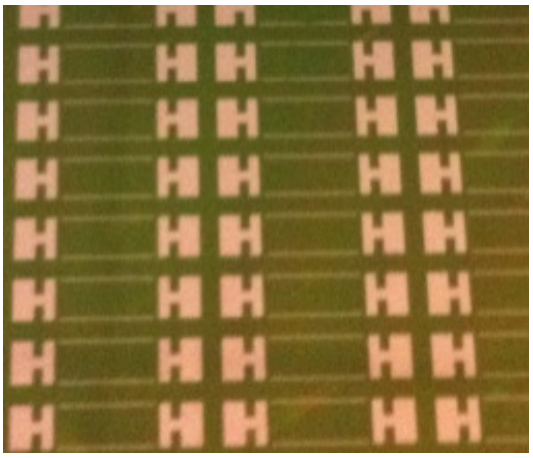

Figure 5.12 Photograph showing first generation design for nanofiber based devices

The above patterned kapton film was wrapped around the rotating drum assembly and aligned nanofibers were electrospun directly on to the devices. The electrospinning was carried out in a manner such that the electrospun fibers were aligned lengthwise on the device. In other words the length of every nanofiber making contact with both the electrodes was 10mm.

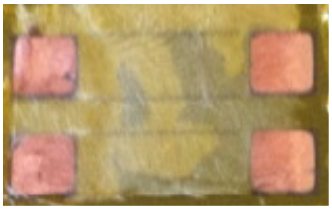

Figure 5.13 Photograph showing aligned nanofiber devices coated with top metal electrode pad

In order to anchor the electrospun fibers down on the kapton film and increase the electrical connectivity of the fibers with the patterned electrodes, a thick layer of copper (350nm) was patterned on top using a hard shadow mask (fabricated using 3D printer), as shown in Figure 5.13. For external connectivity to these devices, electrical wires (32 gauge) were directly connected to the top metal electrode pad using silver print (MG Chemicals). The wire-electrode pad connection was then covered with UV curable epoxy (NOA 81, Norland optics). The whole device was then placed on a glass slide and spin coat covered with low-viscosity UV curable epoxy (NOA 89, Norland optics).

A problem with the first generation design of nanofiber based devices, was the need for longer nanofibers. The nanofibers had to be 10mm long to make an active device. Further, any charge generated at the center of a 10mm long nanofiber would not be able to reach either of the electrode pad due to the high impedance of PVDF-TrFE as a material. Therefore, we fabricated the second generation design for nanofiber based devices such that a nanofiber had to be only 4mm long (Figure 5.14). The second

generation design also allowed for higher number of fibers to be present in a single device compared to the previous design.

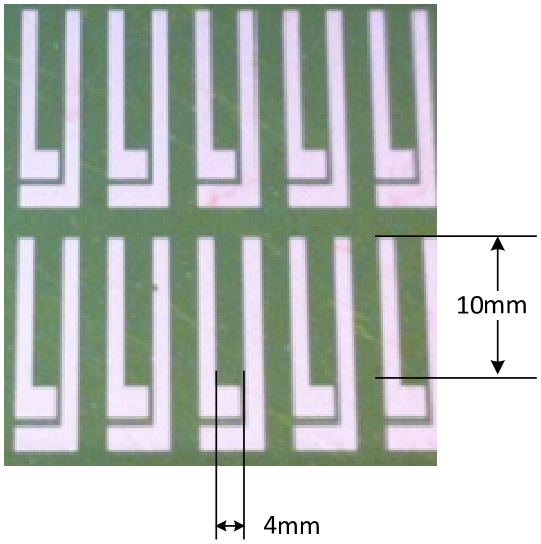

Figure 5.14 Photograph showing second generation design for nanofiber based devices

Electrospinning of nanofibers was done in the same manner as before, by wrapping the kapton film around the rotating drum setup. In order to anchor the fibers down on kapton film top metal (copper, 350nm thick) was again deposited using anoter hard shadow mask. The electrical connections to the devices and assembly of devices were done in the same manner as described above.

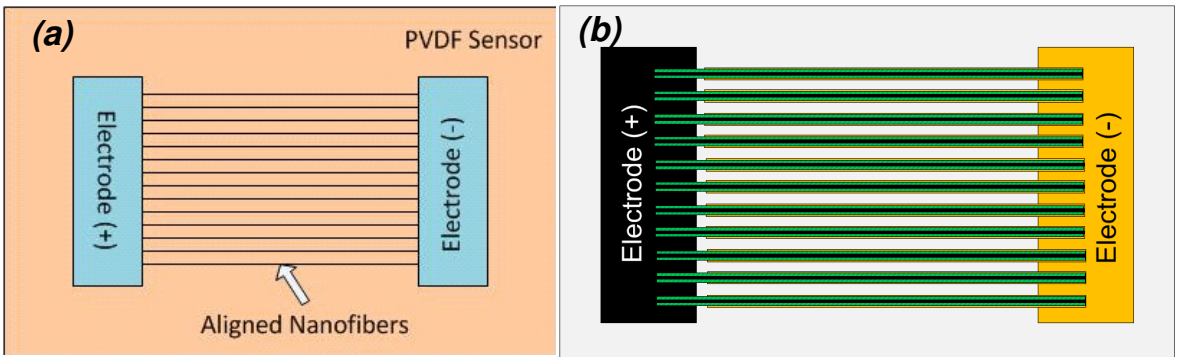

Figure 5.15 Schematic of devices fabricated from (a) Highly aligned PVDF nanofibers, (b) PMMA-PVDF core-shell fibers with external metal coating

For fabrication of core-shell based nanofibers, we used the second generation type device pattern. The goal was to fabricate aligned core-shell fibers stretched between two electrodes, as shown in Figure 5.15. Core-shell fibers were electrospun using core-shell setup on the patterned kapton film substrate. Figure 5.16 shows the core-shell electrospun substrate with fibers that were aligned from left to right direction. Even though the electrospun fibers were covering the entire available surface area, electrical connections to the conductive core still needed to be established.

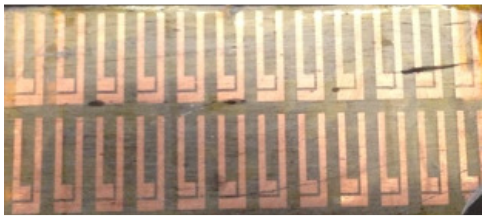

Figure 5.16 Photograph showing aligned core-shell electrospun fibers directly on top of patterned substrate

The open circuit potential of the devices was found to higher than 1GΩ (measurable limit of the digital multimeter). In order to connect the conductive core to the electrode collector, silver print was used along the length of the electrode (Figure 5.17a). Silver print contains organic polar solvents which help dissolve the PVDF-TrFE coating and establish a conductive connection to the core PEDOT-PVP fiber. Control experiments were done where both the electrodes were covered with silver print to short circuit the devices and the resistance of the devices fell to 1.5MΩ, which also happened to be the resistance of a bulk (spin-coated) PEDOT-PVP film (1cm length). This is an indication of good connectivity of the core-fiber with the electrode pad.

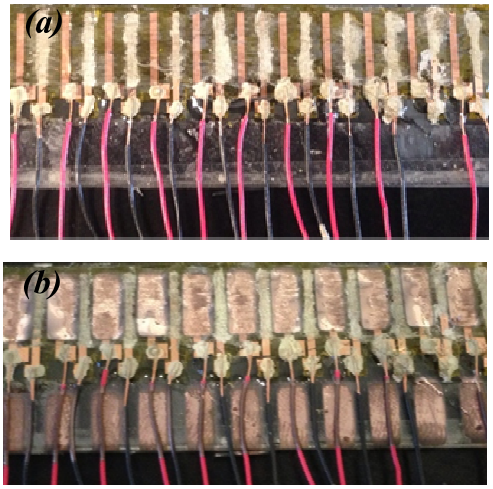

Figure 5.17 Photograph showing (a) silver-print coated along electrode length for connection of core fibers, and (b) top metal coated set of devices

In order to connect the PVDF shell material to the other electrode, copper metal was e-beam deposited from top (350nm) using a hard shadow mask. Figure 5.17b shows the photograph of the final devices. The resistance between the two electrodes was still

greater than 1GΩ, indicating good core-shell assembly of fibers. Electrical wires were connected to the electrode pads using silver print, as shown in Figure 5.17. The devices were spin coated with UV curable epoxy (NOA 89) for external passivation.

5.4 SUMMARY

We described the process of fabricating thin-film based devices. Different sizes and electrode patterns were easily fabricated. The same fabrication technique was transferred to kapton substrate for fabrication of flexible devices. Due to the thin patterned electrode connections, the device pattern was shifted to longer device type with thick electrode connections. These devices were more suitable for catheter mounting application as well.

We also described the device designs used for nanofiber based devices fabrication. The same optimized design was used for fabrication of core-shell devices. By coating top metal electrode after electrospinning of nanofibers, we made sure that the nanofibers were well attached to the flexible substrate, both mechanically and electrically. Further, we demonstrated successful fabrication of core-shell fiber based using the appropriate controls.

Chapter 6: Sensor characterization

6.1 INTRODUCTION

In the present chapter, we first present a brief overview of the previously used testing procedures for sensors using PVDF. We will also justify to why these techniques cannot be used in the present study. Later on in the chapter, we then present the testing procedure that we used for our PVDF sensors.

The different testing chambers along with the results obtained from the chambers are presented later in the chapter. Output from all the different types of PVDF sensors (Chapter 5) are described and compared for sensor comparison.

6.2 PREVIOUS TESTING METHODOLOGY

Testing of pressure sensors usually requires subjecting the pressure sensor to a known value of pressure using physical means, followed by calibration of the signal generated from the sensor against the actual value of the pressure. Subjecting the PVDF structures to pressure causes stress in the structure, which leads to surface charge generation. The deformation in the PVDF film could be due to the deflection of a film or due to compression. Based on the mode of deformation in the film, there have been two major testing methodologies for PVDF based pressure sensors.

Figure 6.1 shows the schematic of the deflection based testing assembly. In such a system, the PVDF film is usually clamped at both the ends such the film is suspended inside the housing. When pressure is applied on the sensor, it leads to deflection in the suspended film, generating an electrical charge and voltage signal. The charge is

collected through the two electrodes and transmitted to the external circuitry. The drawback with this testing method is that the PVDF films or structures need to thick so that it can suspended and ensure that it would not irreversibly deform when pressure is applied.

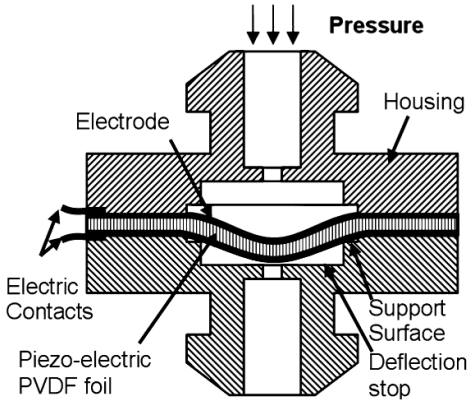

Figure 6.1 Schematic of deflection based pressure sensors. Source: Pressure sensor from a PVDF film

With our thin films being substantially thinner (1μm) compared to the films tested previously. Further, pulling off such thin films from the substrate surface might lead to mechanical stretching of the film and further thinning. A more practical approach for testing of thin film based devices is by using the compression testing setup, as shown in Figure 6.2. The sensor device is placed on a fixed support. Compression is introduced to the fixed sensor using an external vibrator. A commercial force transducer can be simultaneously coupled to this vibrator for calibration of the force transferred to the sensor under test. The signal obtained from the sensor under test can be compared against the spectrum obtained from the commercial force transducer for calibration purposes.

Compression mode of testing is more suitable for thin film based devices, as is in the present study. However, reduction in the device size increases the scope of external electrostatic interference. The effect of electrostatic interference is further worsened by the presence of the probe, which is difficult to ground and the absence of a faraday's cage around the sensor under test to shield the stray charges. As the device size shrinks, the amplification on the charge amplifier needs to be increased to compensate for the loss in sensitivity. Employing any physically moving object for force transduction on such a small sensor can lead to false signal generation, corresponding to the movement of the probe itself.

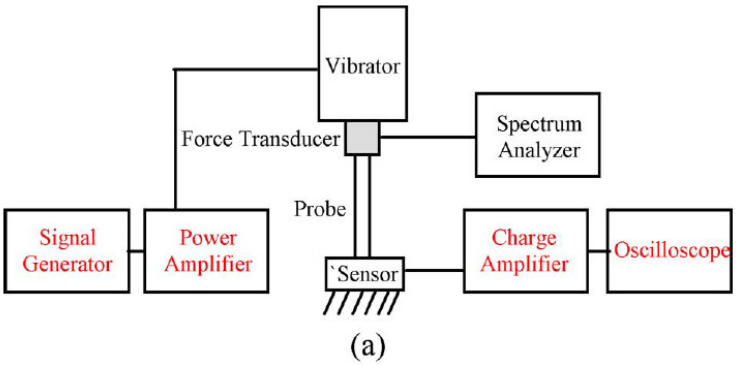

(a)

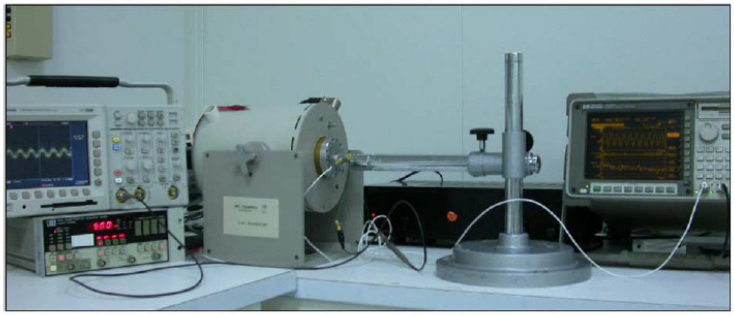

(b)

Figure 6.2 Schematic and photograph of deformation based pressure sensors. Source: Flexible Dome and Bump Shape Piezoelectric Tactile Sensors Using PVDF-TrFE Copolymer

6.3 CHARGE AMPLIFIER

The piezo-electric PVDF film, like other piezoelectric sensors, is not accurate for measurement of static pressures due to the discharging of the surface charges [131]. Therefore, only dynamic pressures with a minimal frequency of about 0.01Hz can be measured using PVDF based sensors [131]. When the pressure subjected on the film deforms the PVDF film, an electric charge and voltage is generated on the electrodes. This electric signal can be measured with a simple electric circuit. However as the device size keeps shrinking, the signal intensity deteriorates due to the lower amount of piezoelectric material contributing to the charge generation. In order to compensate for the poor signal quality, a charge amplifier can be used.

Most of the commercial charge amplifiers are based on the principle of grounding one of the transducer electrodes. Larger gains in efficiency are likely to be realized by the design and fabrication of a charge amplifier that is properly coupled to the characteristics of the specific sensor. Efficient removal of surface charge from the PVDF requires extremely high device input impedance. In the present study, we used two different charge amplifiers. One was a commercial charge amplifier (Measurement specialties Inc.) providing output gain of 40dB. For recording simultaneous input from dual sensors, a dual-channel charge amplifier was also assembled, capable of up to 60dB gain. The electrical circuit for the custom-built charge amplifier is shown in Figure 6.3a. OPA227 and AD620 were used to convert the high impedance signal to low-impedance signal and for output voltage amplification, respectively. The feedback capacitance, which determines the sensitivity of the charge amplifier, was selectable from 3pF-100μF. The

resulting custom-built charge amplifier contained two of the above described circuits (Figure 6.3b) to enable simultaneous reading of two PVDF sensors.

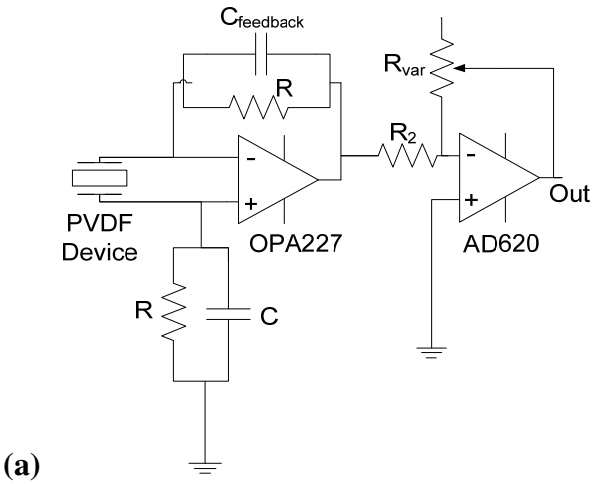

(a)

(b)

Figure 6.3 Thin-film sensor charge amplifier circuit. (a) Circuit schematic of a single channel charge amplifier, and (b) photograph of the custom-built dual channel charge amplifier

6.4 MANUAL TESTING

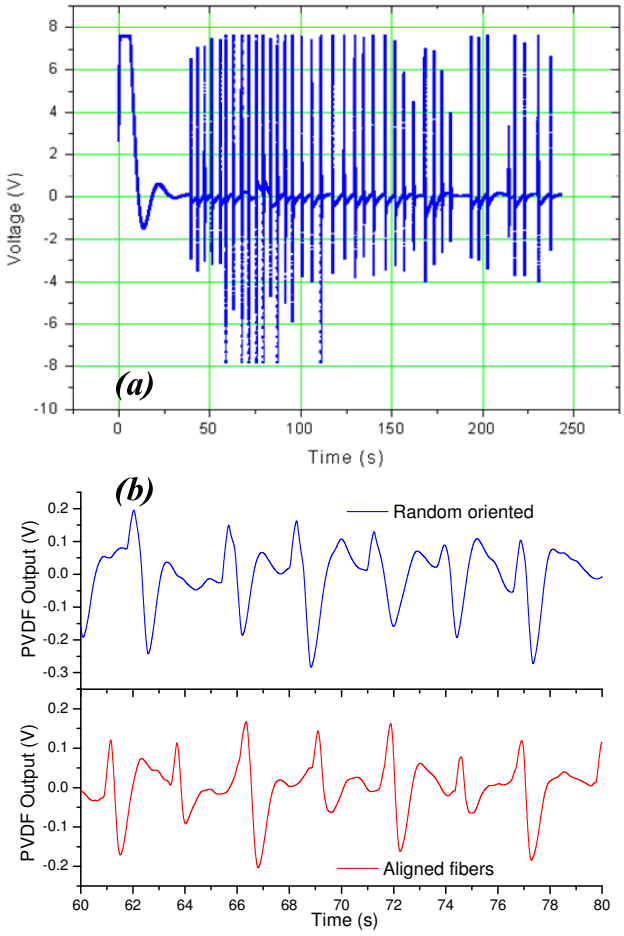

Figure 6.4 Plot of device output obtained by manual testing of: (a) thin-film, and (b) nanofiber based devices

Manual testing of sensors involves application of pressure on the PVDF sensors by manual tapping using a probe similar to what the vibrator achieves in Figure 6.2. The main difference, however, is that there is no external force transducer to corroborate the magnitude of the applied pressure. Therefore, manual testing by manually tapping using a

probe on the sensor surface serves as a quick method for testing the functionality of the devices.

0 shows the response obtained from various PVDF sensors by manual tapping. The devices showed good initial response, corresponding to the pressure input. This technique can also be used to study the hold-and-release characteristics of the device, which can provide important information about the device response time and its piezoelectric nature.

6.5 FLOW CHAMBER

In order to overcome the challenges associated with the testing of a miniature sensor using the conventional testing methods presented above, we tested the sensors using air pressure inside a custom-fabricated chamber. The current Figure 6.5 shows the schematic of the pressure sensor measurement in air chamber. A 5x5x6 cm^3 chamber was fabricated. Air was introduced into the chamber through the inlet and venting of air was controlled to manipulate the air pressure inside the chamber. The PVDF device was placed at the center of the chamber. The backside of the device was taped to the device holding plate. Both, the device and the sensor were so placed that the sensing element was perpendicular to the direction of the air flow and hence compression-induced signal from the commercial sensor and the PVDF devices due to air pressure was recorded. The pressure on the PVDF sensor was determined using commercial pressure sensor (Freescale Semiconductors, MPX2300DT1). The commercial pressure sensor was supplied an input of $5V_s$, making the sensitivity upto 25.3μV/mmHg. Table 6.1 summarizes the properties of the commercial pressure sensor used. Any possible leakages

from the chamber were prevented by the use of neoprene o-ring and vacuum grease. Air pressure and flow inside the chamber was manipulated using the multiple outlet valves.

Table 6.1 Properties of the commercial pressure sensor. Source: Freescale website

Characteristics	Typical
Pressure Range	0-300mmHg
Supply Voltage	6 Vdc
Supply Current	1 mAdc
Sensitivity	5 µV/V/mmHg

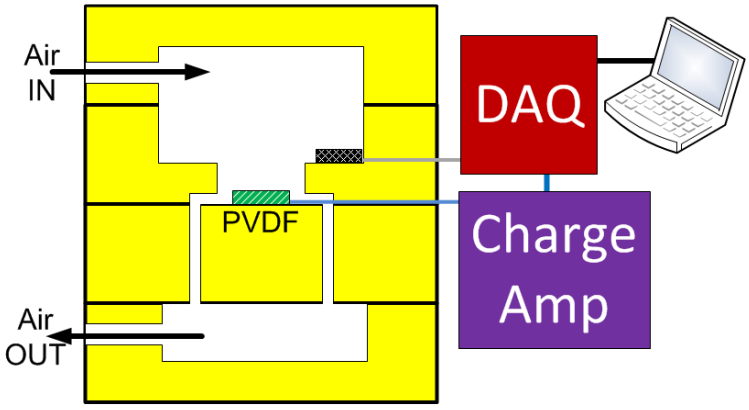

Figure 6.5 Schematic showing the working principle of the flow chamber for PVDF sensor testing

In the present study, we fabricated two different prototypes of flow chamber for testing of PVDF sensors. Both designs were fabricated using the 3D rapid prototyping

machine (BME, UT Austin). Figure 6.6 shows the schematic and photograph of the first type of flow chamber testing setup.

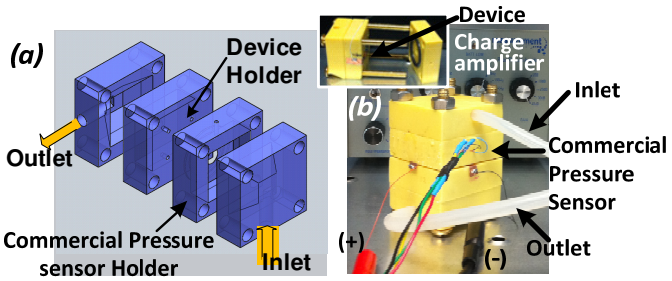

Figure 6.6 (a) Schematic showing chamber with air flow through the system; and (b) actual photograph of chamber in the testing setup

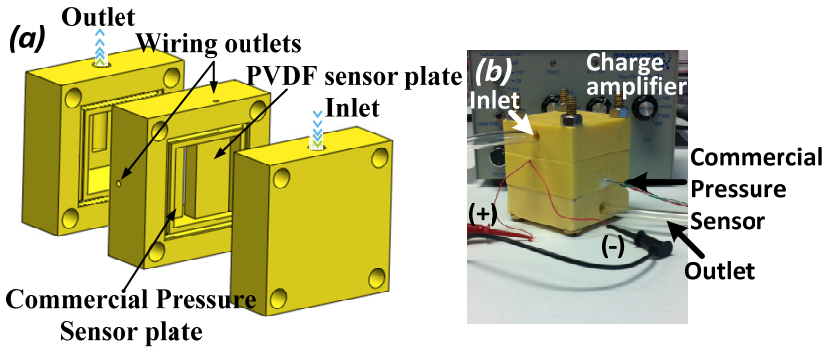

Figure 6.7 Flow chamber assembly for sensor measurements. (a) Schematic showing chamber with air flow through the system; and (b) actual photograph of chamber in the testing setup

The first type of flow chamber contains four plates based system, which allows for a compact assembly and thinner plates. However, the newer design (Figure 6.7)

allows for placement of both the PVDF sensor and the commercial pressure sensor on the same level, allowing for more accurate sensor calibrations.

Air flow into the chamber was controlled using a flowmeter (Dwyer instruments) before the inlet and a multiple outlet valve after the inlet. Flow rate combined with the number of open outlet valves were used to generate air pressure inside the chamber in the 0-300 mmHg range. This also happens to be the physiological pressure range over which the PVDF sensor needs to be operational. The two electrodes of the PVDF devices were connected to the terminals of the charge amplifier (Figure 2b), as described above. Charge amplifier setting were always kept on 40 dB gain (100x amplification), 100 nF feedback capacitor, 0.1-10Hz bandpass. All data was recorded after 40dB gain but was scaled to 0dB before plotting. Outputs from the charge amplifier were connected to a USB-type (6009) Data Acquisition Kit (National Instruments). The output was further filtered using a digital low-pass filter (set to 8Hz) with Infinite impulse response filter set to inverse Chebyshev filter of order three. A low threshold values of 8Hz was selected for the low pass filter because most of the physiological processes occur at 1-3Hz range, corresponding to 60-180 heart beats per minute. The chamber plates were sealed using custom-shaped o-ring made from flexible silicone elastomer. The electrode pads of the PVDF devices were connected to external wires using silver print (GC electronics).

In order to further automate the air pressure control, we connected the air inlet to a solenoid valve (Figure 6.8). Both, the device and the sensor were so placed that the sensing element was perpendicular to the direction of the air flow. The inlet was kept at a certain air flow rate, while the exit of air from chamber was controlled using a multiple

valve exit. The solenoid valve was connected to the same data acquisition kit, which also served the purpose of PVDF sensor signal acquisition. The switching frequency of solenoid valve was controlled using LabVIEW program. By controlling the switching frequency, we could manipulate the air pressure cycling frequency inside the chamber.

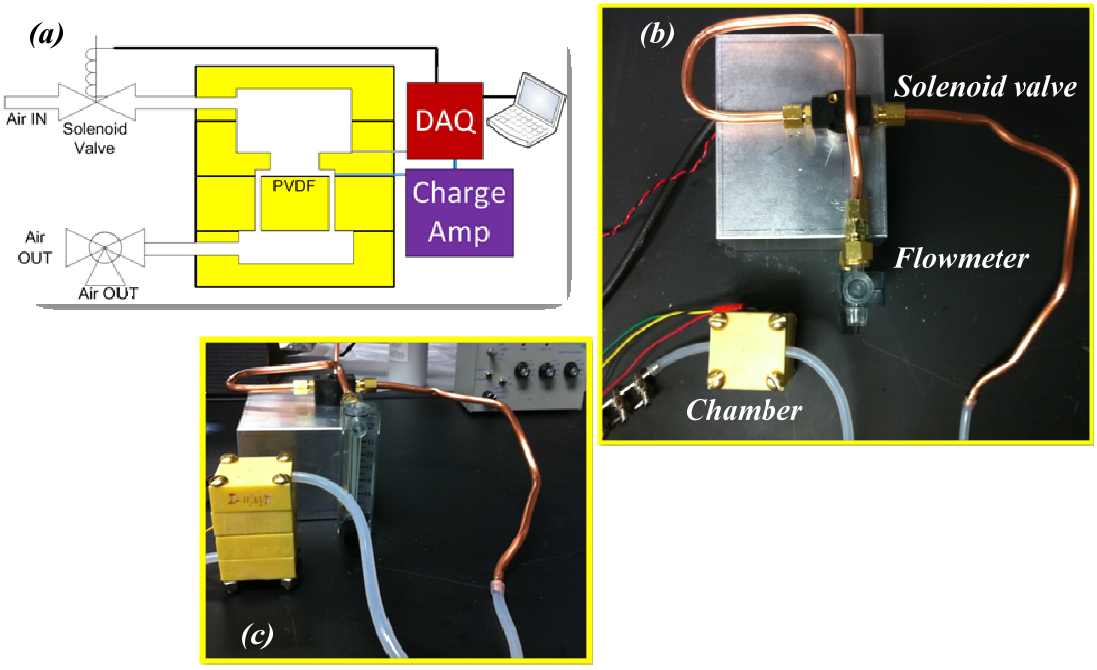

Figure 6.8 (a) Schematic of the automated air flow control system; (b), (c) photographs of the actual setup showing the solenoid valve feeding air to the chamber

6.5.2 Air based testing

When the devices were place inside the flow chamber and air was used to create ambient pressure, the responses were immediate and very reliable, having very fast recovery time. **Error! Reference source not found.** shows experimental results of

output voltage for a dual PVDF-TrFE film sensor (1x1 cm^2 bottom electrode surface area) when exposed to impulses of air pressure in the chamber. When exposed to the same pressure amplitudes, similar outputs were observed though the charge amplifier. The two different top electrodes on the same device showed a fast recovery time, 0.17 sec and 0.23 sec, respectively.

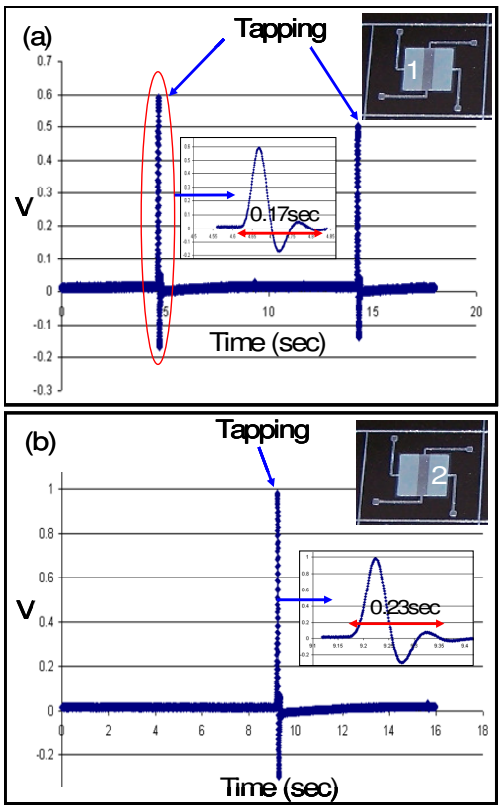

Figure 6.9 Experimental results of output voltage for pressure sensor having dual PVDF-TrFE film, showing 26% recovery time mismatch between two membranes and 9% repeatability

Such recovery times correspond to an efficient resolving frequency of up to 5Hz. This happens to be in the physiological sampling rates, as most of the physiological phenomenon occurs at 1-3Hz, corresponding to 60-180 beats per minute.

Figure 6.10 shows the hold-and-release output response obtained from a single PVDF pressure sensor fabricated (in blue color; online) corresponding to the pressure the PVDF device was subjected to, inside the chamber. The response obtained from the PVDF devices show the typical dynamic response expected from piezoelectric PVDF films. The pressure inside the chamber was measured using the commercial pressure sensor, indicated by the right vertical axis in Figure 6.10. The negative voltage peak corresponds to the compression of the membrane and the positive direction peak corresponds to the relaxation of the membrane.

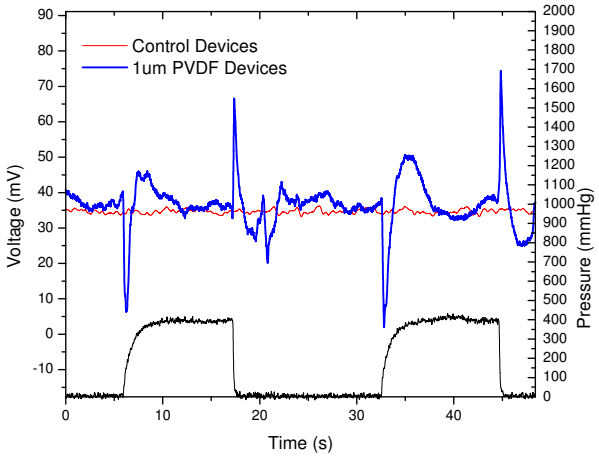

Figure 6.10 Response from PVDF-TrFE devices on hold-and-release pressures inside the air chamber showing the true dynamic behavior of the piezoelectric PVDF films

The relaxation response from the PVDF film is a combined function of its spring constant and the damping factor. Response from control devices is shown in red, when exposed to similar pressures. Control devices were assembled in exactly the same manner as normal devices but did not have any PVDF membrane present.

For different magnitudes of pressure inside the chamber, the peak voltage from the PVDF devices were obtained and plotted as shown in Figure 6.11. The graph shows a linear response for the PVDF based pressure sensors in physiologically relevant pressure range. Further, we notice that the slope is higher for 1µm devices compared to 6µm devices, indicating higher sensitivity from thinner devices. Results indicate that the fabricated pressure sensor shows near β-phase formation in the film even after standard lithography techniques.

Figure 6.11a compares the dual membrane design with the quadruple membrane design for 1.5 x 1.5 cm^2 devices. Only one of the top available electrodes was connected at a given time. The standard deviation for all the data observed was low (< 4%). The ratio of slope in the two plots was 2.3 for dual over the quadruple. This ratio of slope was as expected due to nearly double functionally active surface area for the dual membrane design compared to the quadruple membrane design.

This ratio of slope was also found to remain the same when the PVDF film was not etched, indicating that it is the area between the electrodes which contributes towards the signal output. In other words, there was no contribution from areas of the PVDF film which was not covered by metal electrodes.

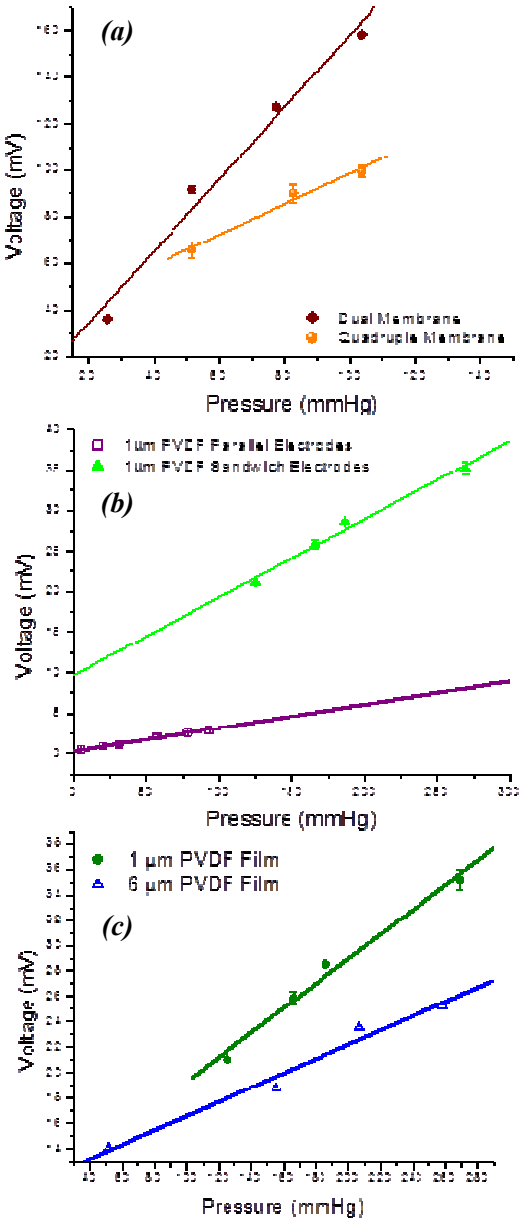

Figure 6.11 Characterization of design variations for PVDF-TrFE devices (1.5x1.5cm^2). (a) high sensitivity of dual membranes comparing to quadruple membrane of 1µm thick PVDF film, the ratio of the slope was 2.35; (b) higher sensitivity of sandwich devices (3.33 times) comparing to parallel electrode on devices; (c) sensing performance of thin and thick films in the air chamber

Figure 6.11b compares the performance from PVDF devices with Parallel electrodes vs. the Sandwich type electrodes. As expected, the sandwich type devices perform better (more than 3 times higher sensitivity) compared to parallel electrodes. This is because the piezoelectric coefficient for PVDF working in compression mode, d_{33}, can be more than two times higher than the lateral stretching mode, d_{31} [95].

Figure 6.11c shows the improved performance obtained from a thinner film (1 µm) compared to a thicker (6 µm) PVDF film.

We observed nearly 1.7 times higher signal output from the 1µm PVDF device compared to 6µm devices, indicative of the higher piezoelectricity of thinner film. This is possible due to the higher surface tension involved in the formation of a thinner film during spin coating, resulting in higher crystallinity in thinner films compared to the thicker films.

Previously, we demonstrated that curing of PVDF films increase the beta crystalline phase considerably [91] using techniques like Raman and Fourier transform infrared spectroscopy. We also showed that the 1µm thick PVDF film based devices demonstrate higher sensitivity compared to the 6µm thick films [91]. These results were further supported by techniques like differential scanning calorimetry (DSC) in the present study. Thinner films show inherently higher crystallinity due to higher stretching during the spin-coating process, without the need for additional electrical poling.

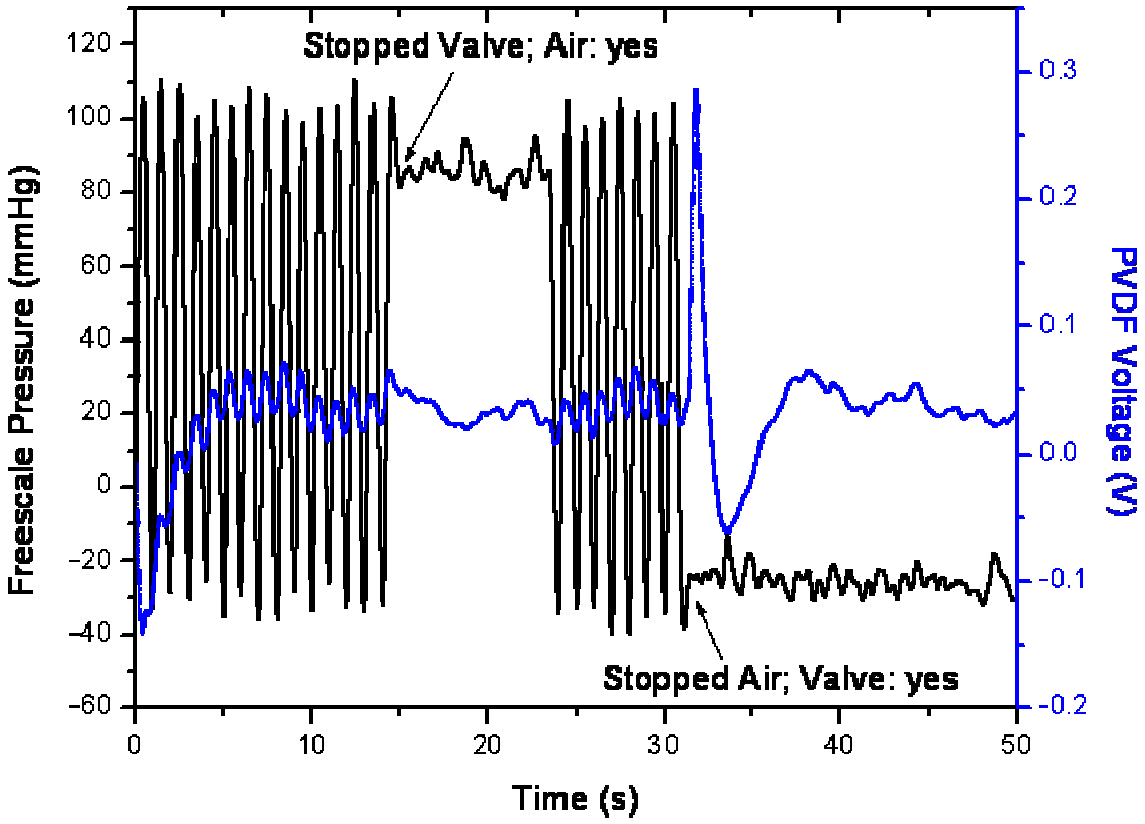

Figure 6.12 Plot showing the PVDF sensor response to automated air pressure in the flow chamber

When automated air pressure was used, we still got excellent signal, with peak-to-peak matching, from the PVDF sensors. Figure 6.12 shows the signal obtained from PVDF sensor in real-time, against the signal obtained from commercial freescale pressure sensor in the same chamber. Albeit the amplitude of the PVDF signal is low, compared to the signal from commercial pressures sensor, the low amplitude is due to the large release peak, observed around 33s, when the flow of air into the chamber is stopped. The PVDF sensor does not show any signal between 15-23s, when the air flow into the chamber was

maintained but the solenoid valve was stopped. Therefore, there was no pressure inside the chamber, which is clearly depicted by the PVDF sensor, as expected.

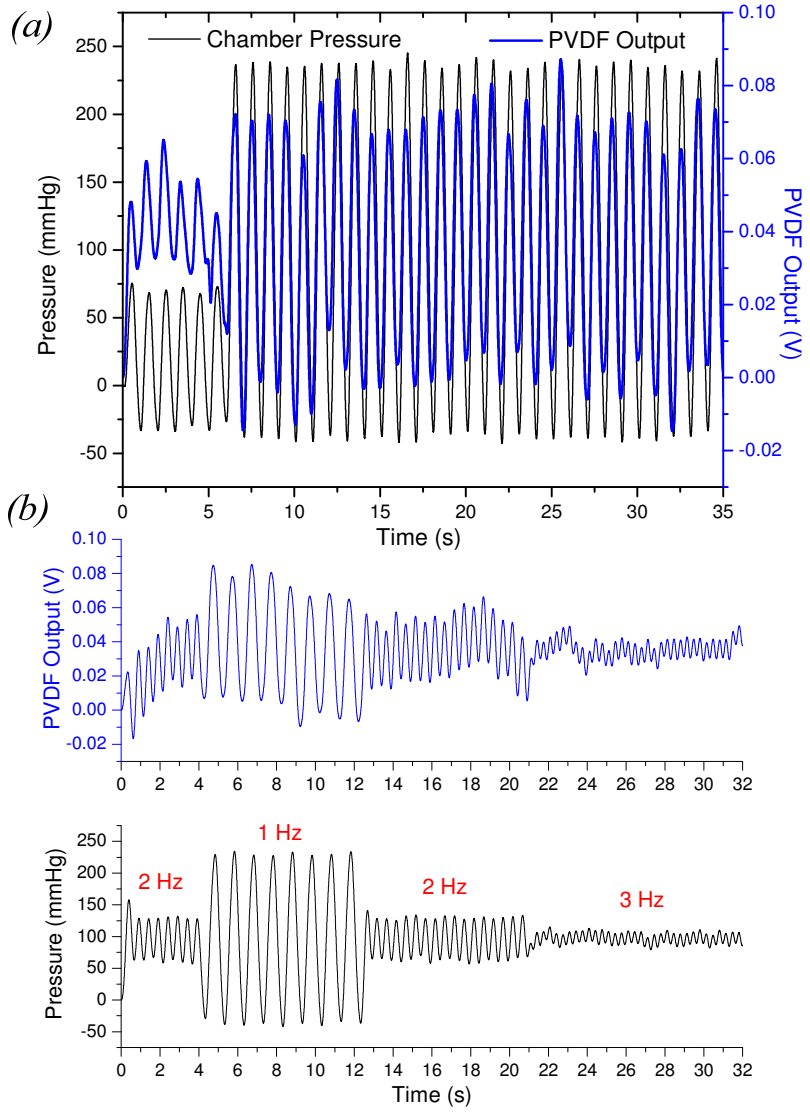

Figure 6.13 Comparison of real-time pressure measurements using PVDF thin-film sensor (blue curve) and Freescale pressure sensor (black curve) as a function of the (a) ambient pressure change in chamber; and (b) chamber pressure frequency

Further testing of the PVDF sensors was done for response to the variation in the air pressure. The solenoid valve was set to operate at a frequency of 1Hz and the flow rate into the air chamber was increased.

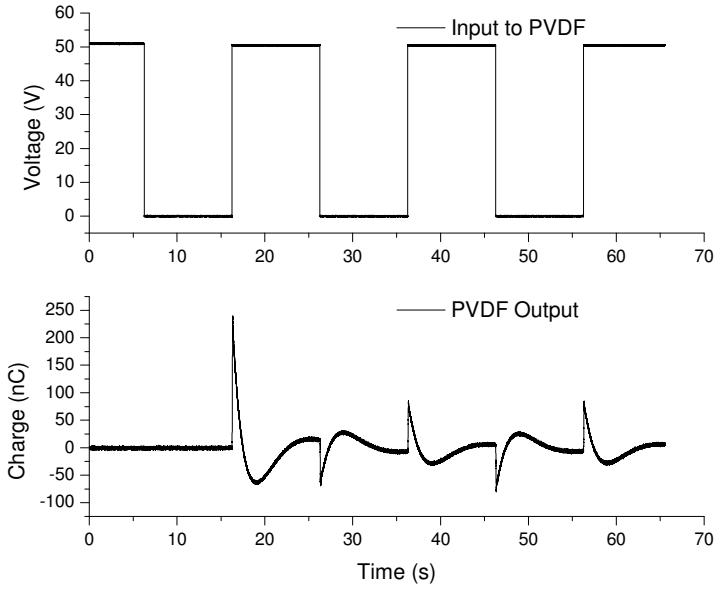

Figure 6.14 Plot showing the input voltage (top) to a PVDF thin film device and the resultant output charge obtained (bottom) from the device

The devices showed perfect peak-to-peak correlation compared to the commercial pressure sensor (Figure 6.13a). An increase in the input flow rate increased the chamber pressure and similar result was observable using the PVDF pressure sensor in the air chamber. By keeping the air in-flow rate constant and varying the solenoid valve operating frequency, the air pulsating frequency in the chamber could be varied. Again, the PVDF pressure sensors show a good correlation with the commercial pressure sensors (Figure 6.13b). Electrical impulse inputs to these devices yielded a resonant frequency of

6.34 MHz for the films and a damping ratio (ζ) of 0.118, indicating underdamped nature of the PVDF pressure sensor film.

The logarithmic decrement (δ = 2.652) was calculated from the recovery time of the PVDF devices in Figure 6.14 and the damping ratio (ζ) of the devices was calculated using the following equation:

$$\zeta = \frac{\delta}{\sqrt{(2\pi)^2+\delta^2}}$$

When two electrode devices were connected, the top two electrodes were connected to independent channels and the bottom electrode acted as the common ground electrode. Output from such a device is shown in Figure 6.15. The plot shows the output obtained from the devices after charge amplification, in mV and the corresponding ambient pressure in mmHg. The PVDF sensors performed at a sensitivity of 99μV/mmHg.

The testing of the fabricated PVDF sensors show good performance compared to the ambient pressures in the chamber. From Figure 6.15a we observe that the travelling average has a noisy nature, which is due to the absence of baseline subtraction. The maximum frequency shown in Figure 6.15b is 3Hz, which also happens to be the range for normal physiological frequencies. Therefore, the PVDF pressure sensor is capable of resolving physiological pressure variations even in miniature flexible version. Thus the output from the PVDF pressure sensor is uniform through the operational frequencies. In other words, there is minimal drift observed for the PVDF sensors.

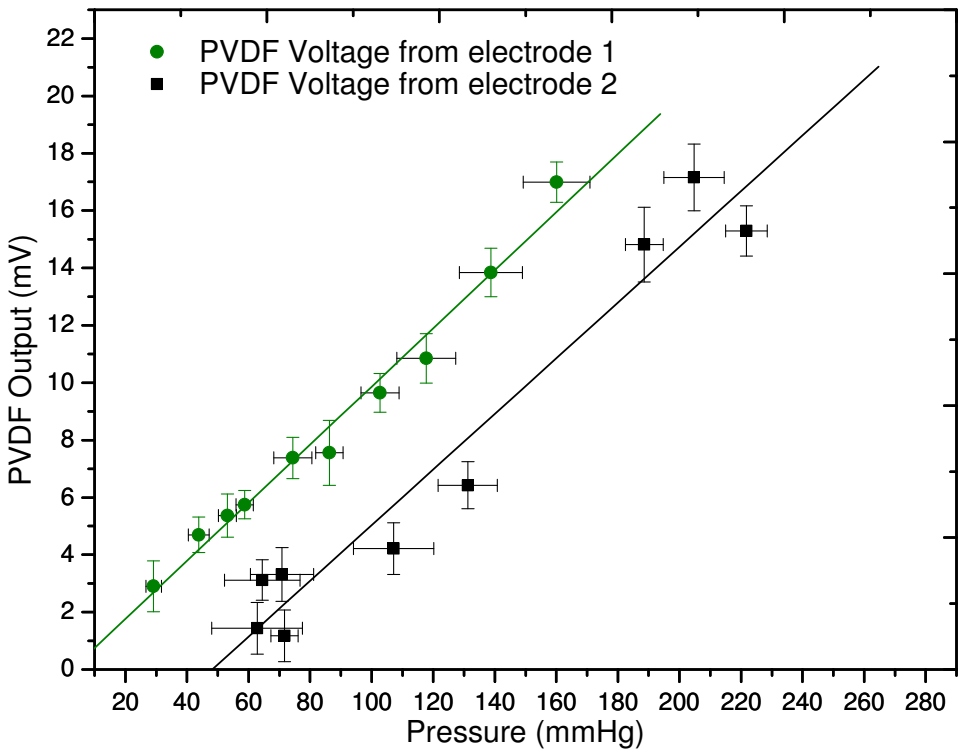

Figure 6.15 The flexible-PVDF sensor response versus the chamber pressure for two independent top electrodes. Slope of the graphs indicate reliable performance from the two electrodes with different zero errors and a high sensitivity of 99μV/mmHg

The dual top electrode based PVDF sensors show a good linear response even with very low functional surface area. Larger devices have show more reliable reproduction of pressure measurements [91]. Since the ambient chamber pressure was measured using a commercial pressure sensor, the data obtained from the commercial pressure sensor was in voltage as well. Using the custom-calibrated equation, this data

was used to determine the ambient chamber pressures. Since the commercial pressure sensors perform in a similar manner compared to our PVDF sensors (Figure 6.15), we could also calculate the error in measurement using the commercial sensors from the acquired data. This error from the commercial pressure sensor is plotted on the chart as the x-axis error. A quick comparison of the error bars of PVDF sensors versus the commercial pressure sensor indicates that the performance of the PVDF sensors is as reliable as the commercial pressure sensors used in the present study. Further, the sensitivity of the PVDF pressure sensor was found to be 99μV/mmHg, nearly four times higher than the commercial pressure sensor used in the present study (25.3μV/mmHg).

6.5.3 Water based testing

In order to simulate physiological conditions for testing, it was important to replace air based testing process with water based testing environment. We replaced the air source with a constant source of water by the use of a peristaltic pump. By keeping the entire setup the same, we could manipulate the water pressure inside the flow chamber either manually using the multivalve or using the solenoid valve. In order to protect the devices from getting damaged by water, the entire device surface was spin coated by a thin film of ultra-low viscosity UV-curable epoxy (Norland optics). The UV epoxy was spin coated on top of the device surface at 2000rpm for 30s. This resulted in a 10μm or thinner layer of UV epoxy formation on top of the device. The resulting film was flexible and did not affect the PVDF sensor significantly, as shown by Figure 6.16 and Figure 6.17.

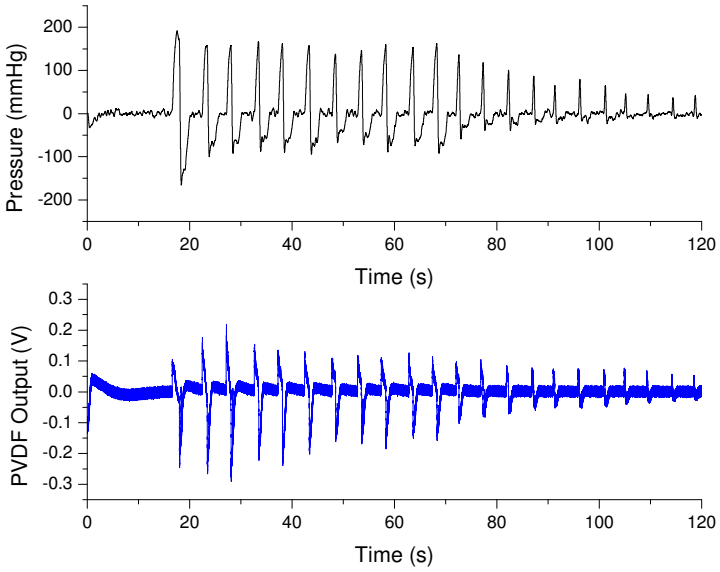

Figure 6.16 Plot showing comparison of water based testing results in flow chamber between commercial pressure sensor (top) and PVDF sensor (bottom)

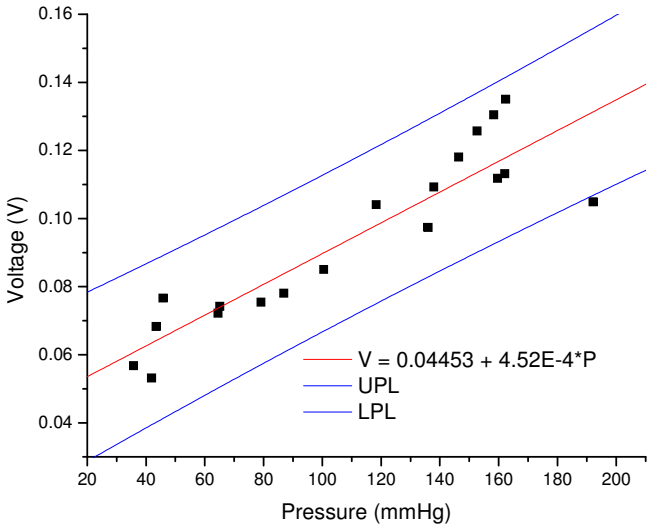

Figure 6.17 Plot showing PVDF sensor output as a function of the chamber water pressure

Although, Figure 6.17 shows low sensitivity obtained from a sensor tested in water chamber, this was not true for most other sensors tested in the water chamber, as can be seen from Figure 6.16. Moreover, water chamber testing of thin film devices were done mainly to study the effect of exposing devices to water based environment and optimize sensor packaging for catheter based testing (described later in Chapter 6). It was found that the devices did not show any degradation or difference in the signal response when the electrode portion of the devices was not coated with UV epoxy, as long as the terminal electrode pads (where external wiring connections are made using silver print) were sealed with UV epoxy.

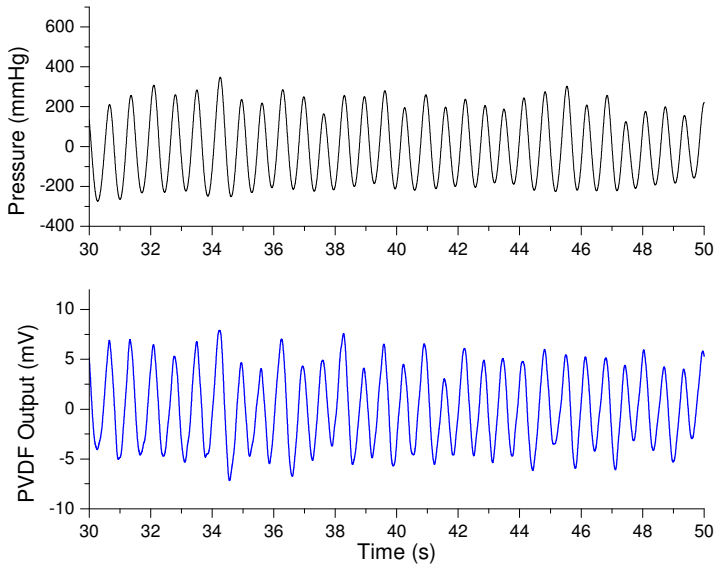

Figure 6.18 Water chamber testing of randomly oriented nanofibers based device

We also performed preliminary water based testing for electrospun fiber based devices. Figure 6.18 shows good peak-to-peak corroboration between the device output from a randomly oriented electrospun sample against the ambient chamber pressures.

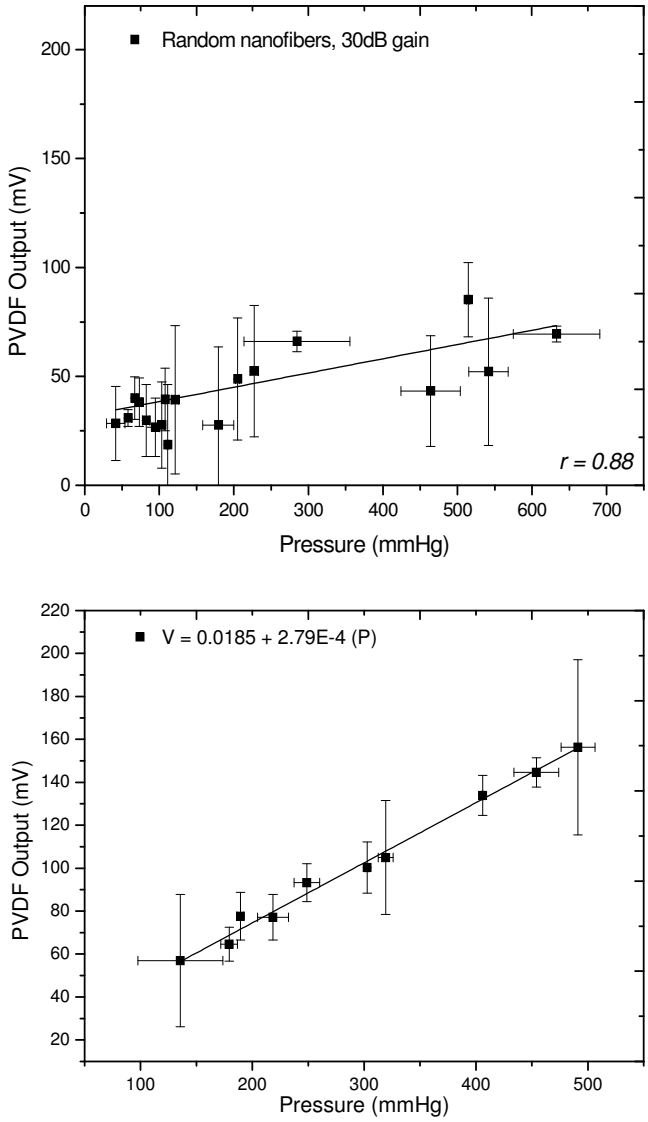

Figure 6.19 Plots comparing the sensitivity of randomly oriented nanofibers based device (top) against the aligned nanofiber based devices (bottom), both graphs at 30dB

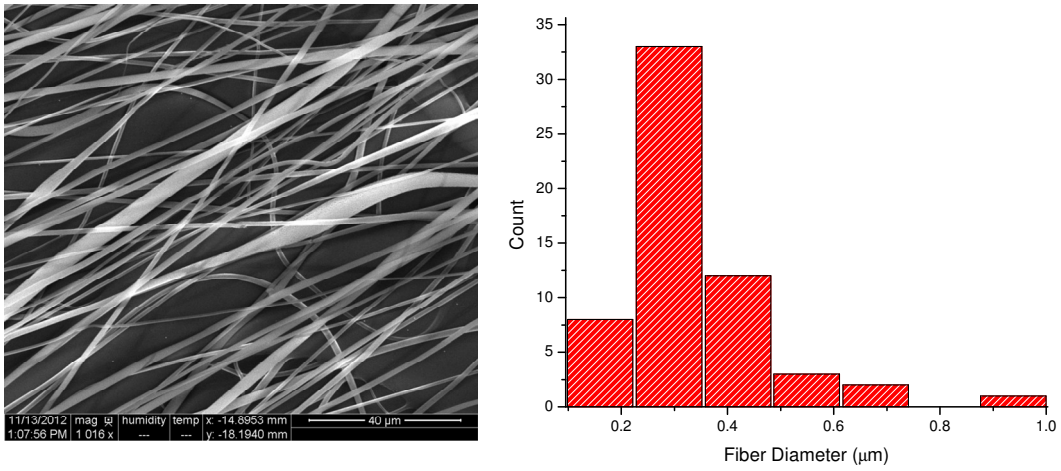

Figure 6.20 Figures showing SEM image of the aligned nanofiber sample along with the fiber diameter distribution in the sample. The average fiber diameter was found out to be 1.469 ± 0.654 µm

Figure 6.19 compares the performance of random nanofiber based devices alongside the performance of aligned nanofiber based devices. Both the sensitivity plots show the device performance at 30dB. From the sensitivity plots, we notice that aligned nanofiber based devices show higher sensitivity (280µV/mmHg) compared to the random nanofiber based devices (65µV/mmHg), assuming 30dB of amplification at the charge amplifier. Further, the aligned nanofiber based devices showed higher linearity, indicated by the higher residual sum of squares value. Fiber characteristics described in Figure 6.20 are indicative of good aligned fiber patterning as indicated previously (Figure 4.30).

The same highly aligned nanofiber based devices did not perform as well on poling, however. Figure 6.21 shows the decreased sensitivity and increased error in the device performance after poling of nanofibers.

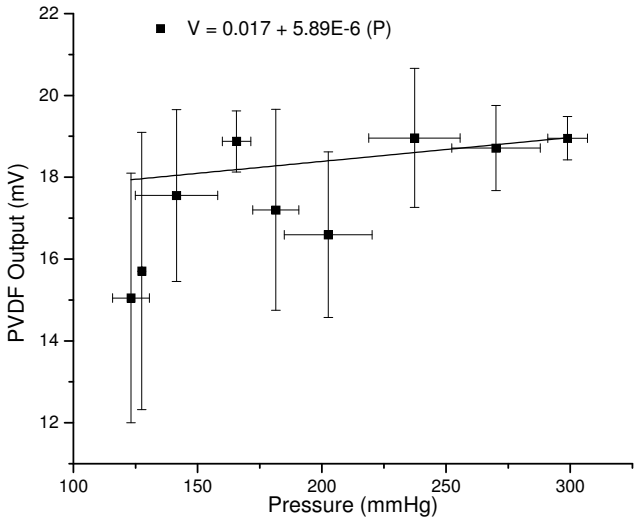

Figure 6.21 Sensitivity plot of aligned PVDF nanofiber based devices after poling of devices at 3kV for 30 minutes, showing decrease in the device performance

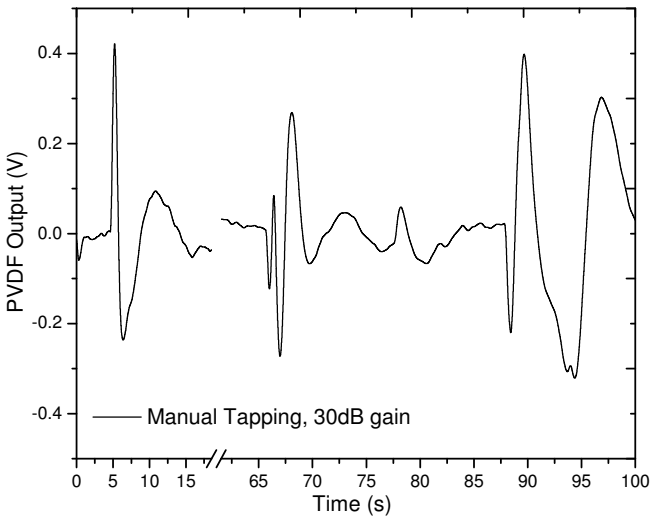

Figure 6.22 Plot showing reversal of polarization obtained by swapping of terminal electrode connections, indicative of piezoelectric phenomenon

The devices showed a reversal in polarization obtained from the two electrodes upon swapping of the electrode connections (Figure 6.22). This is a good indication that the signal being obtained is from the piezoelectric nature of the aligned nanofibers and not due to external electrostatic residual charges.

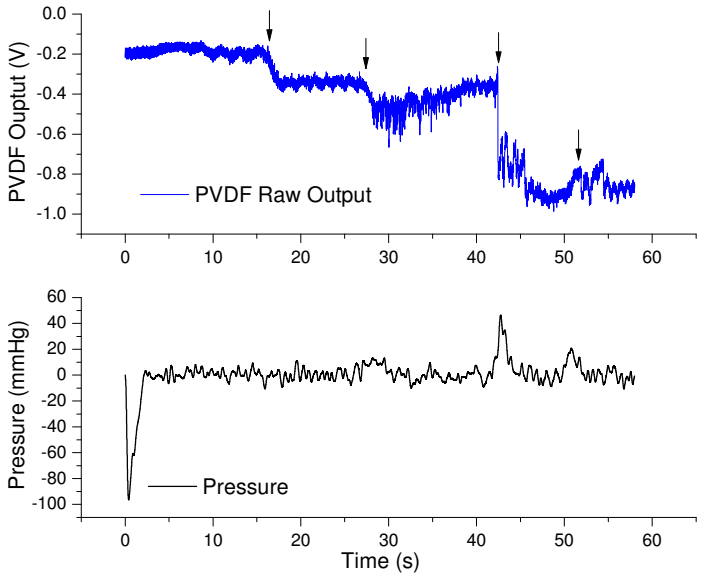

Figure 6.23 Plot comparing raw data output from aligned nanofiber based PVDF devices sensitive enough to detect changes in water flow rate

The aligned nanofiber based devices showed higher sensitivity (280μV/mmHg, scaled to 40dB) compared to the thin film based devices (99μV/mmHg) while at the same time using only half the piezoelectric material (estimated from the average fiber diameter and surface fiber density). This high sensitivity was also capable of detecting minor fluctuations in the flow rates (Figure 6.23), where the commercial pressure sensor failed to show any minor pressure variations.

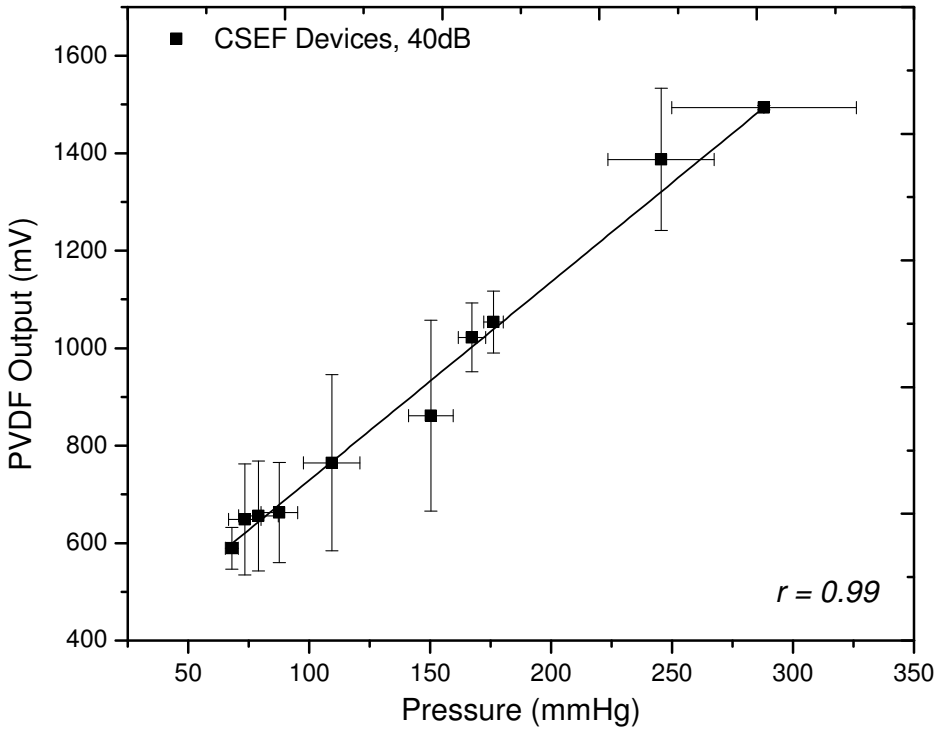

Figure 6.24 Plot of core-shell electrospun fibers based pressure sensing devices, scaled to 40dB for comparison with previous sensors

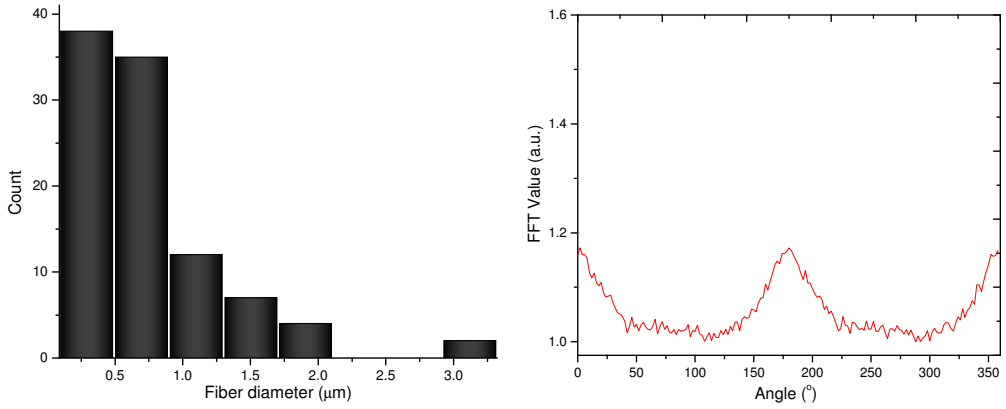

Figure 6.25 Plot showing core-shell fiber distribution (average diameter 0.951 ± 0.0.284 μm), along with the FFT plot showing alignment of the electrospun fibers

Figure 6.24 shows the enhanced performance of core-shell electrospun fiber based devices plotted at 40dB. The core-shell based devices showed high sensitivity (4mV/mmHg) along with high linearity (R-value = 0.99) over the required pressure range of 0-300mmHg. From Figure 6.25, we notice the aligned nature of core-shell electrospun fibers on a rotating drum assembly with average fiber diameters being around 1µm.

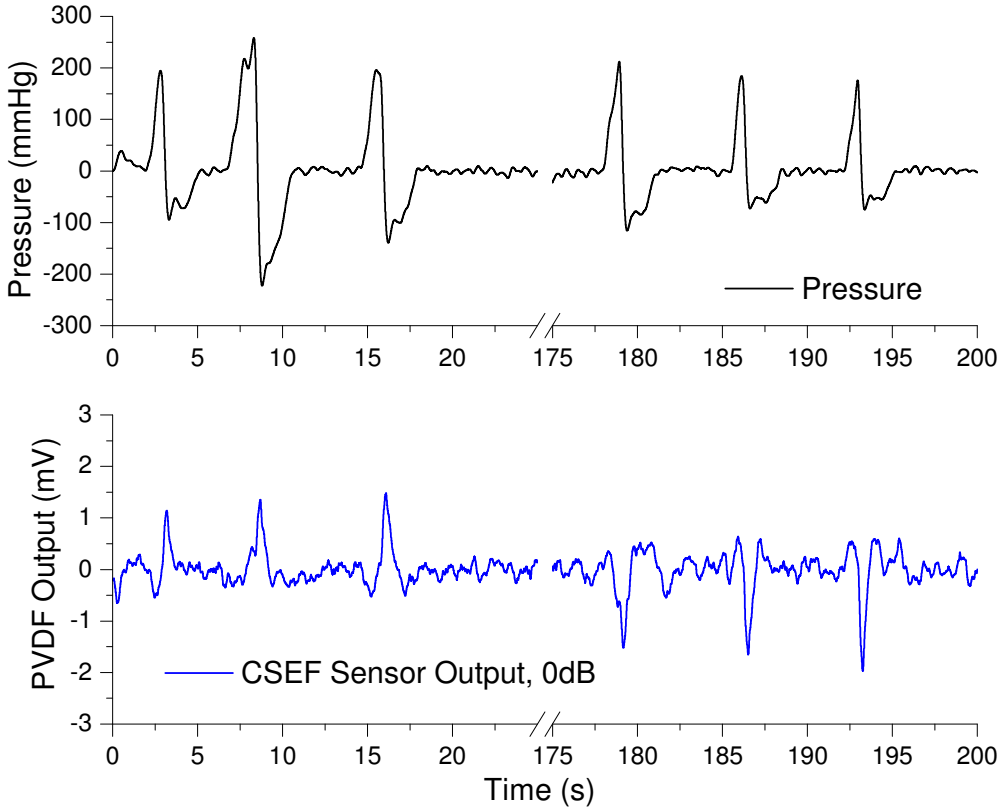

Figure 6.26 Plot showing reversal in polarity from another CSEF based devices on electrode swapping, a strong indicator of piezoelectric signal

The core-shell based devices showed good performance that was 4.5 times higher than the aligned nanofiber based devices (Figure 6.27) than the nanofiber based devices. Further, Figure 6.27 summarizes the performance comparison of the various transducer designs fabricated in the present study. We clearly see 8.8 times higher signal output from nanofiber based devices than from the thin-film based devices, which in the same range of electromechanical efficiency enhancement as reported previously for nanofibers versus thin-film based devices [71].

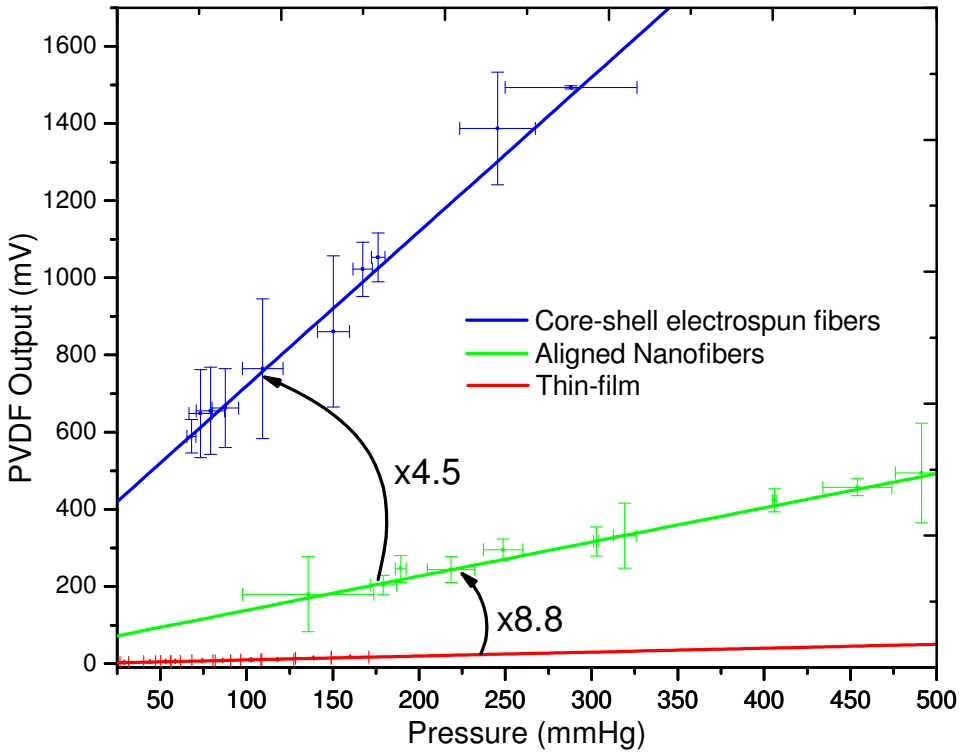

Figure 6.27 Plot comparing the sensitivity of various sensors fabricated in the present study

6.5.4 Tubing based testing

Before the actual mounting of any pressure sensor on the curved surfaces of a catheter, it was important to check for the functioning of PVDF sensors on soft material based tubing. Figure 6.28 shows the photograph of such a modified chamber with 5mm diameter polyurethane tubing fixed inside the chamber.

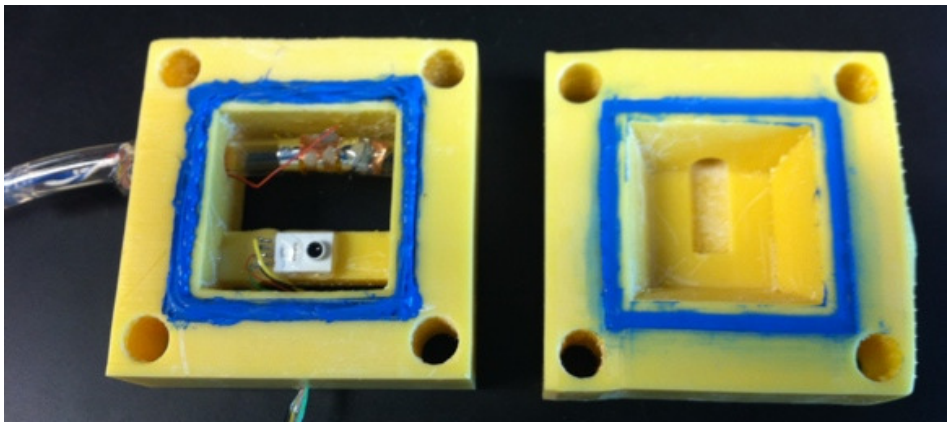

Figure 6.28 Photograph of the flow chamber modified to hold a flexible tubing with a PVDF sensor mounted on the external wall of the tubing

The tubing was inserted through a custom made hole on the side wall of the middle plate of the testing chamber. The flexible PVDF sensor was mounted on the curved surface of this tubing in a manner that the sensor and the commercial pressure sensor were on the same level. Electrical wirings to the PVDF sensor was passed through a hole punctured in the tubing itself. All holes, gaps and electrode pads were sealed using UV epoxy. Water was then flown in a controlled manner through the chamber for testing the PVDF sensor.

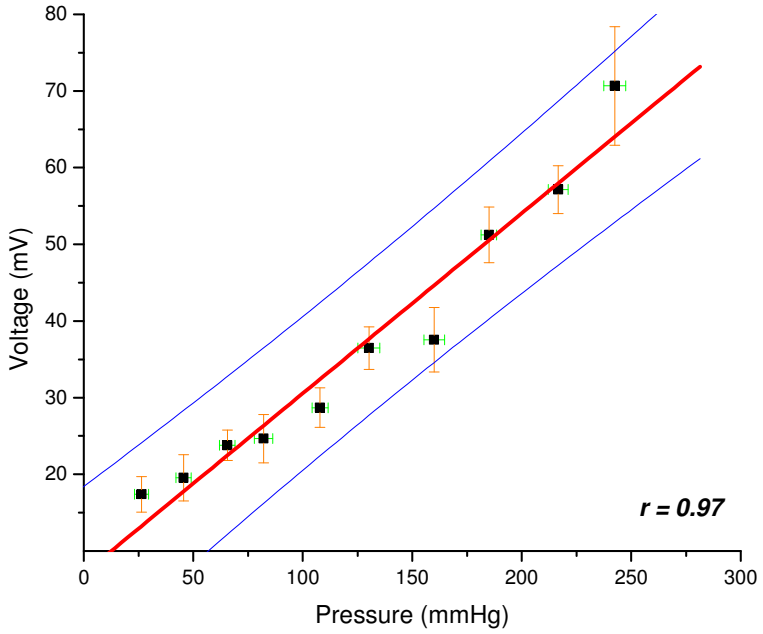

Figure 6.29 Signal output from a single top electrode PVDF thin-film based device ($2x2mm^2$)

Figure 6.29 shows the signal output obtained from a single top electrode device ($2x2mm^2$) mounted on the tubing inside flow chamber. The data was normalized to 40dB in the present plot. We see good linear response from the fabricated PVDF sensor even under water testing on flexible tubing. Further, a quick comparison between Figure 6.29 and Figure 6.15 reveals that we observe twice the sensitivity from the single top electrode device (Figure 6.29) than from the double top electrode device (Figure 6.15). This is obvious due to the double surface area of the single top electrode device accumulates twice the amount of charge compared to a single electrode of a dual-top-electrode

patterned device. This is further evidence that the PVDF sensors fabricated in the present study gave reliable and consistent output.

6.6 VASCULAR TESTING MODEL

In order to test the PVDF sensors in close to physiological environment, we built a vascular testing model in which we could control the water pressure. The water pressure was measured simultaneously by a commercial pressure sensor alongside the PVDF sensor. While the commercial pressure sensor was fixed in the rigid housing, the PVDF sensor was mounted on the tip of the catheter.

6.6.1 Catheter setup

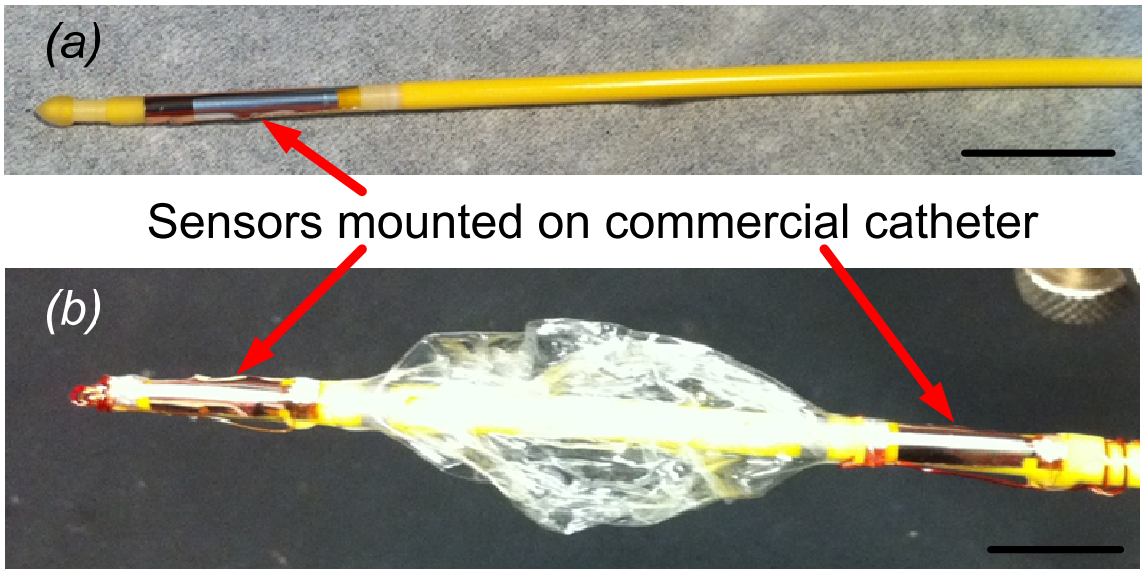

Figure 6.30 (a),(b): Photographs showing PVDF pressure sensors mounted on catheter, on either side of balloon. Scale bars: 1cm.

For catheter assembly, commercial aortic occlusion catheter was used for testing (10Fr gauge, Coda Aortic Catheter, Cook Medical, Bloomington, IN). Pair of 40 gauge insulated magnetic wires was used to make connections to the device electrode pad. The electrical wires were wrapped around the catheter surface or passed through the internal lumen space of the catheter (Figure 6.30 and Figure 6.31). The electrical connection was made using silver print. The whole joint was insulated using UV curable epoxy.

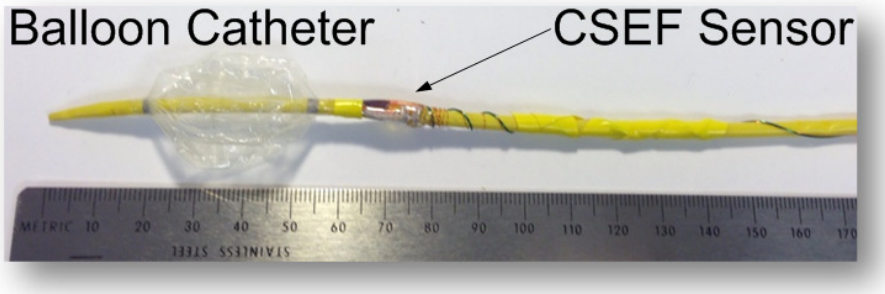

Figure 6.31 Photograph showing a core-shell electrospun fiber based sensor mounted on the catheter

6.6.2 Vascular testing setup

To simulate physiological blood flow, a 3D model of the aorta and lower arteries was fabricated using a laser sintering machine (Sinterstation HiQ, 3D Systems, Rock Hill, SC). The model was created by extracting the vascular structures from contrast-enhanced computed tomography (CT) scan data from an average sized male patient. The walls were made slightly thicker than normal in order to stabilize the structure. Barbed tubing connectors were fixed to the terminal ends of this 3D model with one of the

segment connected to a 0.5” tubing to act as the catheter insertion port (Figure 6.32). Through-wall holes were drilled in the same segment holding the catheter for placement of the same commercial sensors (mentioned above). The commercial sensors were sealed in place using epoxy in a way such that the transducer element was open to the fluid flowing inside the arterial segments.

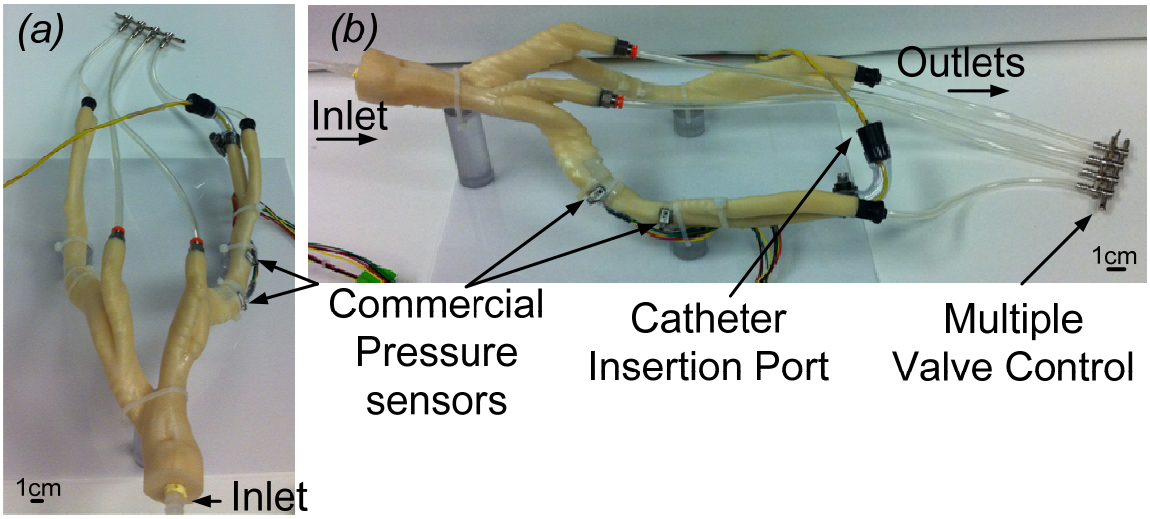

Figure 6.32 Vascular testing model with integrated sensor.

6.6.3 Device Testing

For water based testing in the vascular testing model, the assembled catheters were inserted through the port up to a distance such that the PVDF sensors were in proximity of the commercial sensors in the same segment. The inserted catheter was locked in place using butyl rubber cork which with custom drilled bore size and made water-tight using hot-glue.

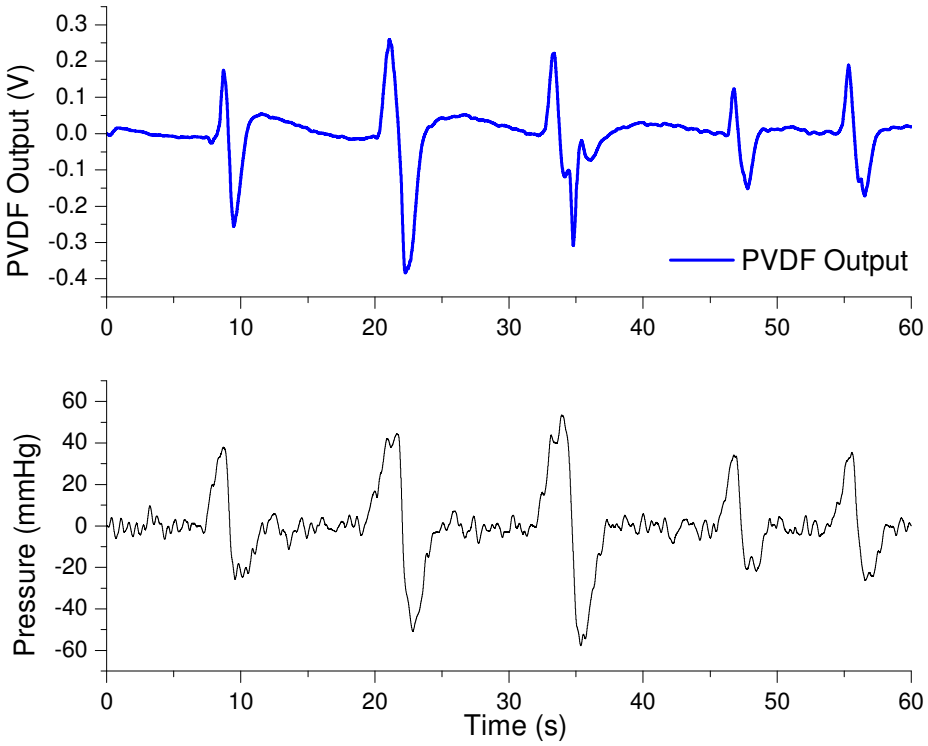

Figure 6.33 Real-time signal from a catheter-mounted PVDF sensor versus the commercial sensor (on vascular testing model pressure) located in close proximity to the PVDF sensor

Water was injected into the completely assembled vascular testing model with the help of a peristaltic pump. The catheter port segment was first kept unsealed to allow escape of air. The water pressure and flow rate in the various segments was controlled using a multi-flow valve. The fluid pressure inside the vascular testing model was controlled manually by manipulating the fluid flow rate and the time for which the valve

was closed and simultaneous signals were recorded from both the PVDF devices and the commercial pressure sensors.

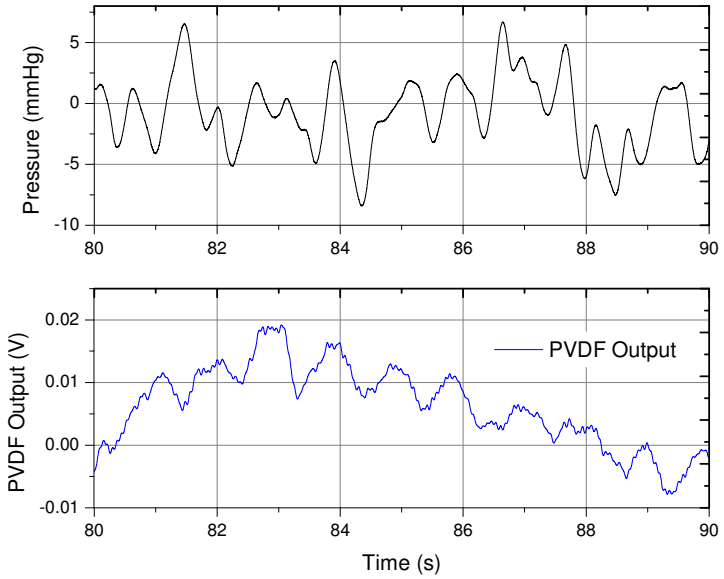

Figure 6.34 Plot showing highly sensitive PVDF sensors capable of detecting low intensity fluctuations in water pressures inside the chamber due to the peristaltic pump, where the commercial pressure sensor failed to detect any pressure fluctuations

The signal output from the sensors is shown in Figure 6.33 and Figure 6.34. From the plot, we see a good correspondence from PVDF devices under wet conditions as well. Further, the signal to noise ratio is higher from PVDF devices compared to the commercial sensor. Figure 6.34 shows the high quality signal obtained from PVDF sensors, which as capable of detecting the minor fluctuations in vascular testing model due to the peristaltic pump. Similar results were obtained from dual sensors mounted on a catheter and tested in the 3D vascular model.

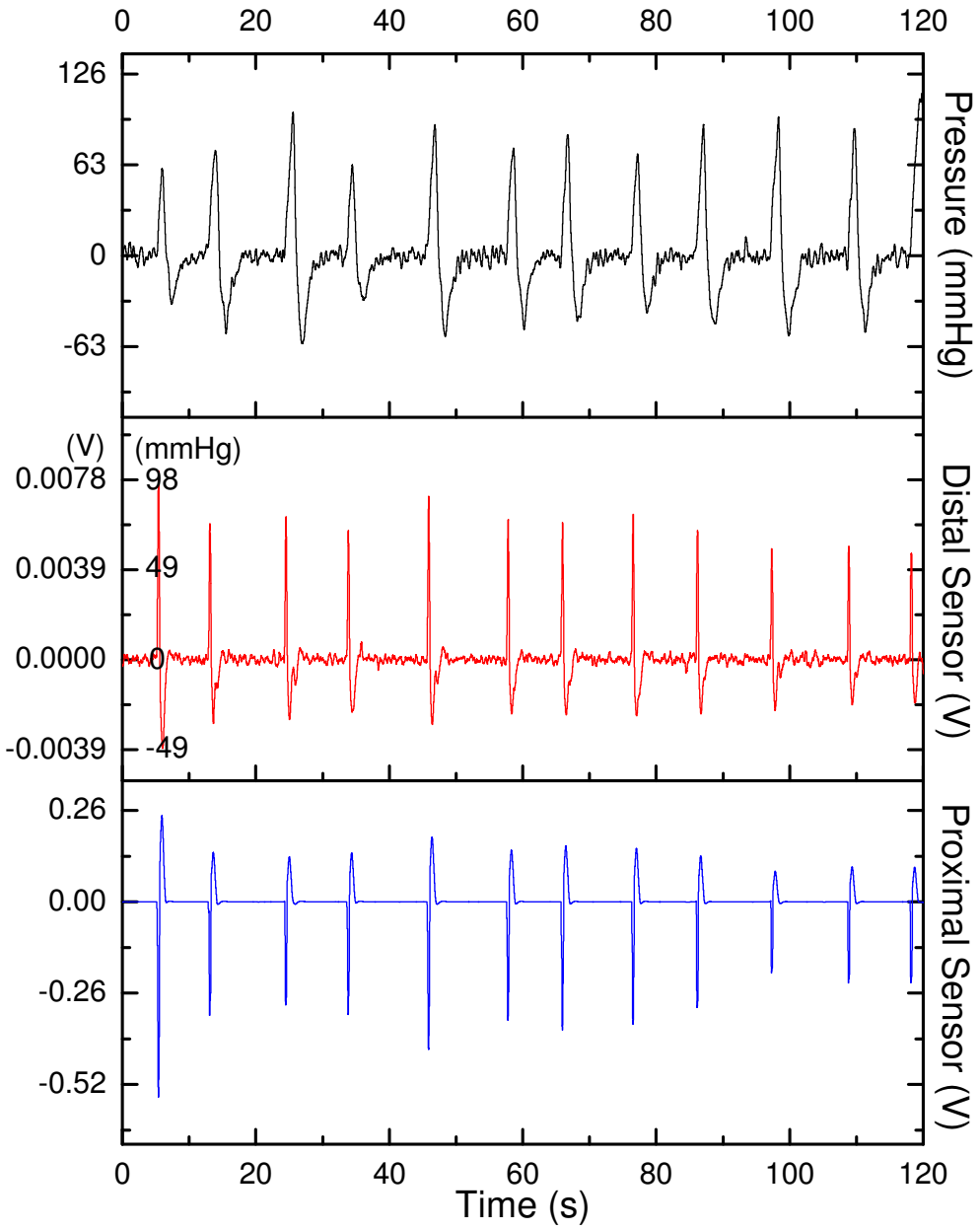

Figure 6.35 Comparison of the proximal (closer to catheter tip) and distal (away from catheter tip) PVDF sensors against the fluid-pressure inside the vascular model. It shows shorter response times of PVDF sensors (0.26s) compared to the commercial pressure sensor (1.30s).

Figure 6.35 shows good correlation of the signal output with the ambient pressure from the two PVDF sensors mounted on either side of a balloon. Further, there is negligible delay in the signal received when the balloon is deflated. The average response time of the PVDF sensors (0.26s) was found to be five times higher than the commercial pressure sensor (1.30s) when evaluated for the 0% to 100% pressure change. When the balloon is inflated, pressure is recorded from the proximal PVDF sensor only, as expected (data not shown). Again, the commercial pressure sensors in the present case show a lot of noise compared to the high quality signal from PVDF sensors.

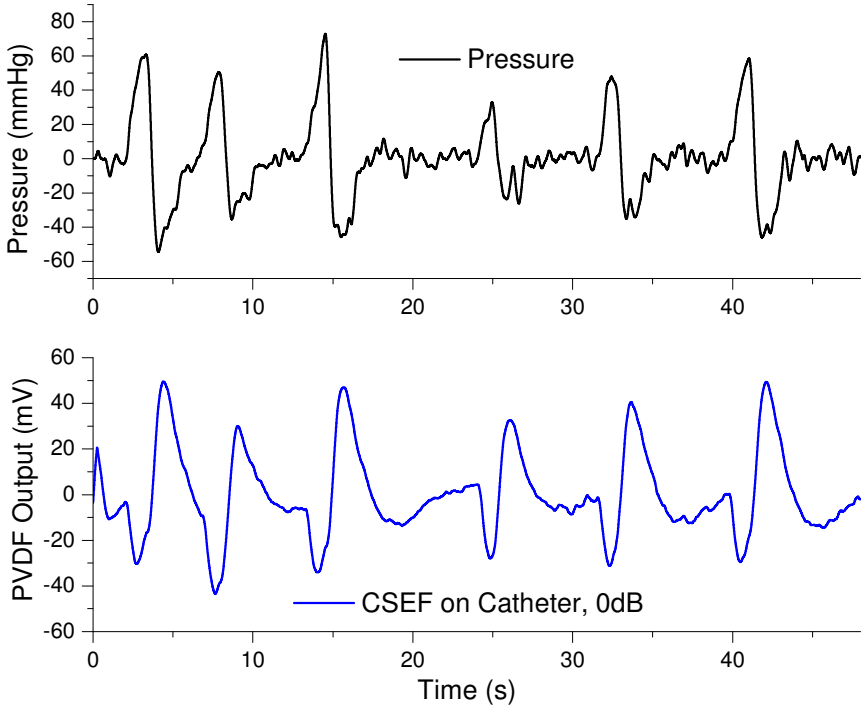

Figure 6.36 Plot showing performance of a CSEF device mounted on catheter surface compared against the commercial pressure sensor

Figure 6.36 shows a comparison between the commercial pressure sensor and high quality response obtained from the core-shell electrospun fiber based sensors that were mounted on a catheter. Further, this signal showed good correlation and reflection of the water pressures inside the vascular testing chamber without any amplification on the charge amplifier. Figure 6.37 shows the same device response obtained when the balloon was inflated and deflated.

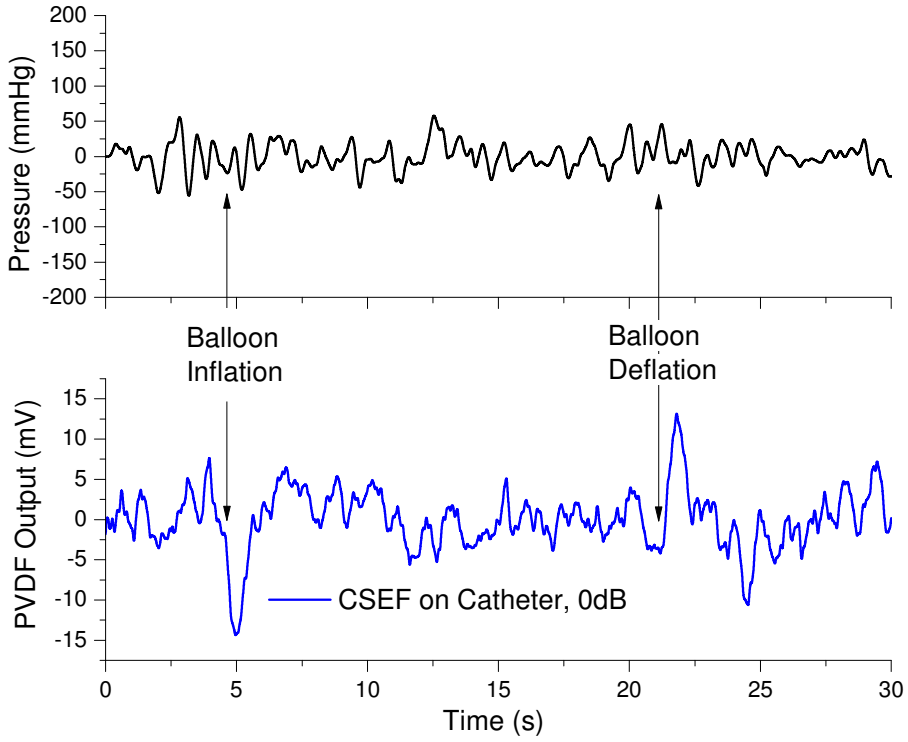

Figure 6.37 Plot showing the response obtained from core-shell electrospun fiber based sensors on catheters upon inflation and subsequent deflation of a balloon on catheter, compared against no signal received from the commercial pressure sensor

Only the CSEF based sensor was capable of detecting the pressure variations due to the changes in balloon condition and any change in the system went unnoticed by the commercial pressure sensor.

6.7 SUMMARY

The low-cost, low-temperature standard lithography fabrication technique is applicable to pattern biocompatible PVDF-TrFE copolymer. The process is fully compatible with existing micromachining fabrication processes without additional mechanical stretching and electrical poling processes. Further, we found that the electrode-patterned surface area only contributes towards the output signal rather than the PVDF area. We achieved better β-phase formation in thin film (1 μm) PVDF-TrFE copolymer compared to the thick film (6 μm) without any electrical poling or mechanical stretching. The demonstrated fast recovery time (0.17 sec), biocompatibility, and compact form factor show the great potential for pressure and flow direction measurements as implantable biomedical devices.

We further fabricated devices and tested them in water based testing environment, both on a hard wall surface and on soft-material tubing. From both the testing environments, we observed good device response. Water based testing was extended to custom-build vascular testing model. For vascular based testing, PVDF sensors were successfully mounted on the surface of the catheter. The catheters were inserted inside the vascular testing model and by manipulating the flow of water inside the model, we observed high quality signal obtained from PVDF devices compared to the existing commercial pressure sensors. The PVDF devices fabricated in the present study showed

higher sensitivity and shorter response time, both of which are highly desirable for the intended biomedical applications.

For the future prototype ready for catheter based *in-vivo* measurements multi-lumen catheters will be used for multiple sensor integration onto a single catheter. In such an assembly, the electrical wirings will be internally present and will not be exposed or affected by blood flow or bodily fluids. Although we passivated the sensors in the present study using UV epoxy, the devices can be readily laminated using thin coating of parylene, which has been shown to be biocompatible previously [132].

Chapter 7: Conclusions and Future Work

7.1 CONCLUSIONS

In the present thesis we have demonstrated the capability of using various PVDF structures and fabricate highly sensitive, flexible pressure sensors out of them. Such flexible pressures sensors are highly important for various biomedical applications, especially since they can be easily integrated with catheters for minimally invasive surgeries.

We demonstrated the technique for fabrication of uniform thin film structures using PVDF-TrFE solution. The film was shown to have high cyrstallinity, comparable to commercial films, without any mechanical stretching or poling. We also demonstrated that 1µm thin film was more piezoelectric nature compared to the 6µm thick film. This was supported by the differential scanning calorimetry experiments and also by the fabricated sensor performance. We successfully assembled the electrospinning facility and optimized all the different variables involved in the electrospinning of PVDF nanofibers. Further, we optimized the ground collecting electrode geometry for patterning high-density of highly aligned nanofibers. Quantification of the highly aligned nanofibers was performed on the obtained samples using ImageJ. This technique helped us distinguish between the aligned nanofiber and the randomly oriented nanofibers. More importantly, the results of quantification revealed that higher rotating drum speeds lead to better alignment of the fibers. This high rotation speeds coupled along with the parallel ground wires on the rotating drum was the missing link towards achieving high-density of highly aligned nanofibers.

We also demonstrated the electrospinning of core-shell fibers. Several variables were optimized to obtain the desirable highly aligned core-shell fibers. Further, the resistance of the core material was decreased substantially by using PEDOT:PSS based polymer solution. PVP was added to the core solution to add viscosity to the solution. TEM images along with the presented confocal laser fluorescence imaging indicated substantial presence of core-shell fibers in large quantities. The fabrication of the conductive core-polymer and the optimization of core-shell electrospinning conditions opens up the possibilities for creating nanostructure based biosensing systems that are robust and compact for therapeutics, NEMS, MEMS and micro-total analysis systems.

We demonstrated the procedure for integration of the thin film, highly aligned nanofibers and core-shell fiber structures into device format. Devices were successful fabricated employing the various structures described in the present study. We also optimized various device geometries to optimize the signal quality. Thin-film based PVDF sensors showed faster recovery times and higher sensitivity, even compared to the commercial pressure sensor (intended for biomedical application). This indicates the need and efficacy of PVDF pressure sensors. We also tested these sensors in water based environment and in vascular testing model. We further demonstrated that the flexible sensors can be easily mounted on the curved surfaces of a catheter and still maintain all the performance characteristics of the sensor.

We also demonstrated the feasibility of using nanofiber based pressure sensors in the present study. Further, core-shell electrospun fiber based pressure sensors show a promising future in biomedical application.

The presented research concerns broadly with the understanding, manipulation and application of nanostructures towards bioenergy harvesting and sensing technologies. The technology developed here incorporates efforts in advanced materials characterization, micro- and nanofabrication, MEMS, device assembly, packaging, characterization and testing. The technology developed here has several potential applications (Figure 7.1).

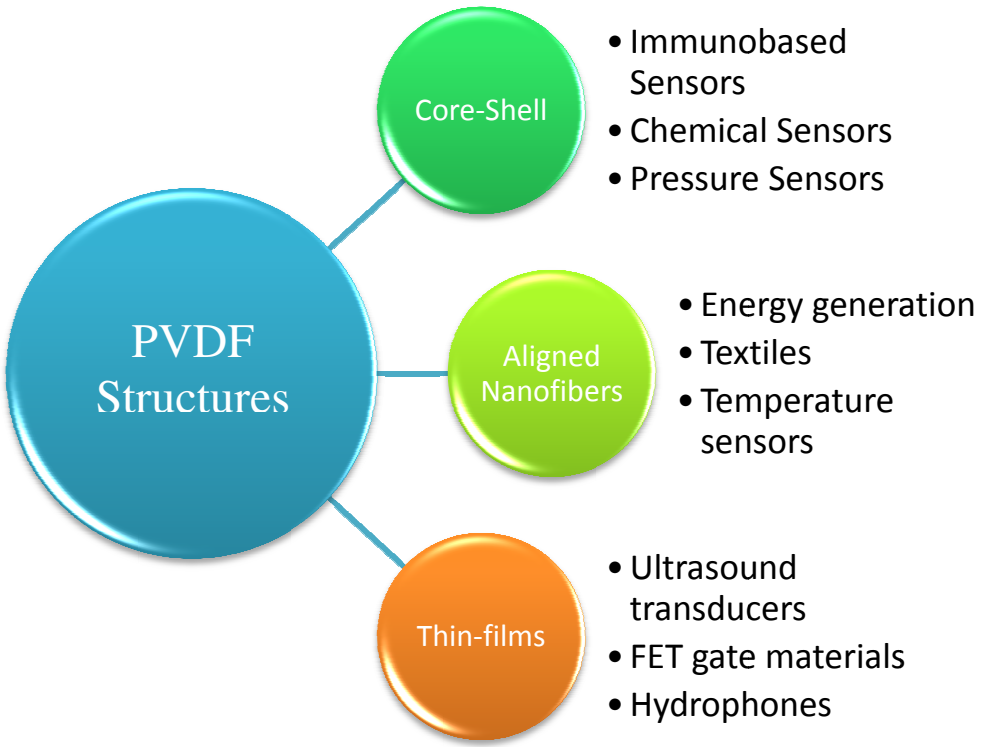

Figure 7.1 Realization of possibilities with fundamental PVDF structures

7.2 FUTURE WORK

7.2.1 Point of care systems in Biomedical Engineering

The experimental results of this dissertation provide several key insights into the future directions that this research can move forward. Even though piezoelectricity of PVDF was discovered several decades ago, fabrication of PVDF based nanostructures is a very recent trend. Clearly, there is a lot more that can be done on different fronts of material characterization, optimization for high-throughput fabrication, enhancement of core material, packaging, device assembly and testing. Development of highly conductive core materials, possibly by using graphene composite materials, is an exciting avenue remaining unexplored. Usage of core-shell nanofibers for electroimmuno based sensors can also be studied.

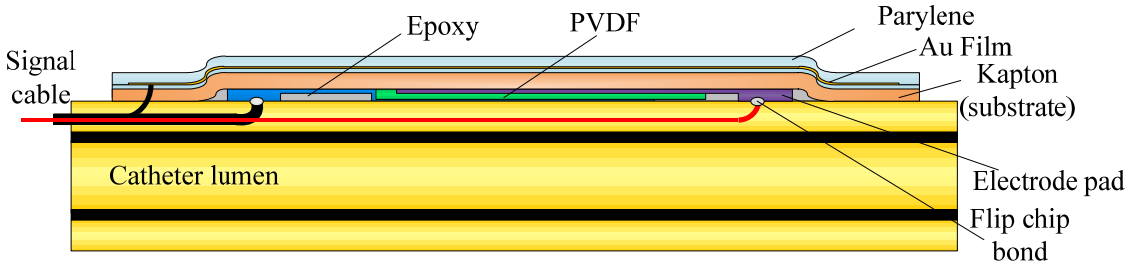

Figure 7.2 Schematic showing the final device mounted on the catheter surface using flip-chip bonding with parylene coating for passivation. An additional layer of gold film is added to eliminate electrostatic interference

Development of more robust, reliable, flexible pressure sensors for catheter application can revolutionize the field of minimally invasive surgeries. Commercial packaging of the PVDF based pressure sensors needs to be worked before clinical

application of such technology. For prevention of electrostatic interference due to ionic flow along with the blood, the devices can be coated with a sandwiched parylene-gold-parylene film (as shown in Figure 7.2) with the gold layer grounded. Combining the novel nanofiber based sensing design with advance measurement techniques described above and unique packaging route, can result in highly sensitive, compact yet flexible pressure sensor appropriate for cardiovascular applications.

7.2.2 Energy

Of the possible types of electro-mechanical devices that can perform *in-vivo* energy conversion, a piezoelectric transducer that makes use of the material's electro-mechanical coupling to covert motion to energy is the most attractive owing to the potentially greater energy densities. There has been tremendous interest in piezoelectric polymer film energy scavengers that convert cardiac motion into electrical power to recharge automatic implantable cardiac defibrillators (AICD). By tuning the thin films thickness, crystallinity and surface energy states, orders-of-magnitude improvement in the power output can be achieved (Figure 7.3).

To date, there have been only a few preliminary demonstrations of energy harvesting from motion of the heart. While ZnO based brittle devices would dissolve in blood over a period of time, other materials might be highly toxic. Nonetheless, it is unclear if the power generation capabilities for either of these schemes may be suitable (there are no data in open literature) and neither approach has been reduced to practical use. The most attractive strategy will be one that does not complicate the implantation

process, compromise the patients' health, introduce additional load on the heart, and fits within the design of existing leads.

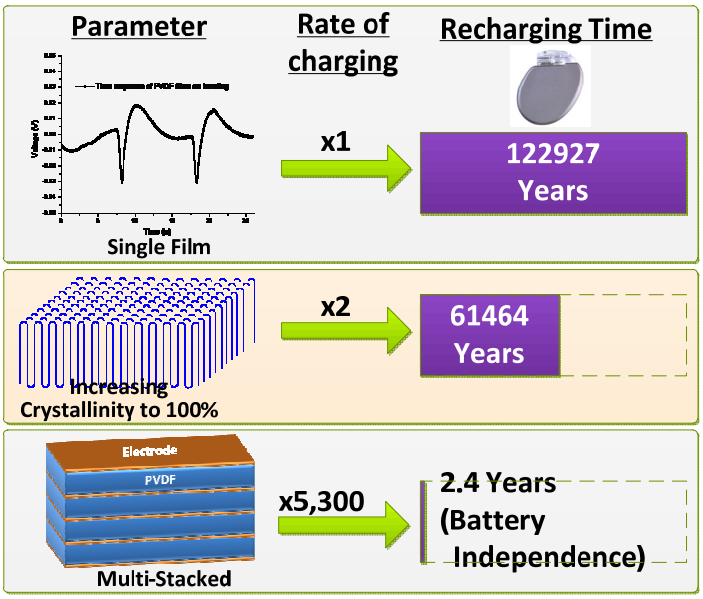

Figure 7.3 Schematic showing the recharging rates and times for an ICM (Implantable Cardiac Monitor) for increasing layers of a multi-stacked PVDF based structure

PVDF is an ideal biomaterial because it is nontoxic, inert, resistant to water absorption (absorbs < 0.04% by weight), biocompatible and clean-room friendly. There are three primary motivating factors for developing an energy harvesting device configured as a multilayered film with nanolayers of PVDF. **1.)** Piezoelectricity in polymers originates solely from crystalline domains. Recent studies [76, 77] have found that confining crystallizable polymers to ~10-100nm thickness increases crystallinity substantially **2.)** Can be easily fabricated in different shapes and patterns. Films as thin as

10nm can be fabricated from techniques like spin coating and fibers of several hundred nanometers diameter can also be drawn using electrospinning techniques, **3.)** The power transfer capability of any piezoelectric material is proportional to the surface area of the piezoelectric material. By exploiting these recent findings, combined with the novel techniques to fabricate PVDF structures presented in this dissertation, highly efficient energy scavengers can be realized.

References

1. Peng, C., K. Wen, and D. Young, *Integrated electronic system design for an implantable wireless batteryless blood pressure sensing microsystem.* Communications Magazine, IEEE, 2010. **48**(4): p. 98-104.
2. Aquilina, K., et al., *Preliminary evaluation of a novel intraparenchymal capacitive intracranial pressure monitor.* Journal of Neurosurgery, 2011. **115**(3): p. 561-569.
3. Bingger, P., et al. *Implantable multi sensor system for in vivo monitoring of cardiovascular parameters*. in *Solid-State Sensors, Actuators and Microsystems Conference, 2009. TRANSDUCERS 2009. International*. 2009.
4. Bullister, E., et al., *A Blood Pressure Sensor for Long-Term Implantation.* Artificial Organs, 2001. **25**(5): p. 376-379.
5. Nozik, A.J., *Nanoscience and Nanostructures for Photovoltaics and Solar Fuels.* Nano Letters, 2010. **10**(8): p. 2735-2741.
6. Zealley, I.A. and S. Chakraverty, *The role of interventional radiology in trauma.* BMJ, 2010. **340**.
7. Ye, X., et al., *Studies of a high-sensitive surface acoustic wave sensor for passive wireless blood pressure measurement.* Sensors and Actuators A: Physical, 2011. **169**(1): p. 74-82.
8. Research, B. *Global Markets for Catheters*. 2012; Available from: http://www.bccresearch.com/report/global-market-catheters-hlc019e.html.
9. Lewis, B.M., et al., *Clinical and physiological correlations in patients with mitral stenosis. V.* American heart journal, 1952. **43**(1): p. 2-26.
10. Kjällquist, Å., N. Lundberg, and U. Ponten, *Respiratory and cardiovascular changes during rapid spontaneous variations of ventricular fluid pressure in patients with intracranial hypertension.* Acta Neurologica Scandinavica, 1964. **40**(3): p. 291-317.
11. Lundberg, N., *Continuous recording and control of ventricular fluid pressure in neurosurgical practice.* Acta psychiatrica Scandinavica. Supplementum, 1960. **36**(149): p. 1.
12. Miller, J. and J. Pickard, *Intracranial volume/pressure studies in patients with head injury.* Injury, 1974. **5**(3): p. 265-269.
13. Wise, K.D. and J.B. Angell, *An IC piezoresistive pressure sensor for biomedical instrumentation.* Biomedical Engineering, IEEE Transactions on, 1973(2): p. 101-109.
14. Samaun, S., et al. *An IC piezoresistive pressure sensor for biomedical instrumentation*. in *Solid-State Circuits Conference. Digest of Technical Papers. 1971 IEEE International*. 1971: IEEE.
15. http://cabggroupassignment.wikispaces.com/file/view/swan_ganz_cath__jpg.gif/162779939/swan_ganz_cath__jpg.gif.

16. Dayal, S., et al., *The Effect of Nanoparticle Shape on the Photocarrier Dynamics and Photovoltaic Device Performance of Poly(3-hexylthiophene):CdSe Nanoparticle Bulk Heterojunction Solar Cells.* Advanced Functional Materials, 2010. **20**(16): p. 2629-2635.
17. Gopinath, S.P., et al., *Evaluation of a microsensor intracranial pressure transducer.* Journal of neuroscience methods, 1993. **49**(1): p. 11-15.
18. Ostrup, R.C., et al., *Continuous monitoring of intracranial pressure with a miniaturized fiberoptic device.* Journal of neurosurgery, 1987. **67**(2): p. 206-209.
19. Crutchfield, J.S., et al., *Evaluation of a fiberoptic intracranial pressure monitor.* Journal of neurosurgery, 1990. **72**(3): p. 482-487.
20. Eaton, W.P. and J.H. Smith, *Micromachined pressure sensors: review and recent developments.* Smart Materials and Structures, 1999. **6**(5): p. 530.
21. Esashi, M., et al., *Fabrication of catheter-tip and sidewall miniature pressure sensors.* Electron Devices, IEEE Transactions on, 1982. **29**(1): p. 57-63.
22. Saueracker, A.J., et al., *Intraoperative hypogastric artery embolization for life-threatening pelvic hemorrhage: a preliminary report.* The Journal of trauma, 1987. **27**(10): p. 1127.
23. Papakostidis, C., et al., *The role of arterial embolization in controlling pelvic fracture haemorrhage: a systematic review of the literature.* European Journal of Radiology, 2012. **81**(5): p. 897-904.
24. Hasenkamp, W., et al., *Polyimide/SU-8 catheter-tip MEMS gauge pressure sensor.* Biomedical Microdevices, 2012. **14**(5): p. 819-828.
25. Jeske, H.C., et al., *Management of hemorrhage in severe pelvic injuries.* The Journal of Trauma and Acute Care Surgery, 2010. **68**(2): p. 415.
26. Frevert, S., B. Dahl, and L. L nn, *Update on the roles of angiography and embolisation in pelvic fracture.* Injury, 2008. **39**(11): p. 1290-1294.
27. SØVik, E., et al., *The use of aortic occlusion balloon catheter without fluoroscopy for life-threatening post-partum haemorrhage.* Acta Anaesthesiologica Scandinavica, 2012. **56**(3): p. 388-393.
28. Swan, H., et al., *Catheterization of the heart in man with use of a flow-directed balloon-tipped catheter.* New England Journal of Medicine, 1970. **283**(9): p. 447-451.
29. Robin, E.D., *The cult of the Swan-Ganz catheter. Overuse and abuse of pulmonary flow catheters.* Annals of internal medicine, 1985. **103**(3): p. 445.
30. http://en.wikipedia.org/wiki/Pressure_sensor.
31. Goustouridis, D., P. Normand, and D. Tsoukalas, *Ultraminiature silicon capacitive pressure-sensing elements obtained by silicon fusion bonding.* Sensors and Actuators A: Physical, 1998. **68**(1-3): p. 269-274.
32. http://gtresearchnews.gatech.edu/newsrelease/cardiomems.htm.
33. Adamson, P.B., et al., *CHAMPION trial rationale and design: the long-term safety and clinical efficacy of a wireless pulmonary artery pressure monitoring system.* Journal of cardiac failure, 2011. **17**(1): p. 3-10.

34. Adamson, P.B., et al., *CardioMEMS Heart Sensor Allows Monitoring of Pressures to Improve Outcomes in NYHA Class III Heart Failure Patients (CHAMPION) Trial: Impact of Hemodynamic Guided Care on Patients With Preserved Ejection Fraction.* Journal of cardiac failure, 2010. **16**(11): p. 913-913.
35. http://josefaipulo.livejournal.com/4773.html.
36. Gieles, A. and G. Somers, *Miniature pressure transducers with a silicon diaphragm.* Philips Technical Review, 1973. **33**(1): p. 14-20.
37. Peake, E., A. Zias, and J. Egan, *Solid-state digital pressure transducer.* Electron Devices, IEEE Transactions on, 1969. **16**(10): p. 870-876.
38. Pomerantz, D.I., *Anodic bonding*. 1968, Google Patents.
39. Wallis, G. and D.I. Pomerantz, *Field Assisted Glass-Metal Sealing.* Journal of Applied Physics, 1969. **40**(10): p. 3946-3949.
40. http://www.imec.be/ScientificReport/SR2009/HTML/1213551.html.
41. Shaikh, M., S. Kodad, and B. Jinaga, *Performance analysis of piezoresistive MEMS for pressure measurement.* 2005.
42. Shimaoka, K., et al. *Micro-diaphragm pressure sensor using polysilicon sacrificial layer etch-stop technique*. in *Technical Digest: 7th Int. Conf. on Solid-State Sensors and Actuators (Transducers' 93)*. 1993.
43. Sugiyama, S., et al. *Micro-diaphragm pressure sensor*. in *Electron Devices Meeting, 1986 International*. 1986: IEEE.
44. Sugiyama, S., K. Shimaoka, and O. Tabata. *Surface micromachined micro-diaphragm pressure sensors*. in *Solid-State Sensors and Actuators, 1991. Digest of Technical Papers, TRANSDUCERS'91., 1991 International Conference on*. 1991: IEEE.
45. Burns, D.W., *Micromechanics of integrated sensors and the planar processed pressure transducer*. Vol. 1. 1988: University of Wisconsin--Madison.
46. Guckel, H. and D. Burns. *Fabrication techniques for integrated sensor microstructures*. in *Electron Devices Meeting, 1986 International*. 1986: IEEE.
47. Guckel, H., *Surface micromachined pressure transducers.* Sensors and Actuators A: Physical, 1991. **28**(2): p. 133-146.
48. *Millar Instruments: Single Sensor Cardiology Catheters*. Available from: http://www.millarinstruments.com/products/cardio/cardio_sngldual.php#SingleWith.
49. Millar.com.
50. Wagner, C., J. Frankenberger, and P.P. Deimel, *Optical pressure sensor based on a Mach-Zehnder interferometer integrated with a lateral a-Si: H pin photodiode.* Photonics Technology Letters, IEEE, 1993. **5**(10): p. 1257-1259.
51. Dziuban, J., A. Gorecka-Drzazga, and U. Lipowicz, *Silicon optical pressure sensor.* Sensors and Actuators A: Physical, 1992. **32**(1): p. 628-631.
52. Hoppe, K., L. Andersen, and S. Bouwstra. *Integrated Mach-Zehnder interferometer pressure transducer*. in *Solid-State Sensors and Actuators, 1995*

and Eurosensors IX.. Transducers' 95. The 8th International Conference on. 1995: IEEE.
53. Chan, M., S. Collins, and R. Smith, *A micromachined pressure sensor with fiber-optic interferometric readout.* Sensors and Actuators A: Physical, 1994. **43**(1): p. 196-201.
54. Katsumata, T., et al., *Micromachined 125μm diameter ultra miniature fiber-optic pressure sensor for catheter.* The transactions of the Institute of Electrical Engineers of Japan. A publication of Sensors and Micromachines Society, 2000. **120**(2): p. 58-63.
55. Wolthuis, R.A., et al., *Development of medical pressure and temperature sensors employing optical spectrum modulation.* Biomedical Engineering, IEEE Transactions on, 1991. **38**(10): p. 974-981.
56. http://www.sambasensors.com/.
57. Jiang, G., *Design challenges of implantable pressure monitoring system.* Frontiers in neuroscience, 2010. **4**: p. 2.
58. http://en.wikipedia.org/wiki/Piezoelectricity.
59. Akiba, T., et al., *ELECTRICITY PRODUCTION FROM ALKALOPHILIC ORGANISMS.* Biotechnology Letters, 1987. **9**(9): p. 611-616.
60. Birry, L., et al., *Application of iron-based cathode catalysts in a microbial fuel cell.* Electrochimica Acta, 2011. **56**(3): p. 1505-1511.
61. Pant, D., et al., *A review of the substrates used in microbial fuel cells (MFCs) for sustainable energy production.* Bioresource Technology, 2010. **101**(6): p. 1533-1543.
62. Logan, B.E., *Exoelectrogenic bacteria that power microbial fuel cells.* Nat Rev Micro, 2009. **7**(5): p. 375-381.
63. Sim, W., G. Kim, and S. Yang, *Fabrication of micro power source (MPS) using a micro direct methanol fuel cell (mDMFC) for the medical application*, in *The 14th IEEE international conference on micro electro mechanical systems*. 2001. p. 341-44.
64. Nalwa, H.S., *Ferroelectric Polymers: Chemistry.* Physics, and Applications (Marcel Dekker, New York, 1995), 1995.
65. Wang, H.-Y., et al., *Micro-sized microbial fuel cell: A mini-review*. Bioresource Technology, 2011. **102**(1): p. 235-243.
66. Chunyan, L., et al., *Flexible Dome and Bump Shape Piezoelectric Tactile Sensors Using PVDF-TrFE Copolymer.* Journal of Microelectromechanical Systems, 2008. **17**(2): p. 334-341.
67. Robert, M., et al., *Fabrication of focused poly (vinylidene fluoride-trifluoroethylene) P (VDF-TrFE) copolymer 40–50 MHz ultrasound transducers on curved surfaces.* Journal of Applied Physics, 2004. **96**(1): p. 252-256.
68. Li, C., et al., *Flexible dome and bump shape piezoelectric tactile sensors using PVDF-TrFE copolymer.* Microelectromechanical Systems, Journal of, 2008. **17**(2): p. 334-341.

69. Li, C., et al., *Dual-mode operation of flexible piezoelectric polymer diaphragm for intracranial pressure measurement.* Applied Physics Letters, 2010. **96**(5): p. 053502-053502-3.
70. Kärki, S. and J. Lekkala, *A new method to measure heart rate with EMFi and PVDF materials.* Journal of Medical Engineering & Technology, 2009. **33**(7): p. 551-558.
71. Chang, C.E., et al., *Direct-Write Piezoelectric Polymeric Nanogenerator with High Energy Conversion Efficiency.* Nano Letters, 2010. **10**(2): p. 726-731.
72. Chang, J. and L. Lin. *Large array electrospun PVDF nanogenerators on a flexible substrate*. in *Solid-State Sensors, Actuators and Microsystems Conference (TRANSDUCERS), 2011 16th International*. 2011: IEEE.
73. Katta, P., et al., *Continuous electrospinning of aligned polymer nanofibers onto a wire drum collector.* Nano Letters, 2004. **4**(11): p. 2215-2218.
74. Li, D., Y. Wang, and Y. Xia, *Electrospinning Nanofibers as Uniaxially Aligned Arrays and Layer-by-Layer Stacked Films.* Advanced Materials, 2004. **16**(4): p. 361-366.
75. Li, D., Y. Wang, and Y. Xia, *Electrospinning of Polymeric and Ceramic Nanofibers as Uniaxially Aligned Arrays.* Nano Letters, 2003. **3**(8): p. 1167-1171.
76. Ericson, M.N., et al. *In vivo application of a minimally invasive oximetry based perfusion sensor*. in *Engineering in Medicine and Biology, 2002. 24th Annual Conference and the Annual Fall Meeting of the Biomedical Engineering Society EMBS/BMES Conference, 2002. Proceedings of the Second Joint*. 2002.
77. Clausen, I., et al. *A miniaturized pressure sensor with inherent biofouling protection designed for in vivo applications*. in *Engineering in Medicine and Biology Society,EMBC, 2011 Annual International Conference of the IEEE*. 2011.
78. Prakash, G., et al., *High efficiency direct methanol fuel cell based on poly (styrenesulfonic) acid (PSSA)–poly (vinylidene fluoride)(PVDF) composite membranes.* Journal of fluorine chemistry, 2004. **125**(8): p. 1217-1230.
79. Lin, D.J., et al., *Preparation and characterization of microporous PVDF/PMMA composite membranes by phase inversion in water/DMSO solutions.* European polymer journal, 2006. **42**(10): p. 2407-2418.
80. Dang, Z.M., Y. Shen, and C.W. Nan, *Dielectric behavior of three-phase percolative Ni–BaTiO 3/polyvinylidene fluoride composites.* Applied Physics Letters, 2002. **81**(25): p. 4814-4816.
81. Wang, L. and Z.M. Dang, *Carbon nanotube composites with high dielectric constant at low percolation threshold.* Applied Physics Letters, 2005. **87**(4): p. 042903-042903-3.
82. Muralidhar, C. and P. Pillai, *Dielectric behaviour of barium titanate (BaTiO 3)/polyvinylidene fluoride (PVDF) composite.* Journal of materials science letters, 1987. **6**(3): p. 346-348.

83. Kim, W.S., et al., *Electrical properties of PVDF/PVP composite filled with carbon nanotubes prepared by floating catalyst method.* Macromolecular Research, 2002. **10**(5): p. 253-258.
84. Wang, D., K. Li, and W. Teo, *Preparation and characterization of polyvinylidene fluoride (PVDF) hollow fiber membranes.* Journal of Membrane Science, 1999. **163**(2): p. 211-220.
85. Salimi, A. and A. Yousefi, *Analysis Method: FTIR studies of β-phase crystal formation in stretched PVDF films.* Polymer Testing, 2003. **22**(6): p. 699-704.
86. Boudin, F., et al., *Microporous PVdF gel for lithium-ion batteries.* Journal of Power Sources, 1999. **81**: p. 804-807.
87. Bacon, D.R., *Characteristics of a PVDF membrane hydrophone for use in the range 1-100 MHz.* Sonics and Ultrasonics, IEEE Transactions on, 1982. **29**(1): p. 18-25.
88. Lehtinen, T., et al., *Electrochemical characterization of PVDF-based proton conducting membranes for fuel cells.* Electrochimica Acta, 1998. **43**(12): p. 1881-1890.
89. Nunes, S.P. and K.V. Peinemann, *Ultrafiltration membranes from PVDF/PMMA blends.* Journal of Membrane Science, 1992. **73**(1): p. 25-35.
90. Klinge, U., et al., *PVDF as a new polymer for the construction of surgical meshes.* Biomaterials, 2002. **23**(16): p. 3487-3493.
91. Sharma, T., et al., *Patterning piezoelectric thin film PVDF–TrFE based pressure sensor for catheter application.* Sensors and Actuators A: Physical, 2012. **177**(0): p. 87-92.
92. *Fully inorganic oxide-in-oxide ultraviolet nanocrystal light emitting devices.* Nature Communications, 2012. **3**: p. 690.
93. Li, J., et al., *Vibrational mode analysis of β-phase poly (vinylidene fluoride).* Applied Physics Letters, 2002. **81**(12): p. 2223-2225.
94. Park, Y.J., Y.S. Kang, and C. Park, *Micropatterning of semicrystalline poly (vinylidene fluoride)(PVDF) solutions.* European polymer journal, 2005. **41**(5): p. 1002-1012.
95. Martinelli, T., et al., *Intra-Aortic Balloon Occlusion to Salvage Patients With Life-Threatening Hemorrhagic Shocks From Pelvic Fractures.* The Journal of Trauma and Acute Care Surgery, 2010. **68**(4): p. 942-948 10.1097/TA.0b013e3181c40579.
96. Su, H., A. Strachan, and W.A. Goddard III, *Density functional theory and molecular dynamics studies of the energetics and kineticsof electroactive polymers: PVDF and P (VDF-TrFE).* Physical Review B, 2004. **70**(6): p. 064101.
97. Chang, J., et al., *Polymeric gate dielectric interlayer of cross-linkable poly (styrene-< i> r</i>-methylmethacrylate) copolymer for ferroelectric PVDF-TrFE field effect transistor memory.* Organic Electronics, 2009. **10**(5): p. 849-856.

98. Kim, J.H., B.E. Park, and H. Ishiwara, *Fabrication and Electrical Characteristics of Metal-Ferroelectric-Semiconductor Field Effect Transistor Based on Poly (vinylidene fluoride).* Japanese Journal of Applied Physics, 2008. **47**: p. 8472.
99. Bloomfield, P.E., F. Castro, and R. Goeller. *The design, processing, evaluation and characterization of pyroelectric PVDF copolymer/silicon MOSFET detector arrays*. in *Applications of Ferroelectrics, 1994. ISAF'94., Proceedings of the Ninth IEEE International Symposium on*. 1991: IEEE.
100. Peterson, J.I., R.V. Fitzgerald, and D.K. Buckhold, *Fiber-optic probe for in vivo measurement of oxygen partial pressure.* Analytical Chemistry, 1984. **56**(1): p. 62-67.
101. Kolkman, R.G.M., et al., *In vivo photoacoustic imaging of blood vessels using an extreme-narrow aperture sensor.* Selected Topics in Quantum Electronics, IEEE Journal of, 2003. **9**(2): p. 343-346.
102. Fujitsuka, N., et al., *Monolithic pyroelectric infrared image sensor using PVDF thin film.* Sensors and Actuators A: Physical, 1998. **66**(1): p. 237-243.
103. Hammes, P. and P. Regtien, *An integrated infrared sensor using the pyroelectric polymer PVDF.* Sensors and Actuators A: Physical, 1992. **32**(1): p. 396-402.
104. Fujitsuka, N., et al. *Monolithic pyroelectric infrared image sensor using PVDF thin film*. in *Solid State Sensors and Actuators, 1997. TRANSDUCERS'97 Chicago., 1997 International Conference on*. 1997: IEEE.
105. Vardi, G.M., V. Spivak, and E. Spivak, *Optical-acoustic imaging device*. 2003, Google Patents.
106. Chandrana, C., et al., *Demonstration of second-harmonic IVUS feasibility with focused broadband miniature transducers.* Ultrasonics, Ferroelectrics and Frequency Control, IEEE Transactions on, 2010. **57**(5): p. 1077-1085.
107. Lupotti, F.A., et al., *IVUS flow measurements: line spread function and decorrelation pattern.* Ultrasonics, 2002. **40**(1): p. 843-847.
108. *Photolithographic patterning of subwavelength top emitting colloidal quantum dot based inorganic light emitting diodes on silicon.* Applied Physics Letters, 2010. **96**(13): p. 131109.
109. Peng, L.M., et al., *Performing probe experiments in the SEM.* Micron, 2004. **35**(6): p. 495-502.
110. http://en.wikipedia.org/wiki/Transmission_electron_microscopy.
111. http://en.wikipedia.org/wiki/Confocal_laser_scanning_microscopy.
112. http://en.wikipedia.org/wiki/Differential_scanning_calorimetry.
113. Kearney, T.J. and M.M. Shabot, *Pulmonary Artery Rupture Associated With the Swan-Ganz Catheter.* CHEST Journal, 1995. **108**(5): p. 1349-1352.
114. Pu, J.A., et al., *PIEZOELECTRIC ACTUATION OF A DIRECT WRITE ELECTROSPUN PVDF FIBER*, in *Mems 2010: 23rd Ieee International Conference on Micro Electro Mechanical Systems, Technical Digest*, Ieee: New York. p. 1163-1166.

115. Wegener, M., *Polarization-electric field hysteresis of ferroelectric PVDF films: Comparison of different measurement regimes.* Review of Scientific Instruments, 2008. **79**(10): p. 106103-106103-3.
116. Brox, D., A.R. Mohammadi, and K. Takahata, *Non-lithographically microfabricated capacitive pressure sensor for biomedical applications.* Electronics Letters, 2011. **47**(18): p. 1015-1017.
117. Peng, C., et al. *A wireless and batteryless 130mg 300µW 10b implantable blood-pressure-sensing microsystem for real-time genetically engineered mice monitoring*. in *Solid-State Circuits Conference - Digest of Technical Papers, 2009. ISSCC 2009. IEEE International*. 2009.
118. Tan, R., et al., *Development of a fully implantable wireless pressure monitoring system.* Biomedical Microdevices, 2009. **11**(1): p. 259-264.
119. Doshi, J. and D.H. Reneker, *Electrospinning process and applications of electrospun fibers.* Journal of electrostatics, 1995. **35**(2): p. 151-160.
120. Reneker, D.H. and I. Chun, *Nanometre diameter fibres of polymer, produced by electrospinning.* Nanotechnology, 1999. **7**(3): p. 216.
121. Li, D. and Y. Xia, *Electrospinning of nanofibers: reinventing the wheel?* Advanced Materials, 2004. **16**(14): p. 1151-1170.
122. Huang, Z.M., et al., *A review on polymer nanofibers by electrospinning and their applications in nanocomposites.* Composites science and technology, 2003. **63**(15): p. 2223-2253.
123. Yee, W.A., et al., *Morphology, polymorphism behavior and molecular orientation of electrospun poly(vinylidene fluoride) fibers.* Polymer, 2007. **48**(2): p. 512-521.
124. Hansen, B.J., et al., *Hybrid nanogenerator for concurrently harvesting biomechanical and biochemical energy.* ACS Nano, 2010. **4**(7): p. 3647-3652.
125. Tan, S., et al., *Systematic parameter study for ultra-fine fiber fabrication via electrospinning process.* Polymer, 2005. **46**(16): p. 6128-6134.
126. Li, D., Y. Wang, and Y. Xia, *Electrospinning nanofibers as uniaxially aligned arrays and layer-by-layer stacked films.* Advanced Materials, 2004. **16**(4): p. 361-366.
127. Rafique, J., et al., *Electrospinning highly aligned long polymer nanofibers on large scale by using a tip collector.* Applied Physics Letters, 2007. **91**(6): p. 063126-063126-3.
128. Teo, W. and S. Ramakrishna, *A review on electrospinning design and nanofibre assemblies.* Nanotechnology, 2006. **17**(14): p. R89.
129. Ayres, C.E., et al., *Measuring fiber alignment in electrospun scaffolds: a user's guide to the 2D fast Fourier transform approach.* Journal of Biomaterials Science, Polymer Edition, 2008. **19**(5): p. 603-621.
130. Kim, G.M., et al., *One-dimensional arrangement of gold nanoparticles by electrospinning.* Chemistry of Materials, 2005. **17**(20): p. 4949-4957.
131. Shirinov, A.V. and W.K. Schomburg, *Pressure sensor from a PVDF film.* Sensors and Actuators A: Physical, 2008. **142**(1): p. 48-55.

132. Rodger, D.C., et al., *Scalable high lead-count parylene package for retinal prostheses.* Sensors and Actuators B: Chemical, 2006. **117**(1): p. 107-114.

Vita

Tushar Sharma was born in Mandi, Himachal Pradesh, India, on September 09, 1986, the son of Mr. Harish Chander and Mrs. Bhavenandu Sharma. He completed high school in Vadodara, Gujarat and Kota, Rajasthan. In August 2004, he was admitted to the Indian Institute of Technology Madras, India, were he received his undergraduate bachelor's degree in Biotechnology. He was also the recipient of the prestigious Bhagyalakshmi and Krishna Ayengar award for the best research work. Tushar enrolled in the Biomedical Engineering graduate program at the University of Texas at Austin in August 2008 and completed with a Master of Science in Engineering degree in August 2010. His master's thesis research, supervised by Dr. John X.J. Zhang, focused on implantable systems capable of generating electricity from blood glucose. The resulting new design of implantable biofuel cells utilized nano-thin layer of mesoporous (nanoporous) silica as the membrane to boost the biofuel cell power output. Since then, he has specialized in application of piezoelectric nanostructures and electrospun nanofibers for implantable biosensors, energy harvesting, and life science under the guidance of Dr. John X.J. Zhang.

Permanent email: tusharsharma@utexas.edu

This dissertation was typed by the author.